Characterization of Magnesium and Magnesium Alloys Processed by Equal Channel Angular Extrusion

by
Nicholas M. Krywopusk

A dissertation submitted to Johns Hopkins University in conformity with the requirements for the degree of Doctor of Philosophy

Baltimore, Maryland
April 2018

Abstract

Magnesium has shown substantial promise as a structural material due to its low density and high specific strength. The lack of primary slip systems and severe tension-compression anisotropy has historically limited traditional forming methods at room-temperature. Thermo-mechanical processing by methods of Severe Plastic Deformation (SPD), such as Equal Channel Angular Extrusion (ECAE), has proven exceptionally effective in microstructural refinement. These successes have included enhanced strength, ductility, and texture modification. Although widely studied, a significant number of gaps in knowledge remain in the processing of magnesium by ECAE, including experimental confirmation of ECAE processing homogeneity, the effect of strain-rate on microstructural evolution, and the relative activation of competing mechanisms for microstructural refinement.

Samples of 99.9% pure Mg and AZ31B were processed by ECAE at elevated temperatures for the purposes of microstructural characterization, and to determine the homogeneity of the microstructural refinement within the ECAE processed samples. Characterization was carried out using Electron Backscatter Diffraction (EBSD). The microstructures and textures of both materials were found to be generally uniform throughout the billet. AZ31B was found to have a smaller average grain size and a narrower grain size distribution. Grain boundary misorientation distributions reveal a peak around 30° that is associated with the recrystallization process. In addition, peaks associated with extension twinning were occasionally seen. Both materials exhibit a basal fiber texture expected of the $4B_C$ processing route in ECAE, although AZ31B displayed fewer local variations and a tendency for basal pole splitting.

There is some question regarding the extent to which AZ31B exhibits strain-rate hardening, and the conditions under which it occurs. To resolve this question, samples of rolled and ECAE processed AZ31B were mechanically tested under uniaxial compression at multiple quasi-static rates and orientations. The project is intended to dove-tail with the Kolsky bar work being performed by Kannan et al., in order to explore AZ31B strain-rate hardening behavior over a wide range of strain-rates. Both rolled and ECAE processed AZ31B were found to exhibit strain-rate hardening effects. Sigmoidal stress-strain curves were observed in the rolled AZ31B compressed along the $\langle a \rangle$ axis and both ECAE orientations. In the rolled material, the sigmoidal curves were found to be due to extension twinning. However, no twinning was observed in the ECAE material. The shape of the curve is instead attributed to the concurrent action of stress-induced grain growth and Taylor hardening.

Spall is known to be a factor in the high strain-rate failure of magnesium. While a number of studies have investigated spall behavior of magnesium and its alloys, few have explored the micro-mechanics of spall through fractography. Samples of AZ31B processed by the $4B_C$ ECAE route were subjected to spall recovery tests in two different orientations. The resulting spall behavior is studied via fractography. Two potential sites were found for the nucleation of spall: voids at fractured, coarse precipitates and pre-existing voids in the matrix. These two sources appear to produce different spall behaviors. Voids at fractured precipitates cause particle fracture that, in turn, further drives crack growth along the length of the precipitate. In contrast, voids in the matrix undergo ductile growth by nanovoid formation. Although the study is incomplete, these initial results suggest that nanovoids in the extrusion direction oriented samples grow

without the assistance of nanoscale precipitates; while in the transverse direction orientation samples nanovoid growth can be linked to nanoscale precipitates.

In ECAE processing, the effects of route design and temperature on the final microstructure have been studied extensively. Typically, these experiments were conducted at an optimized and fixed extrusion rate. As such, the systematic effects of strain-rate have received much less attention. Here, billets of pure Mg were ECAE processed at rates of 0.127, 0.381, and 0.762 mm/s for one, two, three, and four passes of the $4B_C$ route. The processed billets were subsequently characterized by EBSD. The area fraction of recrystallized grains was found to increase with higher extrusion rates. Nucleation of recrystallized grains was observed to be largely heterogeneous and orientation dependent. The average recrystallized grain size showed no significant change with pass, but the 0.762 mm/s rate did display a modest reduction. Both the 0.762 and 0.127 mm/s rates were found to possess a greater volume fraction of extension twins than the 0.381 mm/s rate. The larger fraction of twins was hypothesized to be attributed to the necessity for greater strain accommodation at the higher rates, and to the microstructure retaining some orientations favorable for twinning at lower rates.

Discerning which processing mechanisms are operative during ECAE processing under different temperature regimes and orientations has proven difficult *ex situ*. Furthermore, the mechanisms themselves are only partially understood. A neutron transparent ECAE die, including heating and backpressure capability, has been designed and fabricated. Pure magnesium was extruded in two orientations and at three temperatures while using *in situ* neutron diffraction at the VULCAN diffractometer at the Spallation Neutron Source (SNS). Under all experimental conditions, a large amount of

extension twinning was found to occur that produced a basal texture in the longitudinal direction. The extensive twinning was found to mitigate the effects of initial orientation on dynamic crystallization. Samples processed at lower temperatures were found to exhibit more discontinuous dynamic recrystallization-like behavior than those at higher temperatures.

Readers:
Prof. Timothy P. Weihs, Advisor
Dr. Laszlo J. Kecskes

Acknowledgements

There are many people throughout my undergraduate and graduate research that I am fortunate to have met. My advisor, Professor Tim Weihs, must be thanked first. Professor Weihs taught me how to frame a problem, not only to better dissect it, but also to give the research its greatest impact. His guidance and emphasis on communication has helped me to grow as a researcher, and greatly improve as a writer and speaker. Professor Weihs' direct and respectful manner of leadership, both within the lab and without, is a model to be followed.

Thanks also goes to Dr. Laszlo Kecskes, who acted as a second advisor to me as a part of the collaboration with the Army Research Laboratory within MEDE. Laszlo's extensive knowledge of magnesium and the ECAE process was invaluable throughout the project, but proven especially useful in formulating our early experiments. I suspect that we would have encountered many more pitfalls and dead ends without his experience. We had many useful discussions, and Laszlo was always ready with advice on everything from the writing process to tailoring my career.

I would like to thank the other members of my committee: Professor Todd Hufnagel, Professor Kevin Hemker, and Professor KT Ramesh. I am appreciative both for their insightful comments and their own contributions to this work through various discussions and collaborations.

I am grateful for the help and support provided over the years by my labmates: Dr. Karsten Woll, Dr. Thomas Voisin, Dr. Shashank Vummidi Lakshman, Dr. Xiaolong Ma, Dr. Adam Stover, Dr. Michael Grapes, Dr. Kyle Overdeep, Dr. Longyu Zhao, Dr. Alex Kinsey, Kyle Slusarski, Elliot Wainwright, Suhas Eswrapa Prameela, Shane

Arlington, John Fite, Jesse Grant, and David Gibbins. I would also like to thank students from various other groups for their help, advice, and shared data: Dr. Ravi Shivaraman, Dr. Ian McCue, Vignesh Kannan, Meng Zhao, Debjoy Mallick, and Caleb Hustedt. In particular, I could not have performed the neutron diffraction experiment at ORNL without the aid of Dr. Laszlo Kecskes, Dr. Shashank Vummidi Lakshman, Dr. Alex Kinsey, and Caleb Hustedt.

Over the course of my time in the program, I was assisted by three undergraduate students. Paul Masih Das spent a great deal of time helping me to prepare, sputter, and evaluate wafers of chemical time delays, which unfortunately did not make it into this thesis. Mike Tershakovec performed nanoindentations on ECAE processed magnesium. Zihao He greatly assisted me in making and mechanically testing a large number of AZ31B samples.

I would like to thank Micah Gallagher and David Runk who graciously spent a great deal of time extruding magnesium billets for me and the rest of the MEDE program.

I am indebted to Mike Franckowiak, Walt Krug, Frank Cook, Niel Leon, and Rich Middlestat of the Hopkins machine shop. They were invaluable in refining concepts and turning ideas into reality. The neutron transparent ECAE die wouldt be considerably less streamlined without their advice and input.

I would like to thank the staff of the Department of Materials Science and Engineering and Hopkins Extreme Materials Institute for all of their help over the years. Ada Simari, Jeanine Majewski, Bess Bieluczyk, Katie Vaught, Marge Weaver, Dorothy Reagle, and Paula Davis all deserve a great deal of thanks. In addition, Bryan Crawford

and Mark Koontz were great resources whether using a new machine or planning a new experiment.

Our collaborators at Oak Ridge National Lab: Ke An, Matthew Frost, Yan Chen, and Wenduo Zhou deserve thanks for providing advice during the planning of the neutron diffraction experiment, assistance during its execution, and help during the analysis of the data.

I would like to thank the Army Research Laboratory for the financial support.

I would be severely remiss if I did not thank my parents, Sandra and Roman Krywopusk for helping me get to this point, and for their support and encouragement throughout my graduate life.

Finally, I would like to thank Katie. She has gracefully endured long night and strange working hours, brought me dinner and more importantly coffee when I am unable to leave the lab, and suffered through editing my first drafts. Her support helped me to be more productive, work through the lows of graduate school, and brought me much joy overall.

Table of Contents

List of Figures

List of Tables

1. Background and Research Summary

1.1 Background

1.1.1 Motivation

The desire for weight reduction in structural materials has driven investigation of a number of lightweight materials and, in particular, has garnered significant attention for magnesium and its alloys [1]. This is due to magnesium being the lightest of the structural metals; yet it possesses high specific strength [1]. Among the groups interested in the development of magnesium for weight reduction purposes, the US Army wants to incorporate magnesium into armor systems. The Army has conducted V_{50} tests on AZ31B to assess ballistic performance and identified the relevant failure mechanisms at high rates [2]. During V_{50} tests, armor-piercing or fragment-simulating projectiles strike the target at parametrically varied velocities [2]. The velocities of the fastest projectile that does not cause material failure and the slowest projectile that does cause failure are averaged into the V_{50} metric (see figure 1.1). These tests have formed the basis of our understanding of the behavior of magnesium under ballistic conditions, and, as a result, have demonstrated that dynamic strength and spall strength are two of the more important parameters for dynamic behavior.

However, a necessary precursor to optimization of dynamic strength and spall strength is the capability for materials by design, and hence, a thorough understanding of which microstructural features improve those parameters and knowledge of how to achieve the desired microstructures. Both of these issues are currently being addressed by the Materials in Extreme Dynamic Environments (MEDE) program, and my particular focus is on the latter issue. A detailed study in this area requires both overcoming

traditional challenges in magnesium processing, as well as investigating the relationship between processing conditions and microstructural evolution.

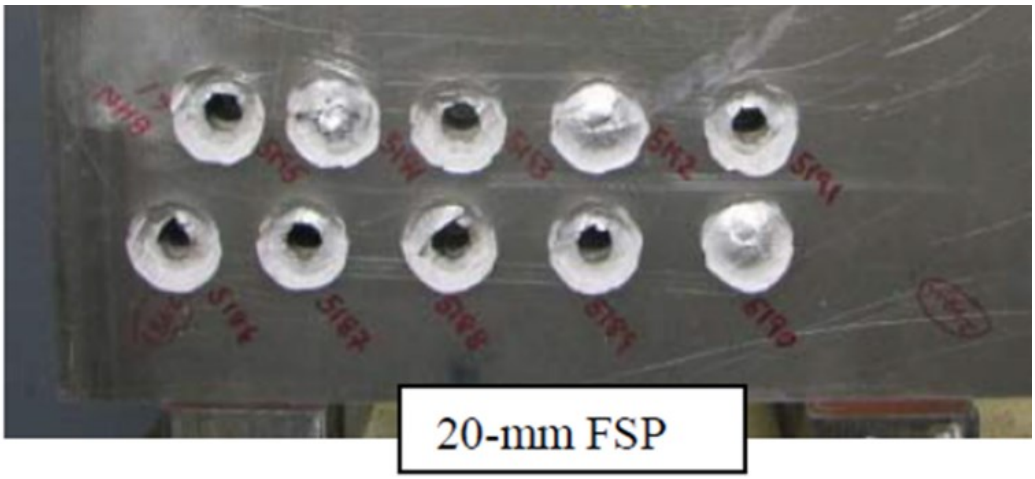

Figure 1.1: Rear view of AZ31B-H24 plate after V50 testing showing spall failure.

1.1.2 Challenges in Magnesium Processing

The source of the challenges in the mechanical deformation of magnesium, including the mechanical processing of magnesium, can be seen by looking at the application of the Taylor model to Hexagonal Close Packed (HCP) metals [3–5]. According to the Taylor model, 5 independent shears, generally in the form of slip systems, must be operational for uniform, crack-free deformation. However, the $(0001)\langle 11\bar{2}0\rangle$ primary slip system in magnesium only has 2 independent modes, and secondary slip systems must be activated [3,5–7]. The prismatic $\{1\bar{1}00\}\langle 11\bar{2}0\rangle$ system provides 2 more modes with the Burgers vectors still confined to the basal plane [3]. It is not until the activation of the pyramidal $\langle c+a\rangle$ system that there is a 5th independent slip system and strain along the $\langle c\rangle$ axis can be accommodated [3]. Of these systems, $\langle c+a\rangle$

is the most difficult to activate, although there is evidence of a strong temperature dependence for this system [3,5,6,8]. Due to the difficulty of activating $\langle c + a \rangle$ slip, alternative deformation modes, such as deformation twinning is frequently activated [9]. Schematics of the slip and twin systems in magnesium can be seen in figure 1.2.

A simple definition of twinning is offered by Christian and Mahajan, where twinning is defined as the reorientation of the parent lattice structure by simple shear of the lattice [10]. In practical terms, the twin boundary is a mirror plane between the parent and twinned lattice. It should be noted that unlike dislocations, twin systems in a material may only operate in a single direction [5]. Hence, there are extension twin systems, which serve to elongate the $\langle c \rangle$ axis, and contraction twin systems, which compress the $\langle c \rangle$ axis. A number of potential twin systems exist in HCP materials, but not all of them are active in every material system. In fact, Yoo has noted that highly ductile HCP metals (e.g. Ti) tend to twin easily in both extension and contraction modes, while those metals that are known to be brittle may only have a single mode active [3]. In magnesium, $\{10\bar{1}2\}$ extension twins and $\{10\bar{1}1\}$ contraction twins are the modes most frequently observed [3,5,11]. Of the two, the $\{10\bar{1}2\}$ extension twins appear to be more easily activated, with loading in $\langle c \rangle$ axis tension being known to exhibit enhanced ductility compared to $\langle c \rangle$ axis compression [5,9]. In contrast, the $\{10\bar{1}1\}$ contraction twin frequently double twins into softer orientations that can lead to strain localization and failure [11]. Additionally, Barnett has reported lenticular voids that possess the same habit as the compression twins, suggesting an interaction between void growth and these types of contraction twins [11]. Altogether, the combination of limited slip systems and

extension and contraction twins that display radically different mechanical behaviors result in strong tension-compression asymmetry and poor formability in magnesium.

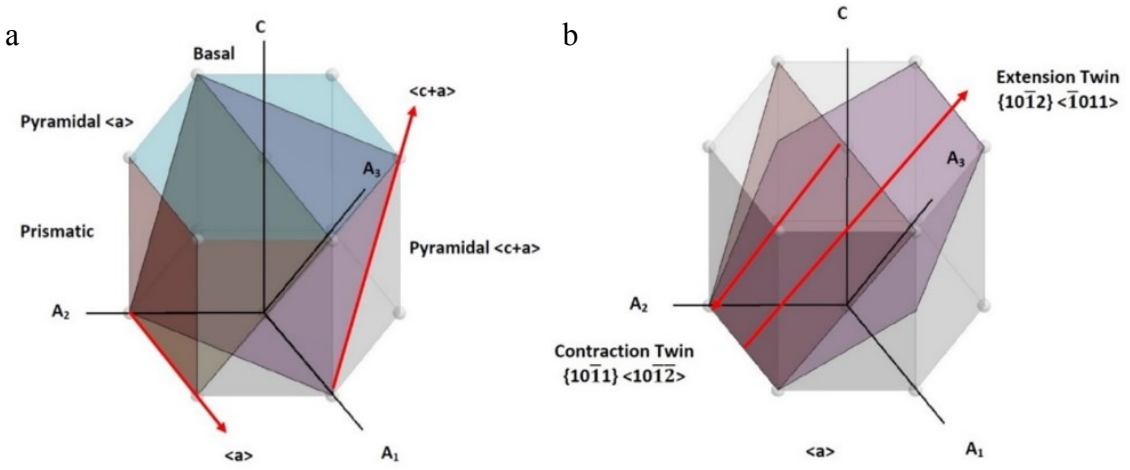

Figure 1.2: (a) Schematic of the slip systems in HCP. (b) Schematic of twin systems known to be active in magnesium.

1.1.3 Severe Plastic Deformation

Severe Plastic Deformation (SPD) is a collection of methods that are known to overcome the formability challenges in magnesium and improve its mechanical properties [12–24]. The definition of SPD provided by Estrin and Vinogradov is "any method of metal forming under an extensive hydrostatic pressure that may be used to impose a very high strain on a bulk solid without the introduction of any significant change in the overall dimensions of the sample and having the ability to produce exceptional grain refinement" [25]. As the definition states, the primary method by which SPD enhances mechanical properties in magnesium and other materials is through grain refinement and taking advantage of the Hall-Petch effect, which can be represented as an equation of the form:

$$\sigma = \sigma_0 + Kd^{-\frac{1}{2}} \quad (1)$$

where σ is the yield stress, $\sigma_0$is the bulk yield stress, K is a constant, and d is the grain size [12,13]. A host of SPD methods exist, but among the most common are High Pressure Torsion (HPT), Accumulative Roll Bonding (ARB), Multiaxial Forging (MAF), Cyclic Extrusion Compression (CEC), Repetitive Corrugation and Straightening (RCS), and Equal Channel Angular Extrusion (ECAE), sometimes called Equal Channel Angular Pressing (ECAP) [12–25]. Two studies are highlighted that display the capabilities of SPD in general and ECAE in particular. First, Figueiredo and Langdon have reported superplasticity in ECAE processed magnesium that has achieved approximately 3050% elongation, setting a record for elongation achieved in magnesium [26]. Second, Ding et al. have achieved grain sizes of approximately 0.35 μm in AZ31B, which had been processed by a complex hybrid ECAE route including a step-down temperature method [27]. At the time, this study set a record for strength in magnesium [27]. The "step-down" method developed by Ding et al. relies on two basic principles: reducing the temperature of ECAE processing reduces the grain size of the resultant microstructure and fine microstructures can sustain more severe processing conditions without localizing than coarse microstructures. The early extrusions use comparatively gentle extrusion temperatures to begin microstructural refinement. As the microstructure is refined with further extrusions, the extrusion temperature is progressively lower to achieve ultrafine microstructures.

In its simplest form ECAE is the pressing of a billet through two intersecting channels, most typically at 90° to one another as seen in figure 1.3. Under ideal conditions, when the billet passes through the plane where the channels meet, a simple

shear is imparted [24,25]. The strain imparted during processing is a solely a byproduct of the die geometry when friction is low and the outer die angle is sharp, and is given by the equation [24]:

$$\gamma = 2\cot\theta \tag{2}$$

where γ is the shear strain imparted, and θ is half of the interchannel angle. For the case of a 90° interchannel angle, the strain imparted is approximately 1.15 [25]. The ECAE process was invented by VM Segal who also derived the above equation, and he has contributed significantly to its further development over the decades [28–30]. To summarize his contributions, Segal found that the shear zone is thinnest, and the plastic deformation most uniform, when the friction between the billet and the sidewalls is minimized, the outer corner of the die is sharp, and the die intersection angle is close to 90° [25,28–30]. Outside of these findings, the single most significant advancement in ECAE processing has been the introduction of backpressure. The addition of backpressure has been found to increase the hydrostatic stress state and narrow the shear region. In turn, this leads to a reduction in shear localization, enhanced strength and ductility, and in at least some alloys, reduced subgrain size and concomitant smaller average grain size after processing [31–33]. In some cases, nonuniformity of friction forces causes "stick-slip" behavior, where the extrudate displays periodic shear localization [34]. The addition of backpressure has been found to significantly reduce the occurrence of this issue [34]. For magnesium, elevated temperatures and backpressure are necessary to improve ductility through activation of non-basal slip systems and through increases in hydrostatic stress [13,35,36]. The application of backpressure and the minimization of sidewall friction have driven increasingly complex die designs. Most

modern dies not only possess backpressure and heating capabilities, but some combination of sliding inlet and outlet walls to minimize friction.

Since the shape of the billet is not altered by processing, and the microstructure is generally not fully refined after a single pass, billets tend to be processed a number of times under different routes. Routes are defined as rotations around the long axis of the billet after each pass. The four basic routes discussed by Segal are A, B, C, and D. The A route has no rotations of the billet. The B route alternates between +90° and a - 90° rotations. The C route rotates the billet 180°, and the D route rotates the billet 90° in the same direction after each pass [30]. The terminology has changed slightly, with routes B and D now more commonly called B_A and B_C, respectively. These routes have been found to impart certain common textures on hcp materials. Yapici and Karaman found that a single pass of ECAE tended to produce a basal texture in Ti-6Al-4V, Zr, Be, and AZ31 that is approximately 27° inclined from the longitudinal axis [37]. They attribute this to the activation of basal slip, even in Ti-6Al-4V and Zr where prismatic slip is the preferred slip system [37]. Suwas et al. have investigated the effect of the 4A, $4B_C$, and C routes on the texture evolution of pure Mg [36]. They found that the first pass had a texture similar to that mentioned by Yapici and Karaman. Repeated shearing on the same plane during the A route decreased the inclination of the basal poles relative to the longitudinal direction. The C route maintained essentially the same texture the entire time, but did display some remnant texture from the previous pass. The B_C route deviated the most from the other two routes. In that case, the basal poles were pulled off of the vertical axis and towards the transverse direction. While the four basic routes are used most frequently, a number of hybrid routes have been designed to improve mechanical

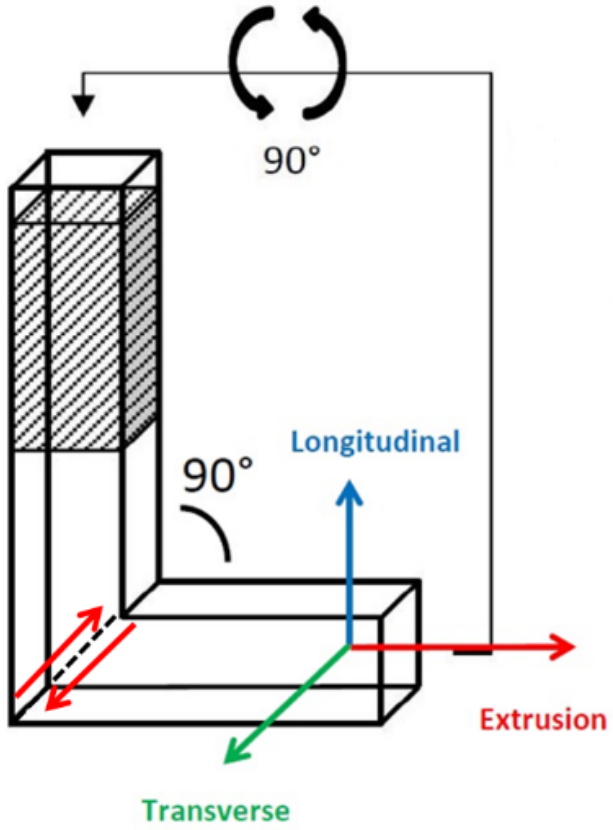

Figure 1.3: Schematic of typical ECAE processing with the shear zone indicated by the dashed line and the shear direction in red arrows. Generally, the direction orthogonal to the longitudinal and extrusion directions is called the transverse direction. In some literature, however, it is also called the flow direction.

properties by combining the basic routes, such as the 10ACB route designed by Ding et al. and the 5H route designed by Foley et al. [27,38].

1.1.4 Shock and Spall Fracture

As mentioned above, spall failure is one of the active mechanisms for failure of Mg alloys at high rates, and learning how to improve spall strength is one of the goals of the MEDE program. This section briefly discusses the topic. Failure by spall – either by void growth or cracking – occurs where tensile release waves of sufficient amplitude meet

[39]. This occurs when a plate, or in some cases explosive or laser shock loading, impacts a sample. A compressive wave propagates through the material. Upon reaching the opposite surface, a tensile release wave is reflected back from the surface. If the spall strength is exceeded, spallation occurs in the region now under tension. This behavior is depicted in figure 4 [39]. Strain-rates from roughly 10^2-10^7 s^{-1} can be achieved across all shock-loading methods: plate-impact, explosive, and laser irradiation [40]. Meyers identifies four sites for heterogeneous nucleation of spall: fracture of particles, fracture of the matrix at particle interfaces, particle delamination, and fracture at grain boundaries [39]. In addition, spall may be nucleated homogeneously at dislocation networks, low angle boundaries, or very fine particles [39]. It is important to note that the usage of the term "homogeneous" here refers less to a true homogeneous nucleation than to nucleation that is typically below the resolution of most microscopy methods. Regardless of whether the deformation is ductile or brittle (and thus the characteristic flaws are voids or cracks, respectively), the nucleated flaws tend to grow and coalesce into a fracture surface [40]. At higher strain-rates, there is less time available for growth and coalescence. This leads to greater nucleation of flaws and the corresponding reduction in spacing, and requires greater stresses to form [40]. As a result, spall strength tends to increase with strain-rate [41].

Spallation of cubic materials has been studied intensely, but in comparison there is relatively little research on Hexagonal-Close-Packed (HCP) materials [41]. Wielewski et al. performed fractography on spalled Ti-6Al-4V specimens [42]. In this case, it was found that voids nucleated at grain boundaries between plastically hard and soft grains prior to undergoing ductile growth and coalescence [42]. The authors also observed that

the spalled microstructure contained no twins, in spite of the fact that Ti is known to twin easily under both tension and compression [42]. Simulations of nanovoid growth in Mg by Ponga et al. suggest an upper bound on spall strength of approximately 2.2 GPa due to a lack of secondary hardening near growing nanovoids [43].

Spall failure by cracking has also been investigated in Mg and its alloys. Rességuier et al. investigated spallation in single crystal magnesium loaded along the (0001) and $(10\bar{1}0)$ directions, revealing orientation dependent spall behavior. Samples loaded along the (0001) direction tended to display a very flat fracture surface, while samples loaded along the $(10\bar{1}0)$ direction possessed an extremely jagged surface. This behavior is attributed to voids growing along the direction of twins in the $(10\bar{1}0)$ samples. They also note the presence of voids amidst fields of short, thin tension twins. Finally, recrystallization is observed near the spall surface, although it is attributed to static recrystallization. Hazell et al. studied Elektron 675 where columns of fine grains were observed on one plane [44]. Shock loading along directions parallel and perpendicular to these columns showed preferential cracking along these columns [44]. The samples where the columns, and thus the cracks, were perpendicular to the spall plane exhibited improved spall strength over samples where the columns ran parallel to the spall plane [44]. This higher spall strength was comparable to the strength in AZ31B reported by McQueen et al. in 1970, and lower than the strength reported in Mg95 by Kanel et al. in 1996 [44]. This suggests that the columns parallel to the spall plane act as a softening mechanism. Most similar to the current work was a study performed by Farbaniec et al on AZ31B plate processed by the ECAE 4E route [45]. The 4E route is a hybrid of the B and C routes adapted to the plate geometry [45]. The 4E route in this

study also used a moderate step-down temperature component. Farbaniec et al. observed that particle fracture played a primary role in the spall failure of AZ31B 4E [45]. The details of the study will be discussed in greater detail in section 2.1.3

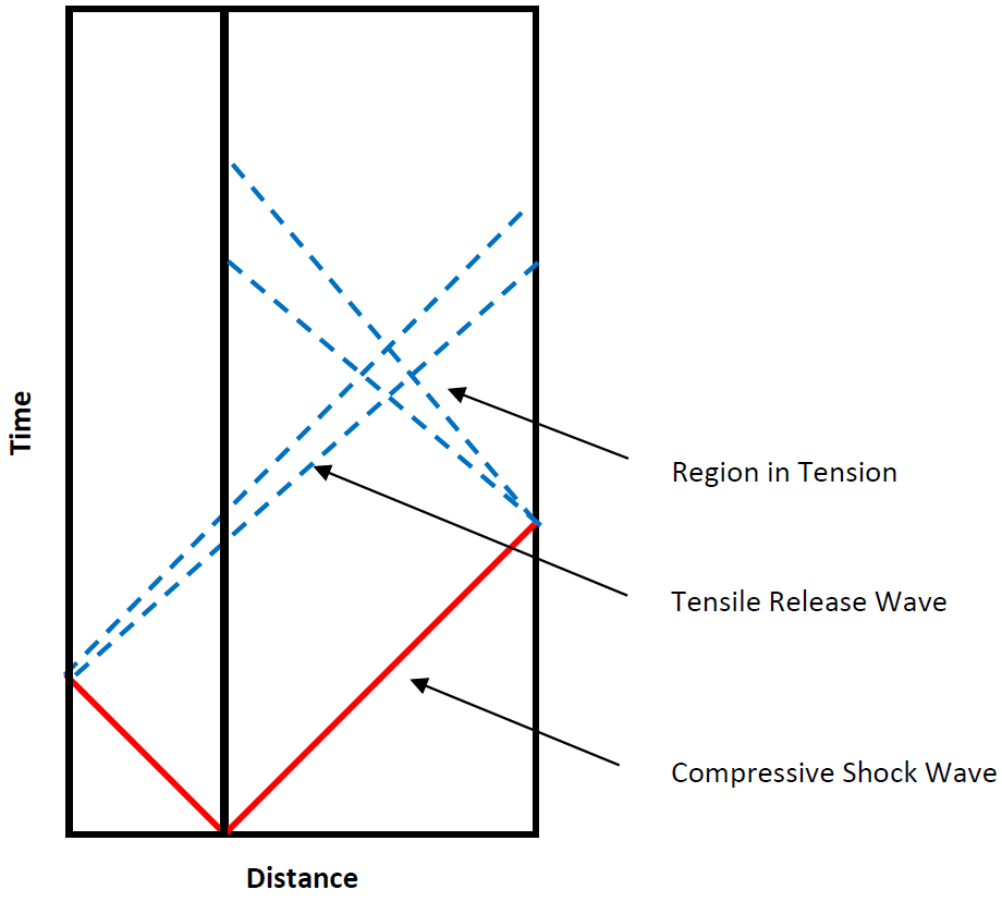

Figure 1.4: Time *versus* distance (Lagrangian) schematic of shock loading. The solid red lines indicate compressive waves, and the dashed blue line indicates tensile waves. The shaded region is under tensile stress.

1.1.5 Dynamic Recrystallization

The primary mode by which the microstructure is refined during ECAE and other SPD processes is dynamic recrystallization (DRX), which is an energy reduction process where new grains consume the parent microstructure *during* deformation [46]. This is in

contrast to static recrystallization, which typically occurs during annealing following processing, and so-called metadynamic recrystallization, which is the continuation of the recrystallization process after deformation is complete [46]. DRX encompasses a number of mechanisms, which can be split into two broad categories: discontinuous DRX (dDRX) and continuous DRX (cDRX) [46,47]. To some extent, dDRX and cDRX can be thought of as "nucleation and growth" and "homogeneous" type transformations, respectively [47]. During dDRX, grains nucleate heterogeneously and then undergo long range grain growth [46,47]. It should be noted that the nuclei in dDRX are not nuclei in the sense of a cluster of atoms of sufficient size for growth, but rather are subgrains that exist prior to recrystallization [47]. During cDRX, subgrain boundaries absorb dislocations and increase in misorientation, eventually forming high angle boundaries [46]. In both cases, subgrains are the source of the recrystallized grains, and the fundamental cause of the different behaviors is the competition between the grain boundary mobility and the rate of dynamic recovery [46,47]. In cases where recovery is difficult, due to low stacking fault energies (SFE), or where boundary mobilities are high, such as at high angle boundaries, dDRX is favored. When recovery is relatively easy, and grain boundary mobility is relatively low, cDRX is favored. A number of factors impact the competition between the mechanisms. Higher temperatures, typically greater than half of the homologous temperatures, favor dDRX [46]. In contrast, higher SFE, strain-rate, and grain size all favor cDRX [46]. Additionally, precipitates and solutes also influence which mechanism is active. dDRX may be stimulated in the deformation zone around large particles, and smaller particles may inhibit grain growth [46,47]. Solute segregation to the grain boundaries impedes grain boundary mobility and makes dDRX more difficult

[47]. Existing research has found that cDRX requires much higher strains for saturation than dDRX [46]. This means that it will take dDRX much fewer ECAE passes to saturate the microstructure than cDRX. Many researchers note that the microstructural refinement produced by both processes is sensitive to the processing parameters used [46,48].

To understand how dDRX and cDRX impact microstructural and texture evolution, it is worthwhile to examine the mechanisms of each process. The case of dDRX will be discussed first. During deformation, dislocation density gradients across grain boundaries drive local bulging of the boundaries and the formation of subgrains [37]. At lower strain rates and higher temperatures, grain boundary sliding generates additional strains and drives the recrystallization of the bulged subgrain [46,49]. In other cases, a twin may nucleate and span the bulge, essentially creating a recrystallized grain with a twin orientation [46]. dDRX does not occur only at grain boundaries, but anywhere that boundary mobility is easy such as at twin boundaries or near coarse particles. Because local strains contribute to dDRX, the recrystallized grains are thought to possess a random orientation. The propagation of dDRX thus tends to weaken the texture of the microstructure. The local nature of nucleation and long range grain growth during dDRX creates microstructures that contain significant variation in grain size and dislocation density. A newly recrystallized dDRX grain has a very low dislocation density [46]. As it grows, it accumulates dislocations until it reaches a critical strain energy, and a new grain is recrystallized [46]. Because dDRX nucleation is heterogeneous, a fully recrystallized microstructure contains grains in every stage of this lifecycle. Thus, a fully recrystallized microstructure contains a range of grain sizes and internal substructure.

Unlike the dDRX nucleation and growth process, cDRX is a homogeneous recovery process. The fact that cDRX is a recovery process has produced some contention in the literature. Some researchers divorce cDRX from DRX completely, and categorize it under the dynamic recovery umbrella [47,50]. However, as cDRX fits the definition of recrystallization already discussed, I consider cDRX to be a recrystallization process. As in the initial stages of cDRX, plastic deformation drives the generation of dislocations and the formation of cellular subgrains from those dislocation networks [46]. The activity of non-basal slip systems is required for the dislocation networks to rearrange into cell walls, and this is generally accomplished through cross-slip of the non-basal systems [49]. The rate of cross-slip is slow, and is generally the rate limiting step for the formation of cellular subgrains at moderate and high temperatures [40]. As deformation proceeds, glissile dislocations are absorbed by the subgrain boundaries, both increasing their misorientation and complexity [46,49]. The subgrain boundaries continue to absorb dislocations, and eventually form high angle boundaries (typically considered to be boundaries with misorientations greater than 15°) [46,49]. As might be expected, the newly recrystallized grains contain few, if any, dislocations, but Sakai et al. also indicate that the recrystallized grains are subject to large elastic distortions as a result of their nonequilibrium grain boundaries [46]. These elastic distortions produce local stresses that can impede dislocation motion, and may contribute to the enhanced mechanical properties of these microstructures despite low dislocation density [46]. Due to the lack of long range boundary migration, the grain sizes produced by cDRX are fairly uniform. In addition, the misorientations relative to the parent structure of grains recrystallized by cDRX are small compared to those in grains produced by dDRX. The

result is an overall “preservation” of the parent texture [46]. It is of interest to note that the dislocation density is highest near pre-existing high angle boundaries [49]. Thus, it is not uncommon to observe cDRX occurring preferentially near high angle boundaries before propagating towards the grain interior. From a microstructural analysis perspective, this means that microstructures undergoing cDRX and dDRX may appear similar at intermediate stages, where parent grains are surrounded by rings of recrystallized grains – a “necklace” structure [46].

DRX in magnesium is particularly complex, as there are many potential competing mechanisms. As a consequence, the literature is not always in agreement on which process, or even individual mechanism, is dominant during deformation under a given set of processing conditions [46,48–51]. Barnett et al. even reported apparent activation of both cDRX and dDRX in AZ31 [48]. This suggests either that activation of one mechanism does not preclude activation of other mechanisms, or that the mechanisms are highly sensitive to microstructural conditions. These factors provide significant challenges and opportunities in the investigation of DRX in magnesium. It is difficult to extricate individual mechanisms, particularly from fully recrystallized microstructures, and delineation of a mechanism plot requires extensive understanding of the various ways in which different microstructural and processing parameters interact. The payoff for this understanding is the capability for a high degree of control over the magnesium microstructure. For example, twinning or dDRX may be encouraged during early processing stages for enhanced ductility, and cDRX encouraged later to preserve that texture and improve the strength of the alloy. I have come to believe that understanding DRX in magnesium is a critical component that is required for

microstructure optimization. It is for this reason, that much of the following work is devoted to understanding the effects of ECAE processing parameters on the resultant magnesium microstructure.

1.2 Research Summary

The work in the following chapters are roughly divided between projects that support other MEDE tasks (Chapters 2, 3, and 4) and projects focused on investigating the effects of processing parameters on microstructure evolution (Chapters 5 and 6). While reading this entire work will provide a full story, it is accepted that readers will likely focus only on single chapters. Therefore, the chapters are largely written in such a way that they stand on their own. In approaching the processing and microstructural evolution of magnesium microstructures from so many different perspectives, it can prove difficult to synthesize the lessons learned. Therefore, I think that before delving too much further, it may be useful to filter this work into its contribution to our understanding of magnesium's processing-structure-properties triangle. Figure 1.5 is the general body of knowledge with regards to ECAE processing and MEDE's interests. The temperature-structure and route-structure interactions have been the most investigated in the literature, and backpressure has proven its value in grain refinement and texture management. Figure 1.5 displays a conspicuous lack of known interactions between extrusion rate and precipitates, and between imparted strain and texture. Even more evident, although the extrusion rate is known to interact with temperature and backpressure to impact the success of extrusions, the interactions links to structure are very few. The impact that this

work has had on generating or strengthening interactions will be assessed in the concluding chapter.

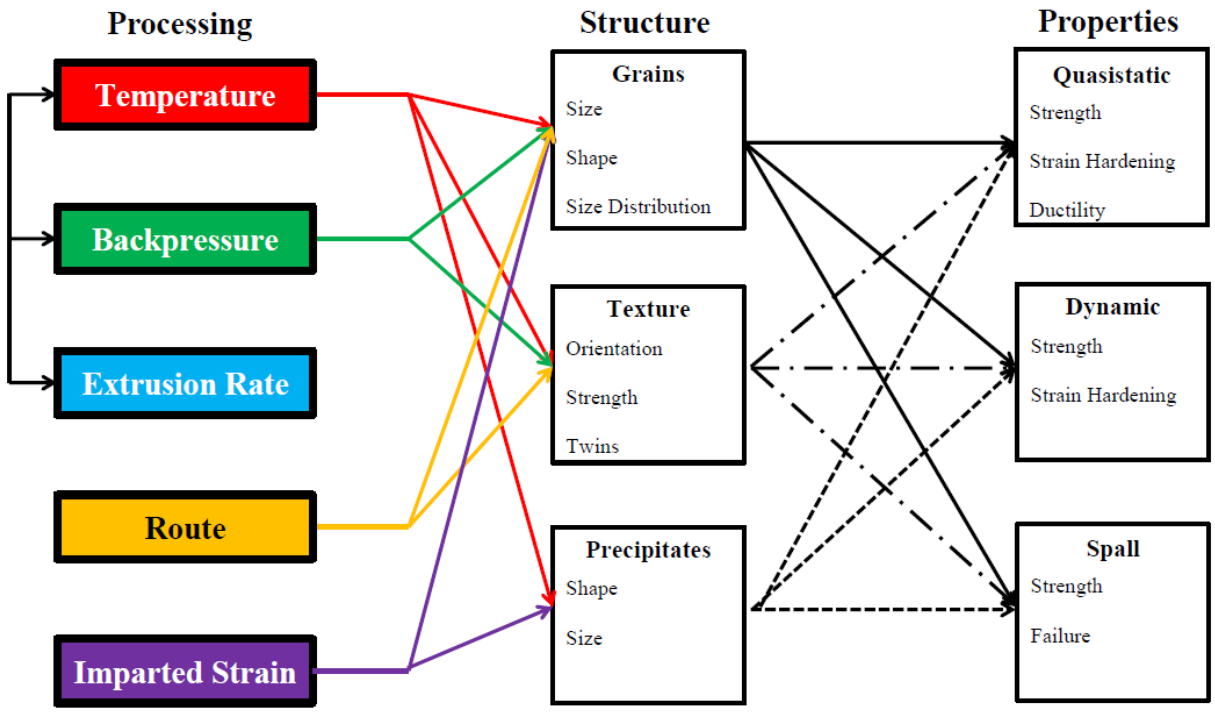

Figure 1.5: Schematic of the body of knowledge as it relates to ECAE processing, microstructural refinement, and mechanical properties. Relationships are indicated with lines.

2. Characterization of Pure Mg and AZ31B

2.1 Introduction

While there has been a renewed interest in magnesium as a structural material in the automotive and aerospace fields due to its low density and high potential strength, conventional thermomechanical processing of magnesium has led to limited ductility due to the lack of primary slip systems and a tension-compression asymmetry [3]. Multiple SPD methods, including ECAE, have been investigated to circumvent these issues and improve the microstructural and mechanical properties of the magnesium material.

In the past, ECAE has been found to be a robust thermo-mechanical processing technique; and, as such, has been applied to a wide range of materials including Cu, Al, Ti, Be, and TiAl [52–60]; typically, the effects of temperature, route, and tool design have been studied [61]. As mentioned previously in Chapter 1, Figueiredo and Langdon have utilized ECAE to produce Mg alloys that exhibit superplasticity, and Ding et al. refined the grain size of AZ31 to 0.37 μm using a hybrid extrusion route and a reduction in temperature between passes. This "step-down" temperature method has since been used extensively in producing ultrafine grains in Mg [26,27].

Although there is a large body of work in the literature dedicated to characterizing the microstructure of ECAE processed alloys, *a priori* prediction of the processed microstructure remains elusive. In part, this is because the final microstructure is a product of many different factors. Some factors can be controlled, such as temperature, extrusion rate, route, and backpressure. Other factors, such as sidewall friction and outer corner angle, are either difficult to control or not always reported. In addition, although the microstructure from ECAE is supposedly uniform outside of the end regions, there is

little experimental work to confirm the idea [28,62]. Therefore, it was found to be necessary to characterize the pure Mg and AZ31B samples processed at the U.S. Army Research Laboratory (ARL), Aberdeen Proving Ground, MD, in regards to their microstructures and the uniformity of these microstructures along extruded bars.

99.9 *at.*% pure Mg and a commercial alloy, AZ31B, were used for this study. The pure Mg was obtained in an as-cast form from US Magnesium, Salt Lake City, UT, with an initial grain size of approximately 19 mm. Due to this extremely large grain size, the as-cast texture was not quantified. Hot-rolled AZ31B was purchased from Magnesium Elektron - North America, Madison, IL, with an initial grain size of approximately 31 μm and a rolling texture in which the basal planes lie perpendicular to the plate normal.

2.2 Experimental Methods

The as-received materials were machined into billets 19 mm × 19 mm × 152 mm for processing in a sharp 90º Equal Channel Angular Extrusion die. The pure Mg was extruded at 250°C at a rate of 0.381 mm/sec with an applied backpressure of 6.2 MPa (900 psi). The AZ31B was extruded at 200°C at the same rate of 0.381 mm/sec with an applied backpressure of 8.55 MPa (1240 psi). Prior to extrusion, the billets were wrapped in either copper foil for pure Mg or polytetraflouroethylene (Teflon) for AZ31B and they were preheated in the die for approximately 30 minutes. The pure Mg samples inserted into the ECAE had no preferential orientation while the AZ31B samples were inserted into the die such that the basal plane is perpendicular to the transverse direction; see figure 2.1a for schematic of the billet orientation. Both samples were processed by the $4B_C$ route, which consists of 4 passes with a 90° rotation around the long axis after each

path. Deformation in the pure Mg was found to localize under the processing conditions used for AZ31B, and thus a higher temperature had to be used while decreasing the backpressure. The reason for this reduction, and why the backpressure used is lower than what is common in the literature, is due to the design of the ECAE press at ARL. In that press, the sidewalls of the outlet channel only extend approximately 25 mm. The extruded samples are typically much longer than 25 mm and thus excessive backpressure produced a mushrooming effect in the billet. The billets were allowed to cool in air following the extrusion. Unless stated otherwise, all samples in this work were processed in this manner.

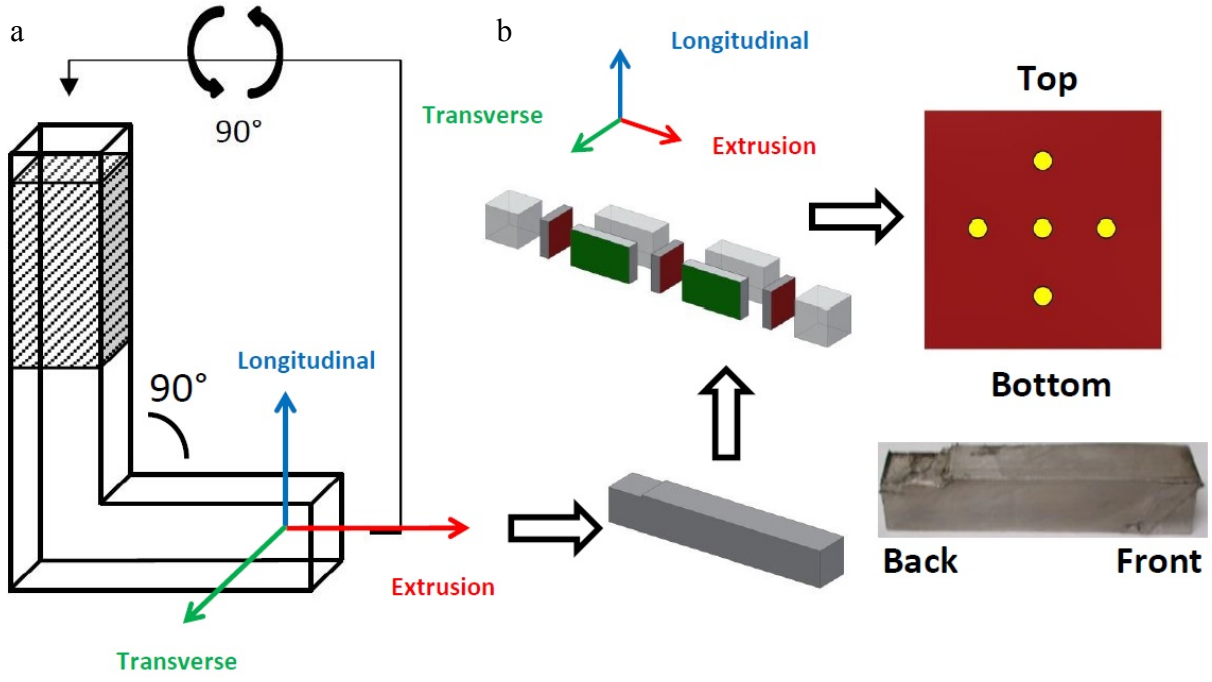

Figure 2.1: (a) Schematic of the ECAE process showing the principal directions in relationship to the tool. (b) Schematic showing the processed billet and the subsequent sectioning. The red and green faces are perpendicular to the extrusion and transverse faces, respectively. Each individual sample had five images taken from it, roughly equi-distant from one another and positioned in a cross pattern as shown by the yellow circles.

Following extrusion, the billets were sectioned with a diamond saw as shown in figure 2.1b. The sample sections with red faces measured 19.05 mm × 19.05 mm × 3.82 mm. The first and last sections, which measured 19.05 mm from the front and rear of the billets, were not characterized because these end regions are known to be only partially plastically deformed, relative to the rest of the billet [58]. The samples on the extrusion plane were given the following designations, relative to the extrusion direction: Front_Ex, Mid_Ex, and Back_Ex. The sample sections on the transverse plane were also given similar designations: Front_Trans and Back_Trans, relative to the extrusion direction. All sectioned specimens were mechanically polished to a 3 μm finish; the AZ31B specimens were polished further to a 1 μm finish. Specimens were sonicated in acetone and then ethanol for 30 seconds each, followed by electropolishing in a Struers Lectropol-5 (Cleveland, OH) for 25 seconds at 25 V. The electrolyte was 5% Nitric acid in methanol that had been chilled to -5 °C to -10 °C. Care was taken to keep the samples in ethanol until immediately prior to inserting them into the SEM. Specimens were mounted in a TESCAN MIRA3 GMU FEG-SEM (Libušina, Czech Republic) and characterized using electron backscattered diffraction (EBSD). Microstructural and texture data were collected at 20 kV and a 120 nm spot size using EDAX TEAM software (Mahwah, NJ). EBSD maps were taken at five locations on each cross-section: in the center and approximately 3.5 mm from the center map as shown in figure 2.1b. Fields of view were chosen to provide approximate 300 grains per image, based on previously obtained optical grain size data (not shown). Using this criterion, pure Mg had a view field of 300 μm while AZ31B had a view field of 100 μm. A 15° of misorientation was used as the definition of a boundary between grains for the purpose of grain size

calculations. The grain size was calculated by multiplying the EBSD step size by the number of pixels in a grain to determine the area of the grain. An average diameter was then calculated from the area as if it were a circle. Grain dilation was applied to the data partitions containing the Inverse Pole Figure (IPF) maps and grain size calculations, but only points with a confidence index greater than 0.1 were used for texture calculations. The method described here for collecting and analyzing EBSD data is typical for the entirety of this work.

2.3 Results and Discussion

2.3.1 Microstructure

Inverse pole figure (IPF) maps, where the grains are colored according to their out of plane crystallographic orientation, can be seen in figure 2.2. After four passes, the microstructure of pure Mg is fully recrystallized, and no evidence of the parent microstructures remains. These microstructures are highly refined compared to the original grain size. The various grain sizes appear to be well distributed, with little evidence of clusters of similarly sized grains. Note that figure 2.2d exhibits a number of elongated grains, which suggests that the process of recrystallization may not have been homogeneous throughout the samples. Table 2.1 details the number average grain size and standard deviation for the five different regions investigated on each sample. The far right column lists the averages all of the average grain sizes for a given cross-section. The standard deviations on the center, top, bottom, etc. averages are very large, even exceeding the average grain size in some cases, and speaks to the heterogeneity of the

recrystallization process. However, the averages for all five locations on a given cross-section vary little and are within statistical agreement across the five cross-sections.

Figure 2.3 displays the distribution of grain size for the center region of all five samples taken from the pure Mg bar. Since the focus is on the homogeneity of the microstructure, number fraction was used to better display outlier grain sizes. Each distribution is wide and contains a long tail; a small number of much larger grains extend beyond the relatively smooth tails. With the possible exception of the Figure 2.3a, the grain size distributions do not exhibit a clear demarcation between recrystallized and non-recrystallized grains.

Figure 2.4 contains misorientation angle distributions from the center of the Front_Ex, Middle_Ex, Back_Ex, Front_Trans, and Back_Trans samples of pure Mg. The black lines indicate misorientation angles between each of the grains and their nearest neighbor grains, which are termed correlated misorientations. The red lines are the misorientation angles between all possible point pairs of grains in the image, not including edge grains, and are called uncorrelated misorientations. The peak near 30° is immediately noticeable, and occurs in both the correlated and uncorrelated data. This peak in the uncorrelated data meets or exceeds the peak in the correlated data. Low angle misorientations make up a large number fraction of the correlated data, and several images also show a peak in the correlated data around 86º. This indicates that there are both long and short-range orientation relationships between the grains.

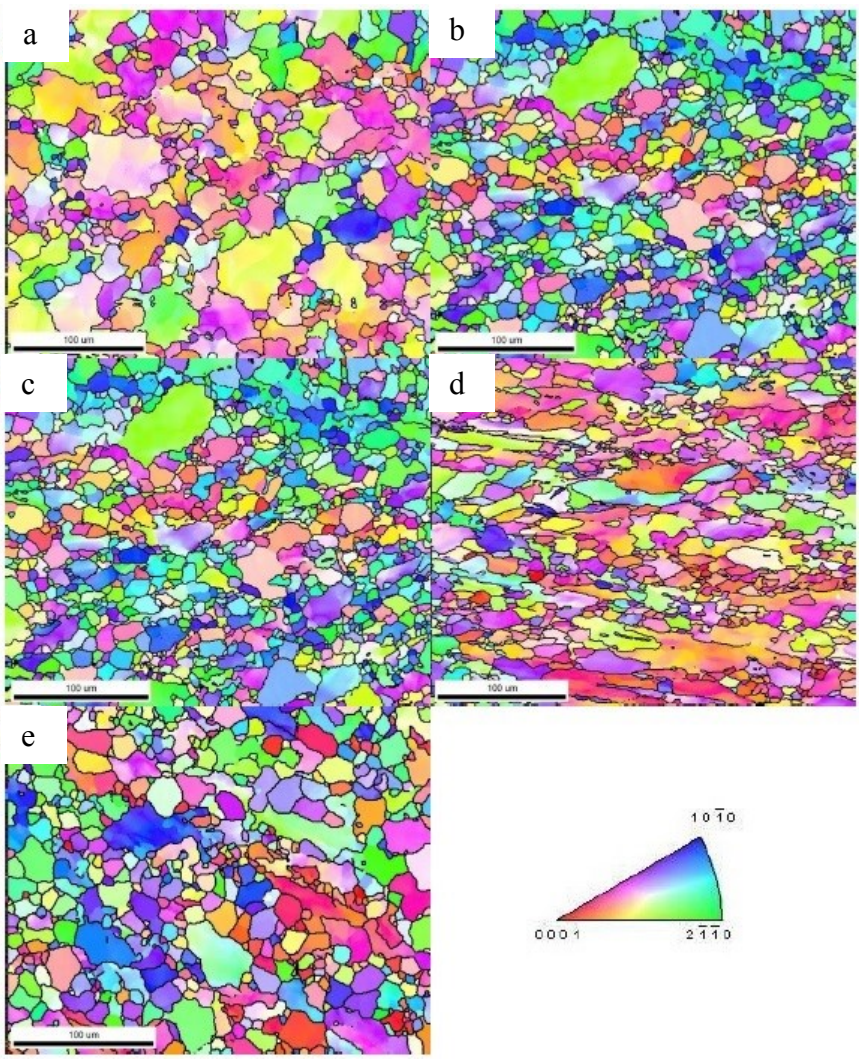

Figure 2.2: Inverse Pole Figure maps from the center of each pure magnesium sample (a)Front_Ex (b)Mid_Ex (c)Back_Ex (d)Front_Trans (e)Back_Trans. The black line indicates high angle grain boundaries (greater than 15° misorientation).

Location	Center	Top	Bottom	Left	Right	Average
Front_Ex	8.61 ± 7.77	9.51 ± 7.96	10.76 ± 10.36	10.04 ± 10.88	11.26 ± 11.17	10.04 ± 0.93
Middle_Ex	7.77 ± 6.83	8.73 ± 6.79	9.99 ± 8.28	8.86 ± 5.76	7.03 ± 6.44	8.48 ± 1.01
Back_Ex	7.75 ± 5.77	7.44 ± 6.22	8.87 ± 6.91	7.47 ± 7.07	9.89 ± 8.59	8.28 ± 0.96
Front_Trans	7.87 ± 7.92	7.79 ± 7.82	7.74 ± 6.63	8.85 ± 7.74	10.16 ± 8.34	8.48 ± 0.93
Back_Trans	9.97 ± 7.73	7.21 ± 5.43	10.29 ± 8.21	10.17 ± 7.48	7.52 ± 5.88	9.03 ± 1.37

Table 2.1: Number average grain size and standard deviation for pure magnesium

Inverse Pole Figure (IPF) maps for the AZ31B samples are shown in figures 2.5 and 2.6. Like that for the pure Mg samples, the microstructure is fully recrystallized, but there is no evidence of elongated grains that were observed for pure Mg. The grains are more refined than in the pure Mg and have an average grain size of about 2.5 μm (Table 2.2). AZ31B displays a narrower distribution in grain size (figure 2.7), but shows a similar degree of variation in the mean grain sizes. The dark regions in the IPF maps could not be indexed and are attributed to the presence of precipitates. Across all of the imaging only one exception to refined grain structure was observed and it is the very large grain shown in figure 2.6. Given the undulated nature or serration of the associated grain boundary, it is likely that the large grain in figure 2.6 was broken down fully during the extrusion process and is not the product of abnormal grain growth.

Figure 2.8 displays the misorientation angle distribution graphs for the AZ31B samples. Like pure Mg, there exists a peak around 30° in both the correlated and uncorrelated data, although this peak is not as pronounced in the uncorrelated data. Most of the AZ31B samples have a large number of low angle misorientations in the correlated distributions, but the number fraction is not as large as it is for the pure Mg samples.

Both pure Mg and AZ31B have large variations in grain size within a given image with the standard deviations being approximately 90% and 50% of the mean, respectively. This speaks to the local heterogeneity of the recrystallization process. However, the image average grain sizes show little variation both across the samples and throughout the bars. The sample averages (which are the averages of all of the image averages) generally fall within two standard deviations of one another. Thus, the refined grain size for both pure Mg and AZ31B can be considered fairly homogenous throughout

the fully worked region of the bars. However, as might be expected from time and temperature controlling grain size, the sample average grain size does increase on moving from the back to the front of the extruded bar, 21% for the pure Mg bar and 36% for the AZ31B bar.

Based on the EBSD maps, both pure Mg and AZ31B undergo significant grain refinement during the extrusion process, with the AZ31B bar developing a smaller grain size and a narrower grain size distribution. This can be attributed, in part, to AZ31B's lower processing temperature, as well as the presence of Al-Mn precipitates, which are known to be grain refiners [63]. However, the morphology of the grains suggests that there may also be a difference in the active mechanisms of recrystallization, which also plays a role in the development of the microstructure.

Many of the larger grains in pure Mg, such as those shown in figure 2.9, display both serrated grain boundaries and grain boundary bulging, which are typical indicators of discontinuous dynamic recrystallization (dDRX) [46]. Further evidence of dDRX is given by a strong non-uniformity in the development of the substructure in the incompletely recrystallized

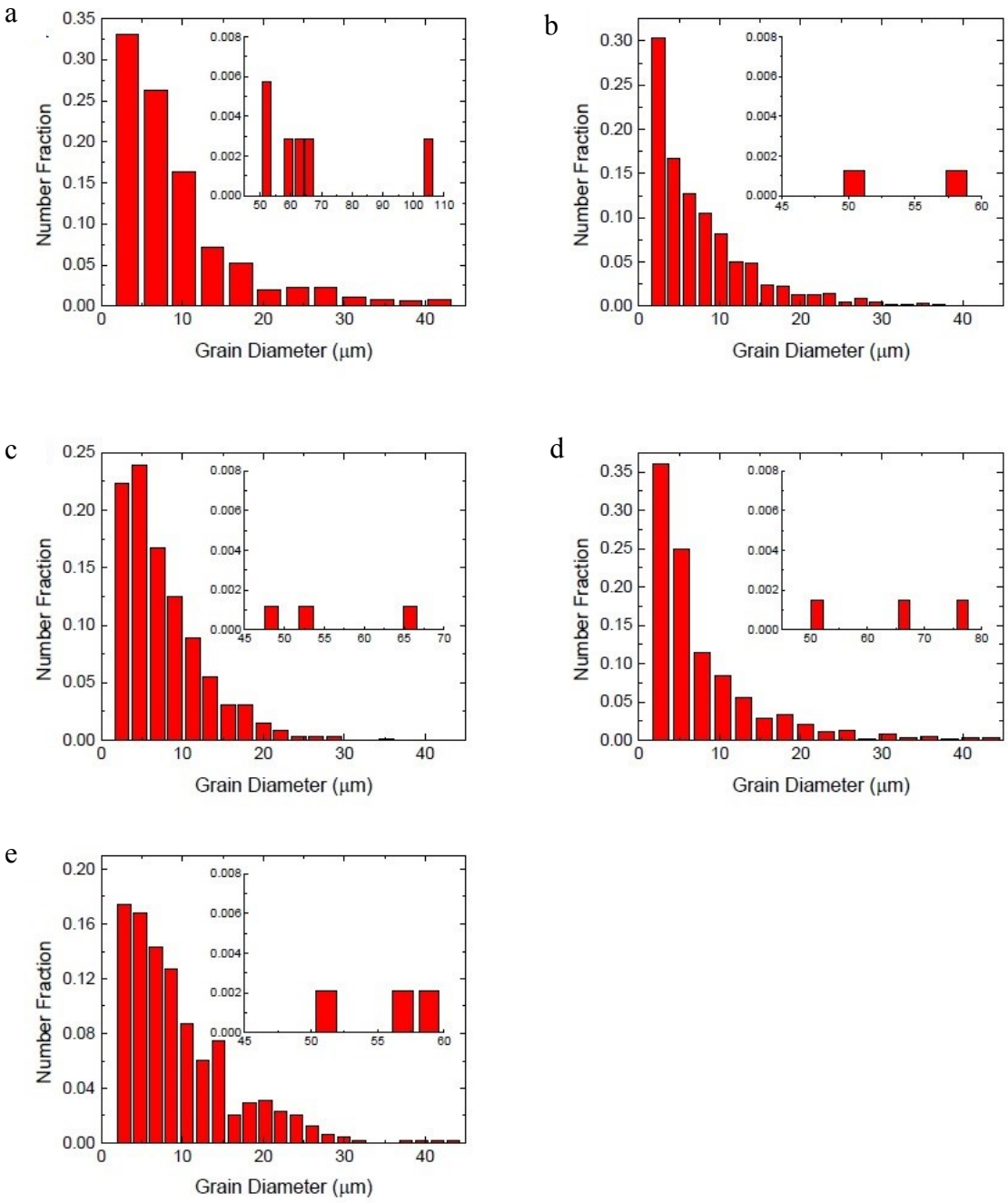

Figure 2.3: Grain size distributions from the center of each pure Mg sample (a) Front_Ex, (b) Mid_Ex, (c) Back_Ex, (d) Front_Trans, and (e) Back_Trans. Grains that were several times the mean were added as an inset.

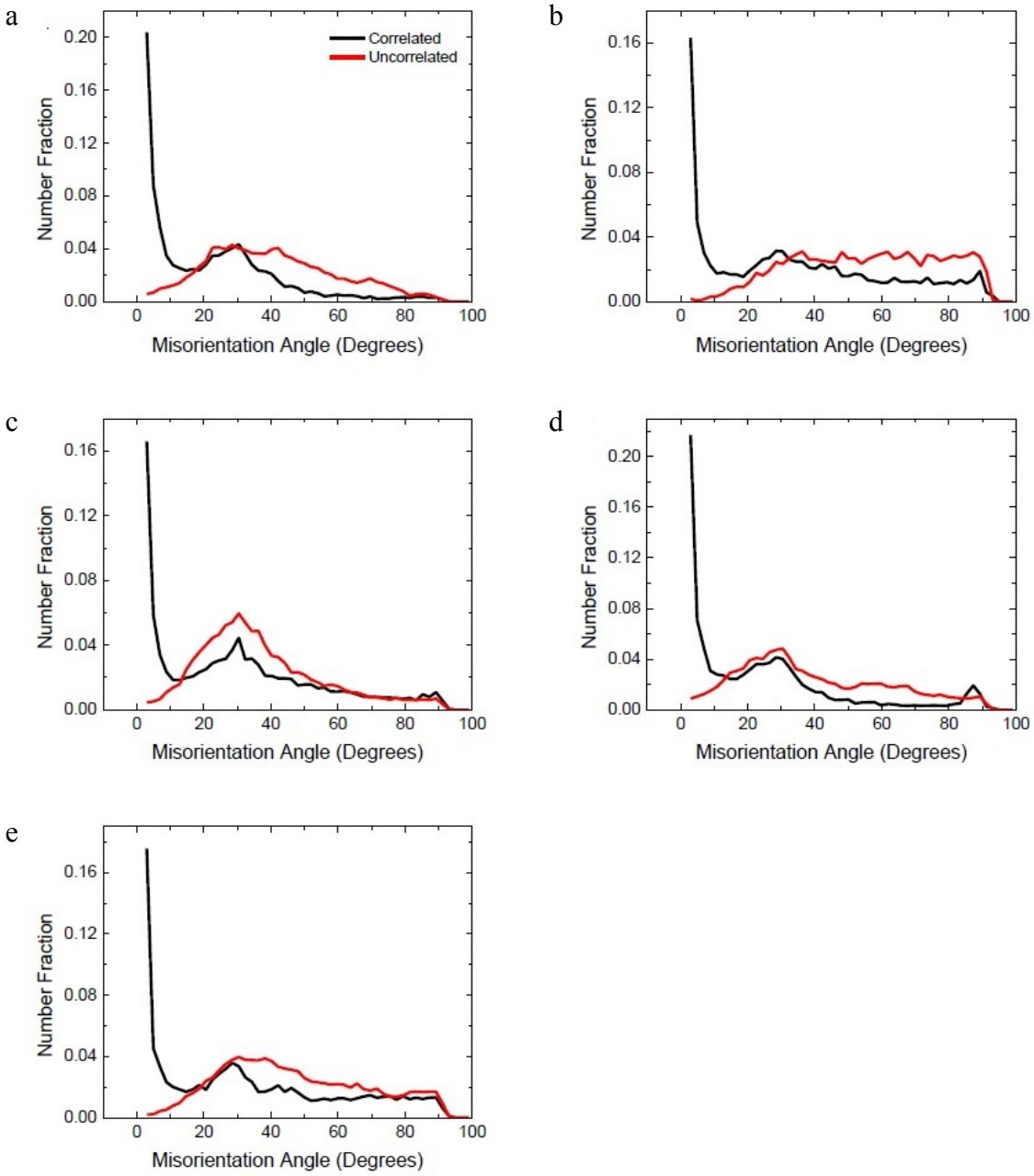

Figure 2.4: Misorientation angle distributions from the center of each pure magnesium sample (a) Front_Ex, (b) Mid_Ex, (c) Back_Ex, (d) Front_Trans, and (e) Back_Trans.

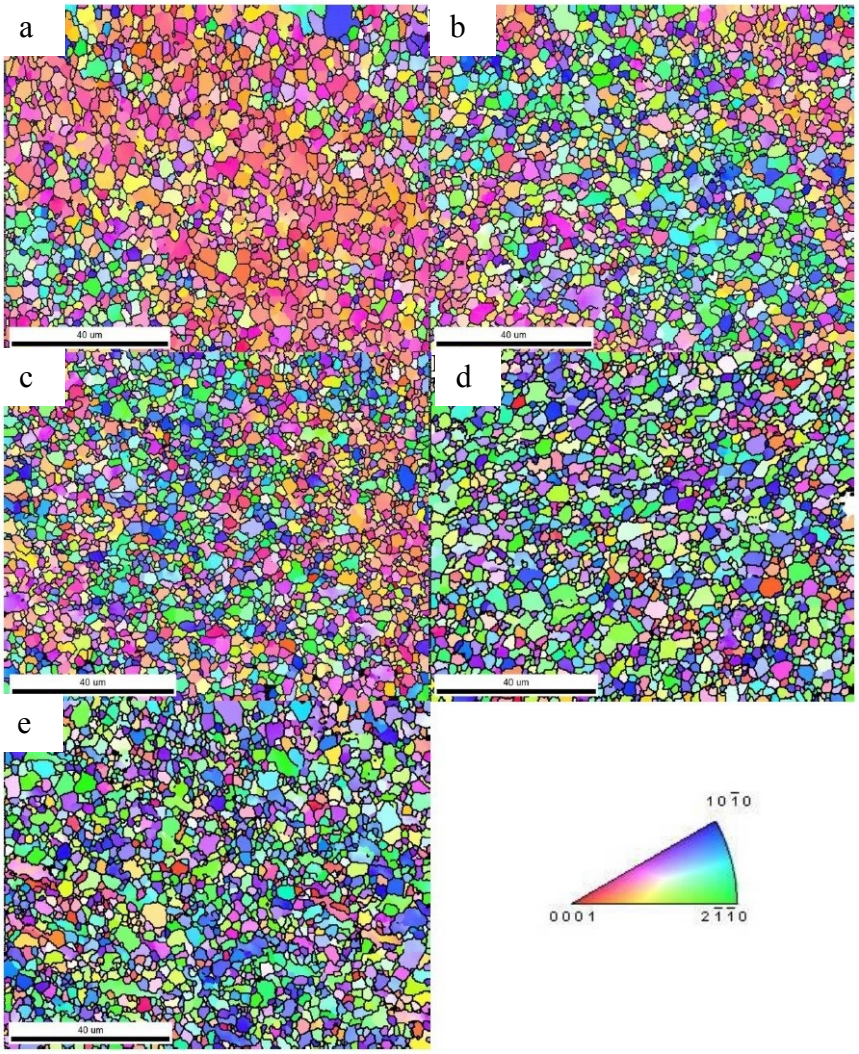

Figure 2.5: Inverse Pole Figure maps from the center of each AZ31B sample (a) Front_Ex, (b) Mid_Ex, (c) Back_Ex, (d) Front_Trans, and (e) Back_Trans.

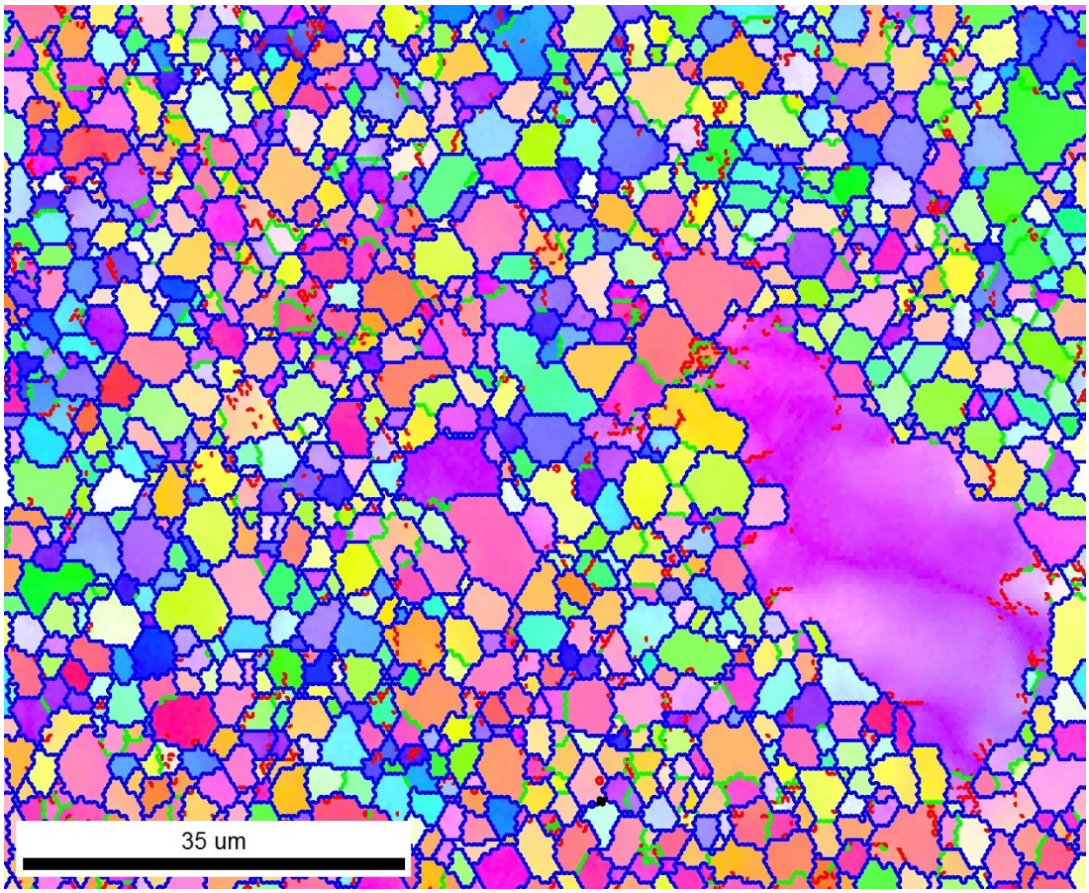

Figure 2.6: AZ31B Front_Ex Left IPF map. Red lines indicate low angle boundaries with misorientations of 2-5°, green lines indicate medium angle boundaries with misorientations of 5-15°, and blue lines indicate high angle boundaries of >15°.

Location	Center	Top	Bottom	Left	Right	Average
Front_Ex	2.41 ± 1.58	3.02 ± 1.46	3.12 ± 1.80	2.99 ± 1.88	2.64 ± 1.37	2.84 ± 0.27
Middle_Ex	2.23 ± 1.30	2.14 ± 1.08	2.24 ± 0.99	2.59 ± 1.31	2.50 ± 1.15	2.34 ± 0.17
Back_Ex	1.93 ± 0.89	2.14 ± 1.04	2.30 ± 1.21	1.75 ± 0.94	2.32 ± 1.25	2.09 ± 0.22
Front_Trans	2.25 ± 1.20	2.49 ± 1.29	2.44 ± 1.48	2.89 ± 1.71	2.34 ± 1.41	2.54 ± 0.21
Back_Trans	2.23 ± 1.27	2.32 ± 1.34	2.18 ± 1.17	2.34 ± 1.55	2.40 ± 1.31	2.29 ± 0.08

Table 2.2: Number average grain size of AZ31B samples in micrometers.

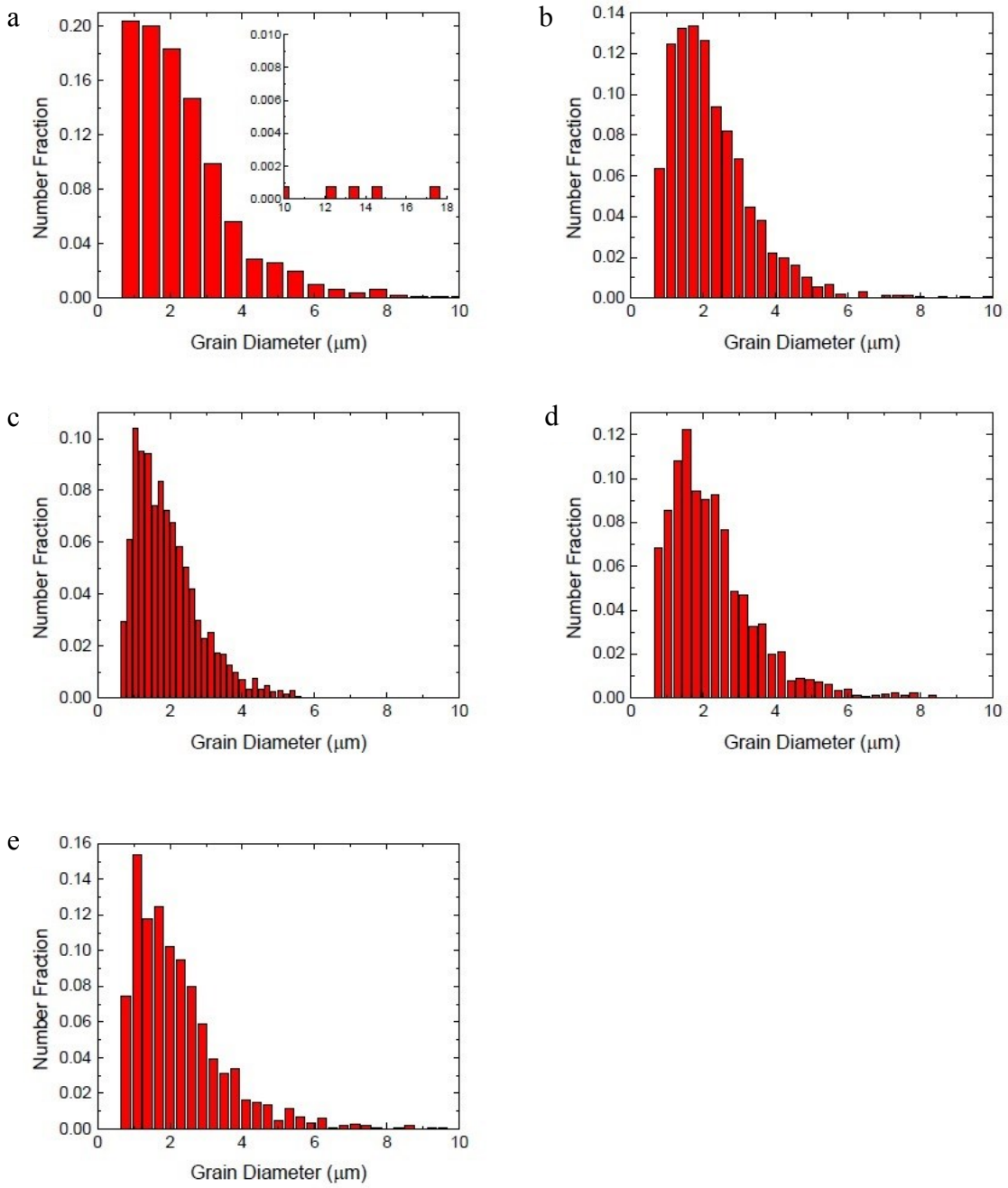

Figure 2.7: Grain size distributions from the center of each AZ31B sample (a) Front_Ex, (b) Mid_Ex, (c) Back_Ex, (d) Front_Trans, and (e) Back_Trans. Grains that were several times the mean were added as an inset.

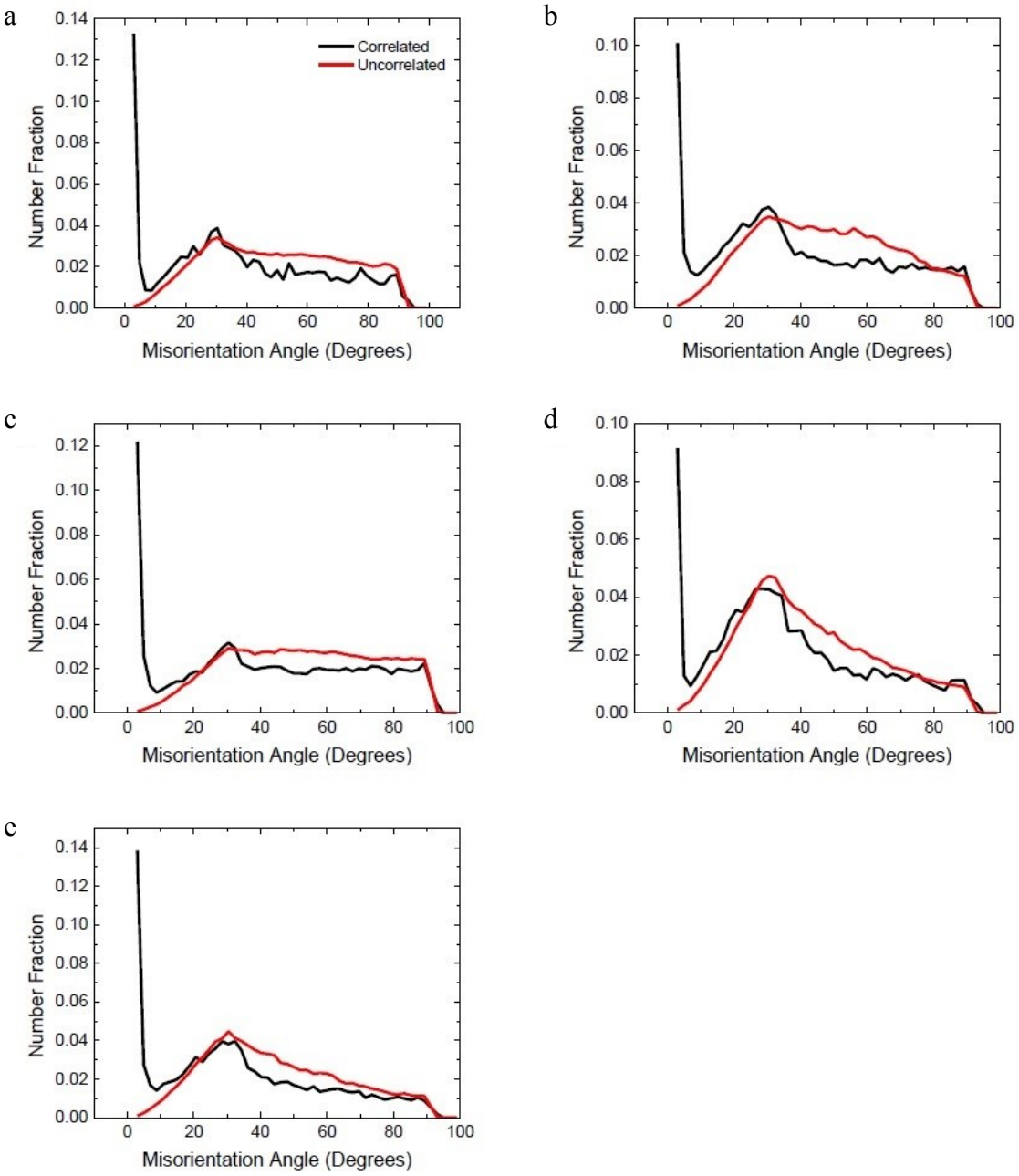

Figure 2.8: Misorientation angle distributions from the center of each AZ31B sample (a) Front_Ex, (b) Mid_Ex, (c) Back_Ex, (d) Front_Trans, and (e) Back_Trans.

grains in figure 2.9 [46]. However, figure 2.9 also displays an area where grains have recrystallized near a grain boundary rather than at a grain boundary. This suggests that recrystallization in pure Mg may also occur by continuous dynamic recrystallization (cDRX), where misorientation increases due to the accumulation of dislocations at subgrain boundaries rather than just at high angle boundaries [48]. The presence of indicators for both dDRX and cDRX suggests that the two recrystallization processes may be competing in pure Mg, although dDRX has stronger indicators and, therefore, is likely to be more active.

In contrast to pure Mg, the few abnormally large grains that appear in AZ31B, such as the one shown in figure 2.6, exhibit serrated grain boundaries and could indicate that dDRX is active. However, as Barnett et al. have shown, the presence of serrated grain boundaries does not exclude the activation of cDRX [48]. In fact, they conclude that both dDRX and cDRX are active in AZ31B [48]. In figure 2.6 we see evidence for cDRX. Note the subgrain that appears in the lower right hand corner of the large grain. It is offset from the grain boundary and has a significant misorientation relative to the large grain. Its location and comparatively large misorientation suggest the activation of cDRX. Further still, the relative absence of low and medium angles boundaries in AZ31B, compared to pure Mg, suggests that the recrystallization process occurs more homogeneously than in pure Mg and provides additional evidence that cDRX dominates in AZ31B. Taken together, this evidence suggests that cDRX is more active in AZ31B than dDRX. Lastly, we note that a homogeneous grain structure cannot easily undergo long-range grain growth and this could partially account for the smaller grain size observed in the AZ31B samples.

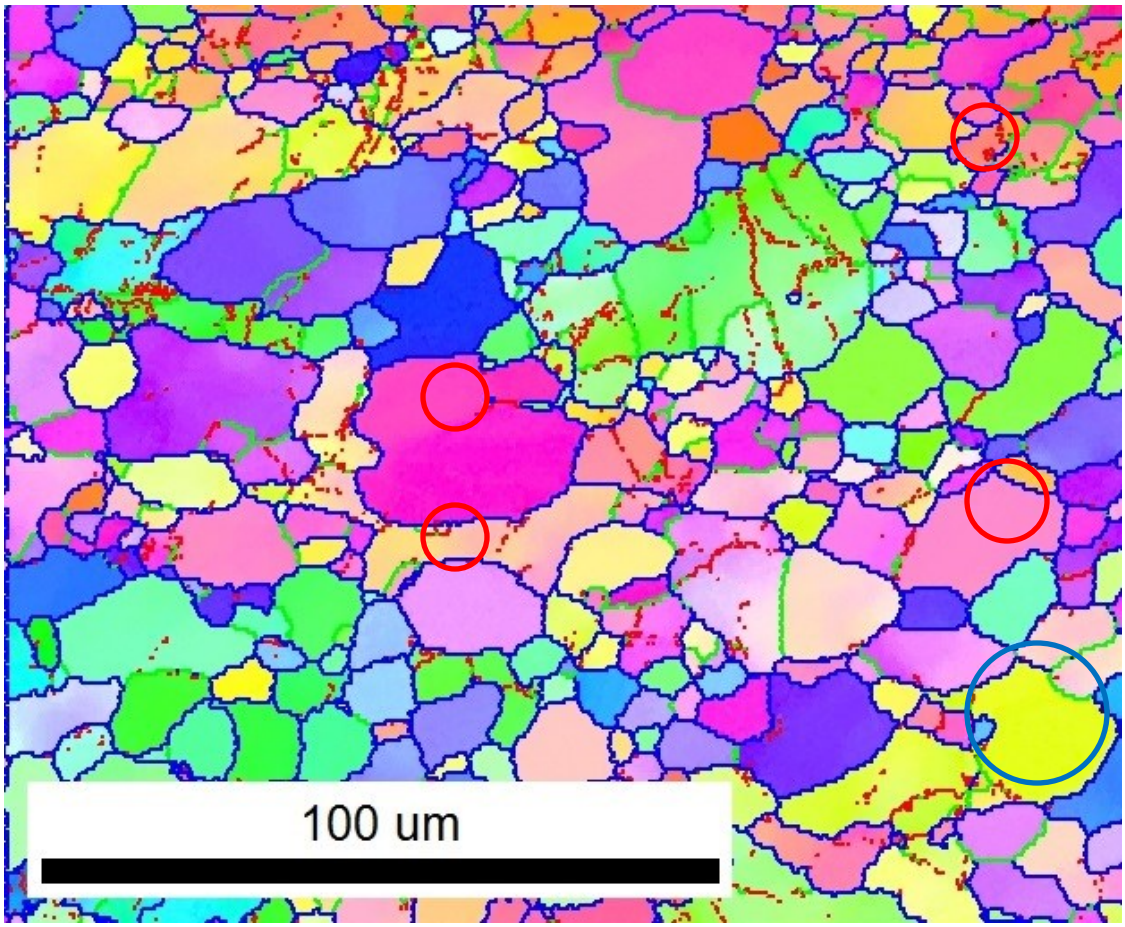

Figure 2.9: IPF map of sample Pure Mg_Back_Ex_Right. Red lines indicate low angle boundaries with misorientations of 2-5°; green lines indicate medium angle boundaries with misorientations of 5-15°; and blue lines indicate high angle boundaries of >15°. Red circles show areas where medium or low angle boundaries have formed behind a bulged boundary. The blue circle contains an area where grains have recrystallized away from the high angle boundary and are surrounded only by medium and low angle boundaries.

Typically, the elongated grains that are seen in several of the pure Mg samples appear on the transverse planes. Given that the shear direction is contained within the transverse plane, it is not unexpected for heavily deformed and elongated grains to appear in the transverse images [58]. Since the initial grain size of the pure Mg was very large, these likely are not the remnants of the original grains, but an older generation of recrystallized grains from a prior pass that are being broken down.

Most of the misorientation angle distribution charts for both pure Mg and AZ31B display peaks around 30°. This has been observed a number of times in previous studies and has been attributed to dislocation motion during the recrystallization process [64–66]. The peak around 86° that is frequently observed in pure Mg and only occasionally in AZ31B is likely the $\{10\bar{1}2\}\langle 10\bar{1}1\rangle$ tensile twin system which has approximately an 86° misorientation with respect to the matrix. There are two likely explanations for this observation. The first is that these are remnants of twins in the microstructure that have yet to be fully recrystallized. The second possibility is that during dDRX, when the grain boundaries bulge, new grains are nucleated by twins propagating across the bulged area [46]. The fact that the 86° peak is infrequently observed in the AZ31B may be attributable to the difference in grain size, which is known to impact the ease with which twins nucleate. Both pure Mg and AZ31B contain a significant number of low angle boundaries, which is typical of materials that have been recrystallized.

2.3.2 Texture

A harmonic series expansion with a Gaussian half-width of 5° was used to calculate the pole figures shown in figures 2.10 and 2.11 for the pure Mg samples. The pole figures were normalized to a maximum intensity of 20 times above random to best compare texture variations between pole figures. The pole figures generally display the basal fiber texture typical of Mg processed by the $4B_C$ ECAE route where the basal poles are approximately 45° away from the extrusion direction, and the prismatic pole figure shows little to no texturing. The variations in the fiber texture do not appear to be systematic with respect to the location within the bar. However, two aspects of these

variations should still be noted. The increase in the peak intensities observed in the prismatic pole figure for the Bottom map of the Back_Trans sample suggests that this section had significant prismatic slip, while the Top and Center maps of the Back_Ex sample are notable for being more heavily textured towards the longitudinal direction than the other samples. Some clustering of basal and prismatic textures can be observed in figures 8b and c.

AZ31B pole figures were calculated in the same manner as for pure Mg and are shown in figures 2.12 and 2.13. By comparing the pole figures for AZ31B and pure Mg one can see that there is less smearing of the fiber texture in AZ31B than in pure Mg. The contribution of prismatic slip to the texture is also observed less frequently and to a lesser degree than was seen in the pure Mg Back_Trans Bottom pole figure. However, pole splitting is common which matches observations reported by others researchers [27,67]. The maximum intensity of the pole figures is frequently within a few degrees of 45° relative to the extrusion direction. Given that the angle between the fiber texture and the extrusion direction is tightly clustered in pole figures from the same specimen and given that maps from the same sample were taken at one time, the deviations from 45° are more likely attributable to samples not being mechanically polished perfectly parallel to the billet orientation, than they are to microstructural evolution during processing. As with pure Mg, some degree of short-range texture clustering can be observed in figures 2.5a, b, and c.

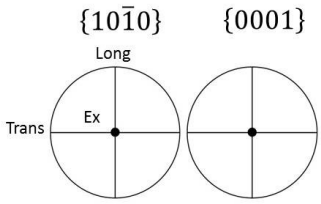

99.9% Pure Mg	Front_Ex	Mid_Ex	Back_Ex
Center			
Top			
Bottom			
Left			
Right			

Figure 2.10: Pole figures for the pure Mg extrusion direction samples. Maximum intensity was normalized to 20 times above random.

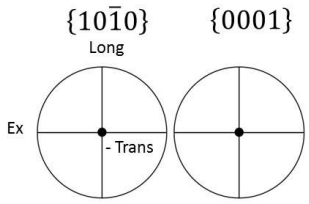

99.9% Pure Mg	Front_Trans	Back_Trans
Center		
Top		
Bottom		
Left		
Right		

Figure 2.11: Pole figures for the pure Mg transverse direction samples. Maximum intensity was normalized to 20 times above random.

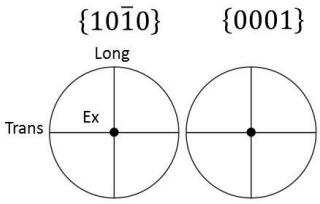

AZ31B	Front_Ex	Mid_Ex	Back_Ex
Center			
Top			
Bottom			
Left			
Right			

Figure 2.12: Pole figures for the AZ31B extrusion direction samples. Maximum intensity was normalized to 20 times above random.

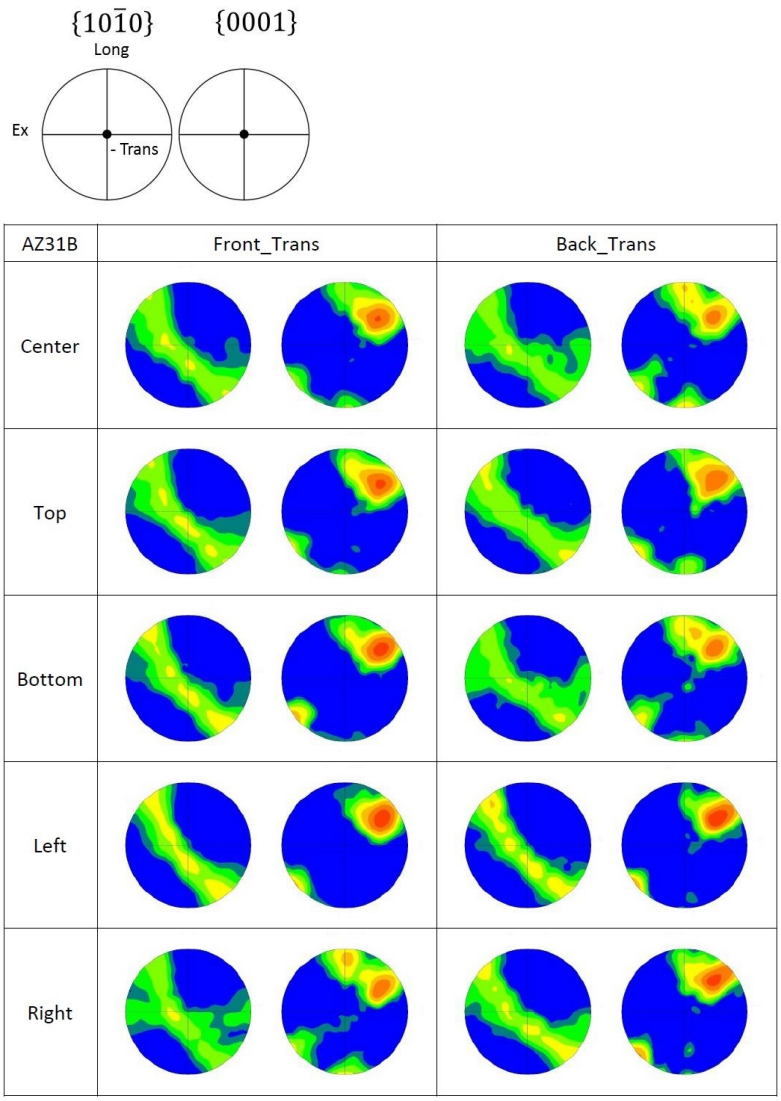

Figure 2.13: Pole figures for the AZ31B transverse direction samples. Maximum intensity was normalized to 20 times above random.

Similar to the results for grain size, there is a larger degree of variation in the texture of the pure Mg than that in the AZ31B. During ECAE, the AZ31B basal poles consistently adopt to the typical $4B_C$ deformation texture where the basal poles are approximately 45° from the extrusion axis; although, not necessarily at the ideal 45° vertical disinclination from the extrusion axis [64,68]. It should be noted that this result differs from the texture reported by Suwas et al., Yapici et al., and Agnew et al. with

regards to the extent of inclination from vertical axis [37,62,64]. Some instances of pole-splitting are also observed. However, there are significant qualitative differences between the pure Mg and AZ31B textures. Although the basal poles are generally the same angle away from the extrusion direction, the basal poles in pure Mg may vary significantly in their orientation relative to the transverse and longitudinal axes. In figure 2.10, orientations that are slightly longitudinal axis biased, transverse axis biased, and longitudinal axis biased are all observed. However, maximum intensities for the pure Mg are similar to those for the AZ31B samples. The IPF images show that both pure Mg and AZ31B exhibit some localized texture clustering. This clustering can be seen in SEM images as electropolishing produces some orientation dependent etching. The SEM images show that the clustering appears fairly uniform throughout the samples. These clusters suggest the activation of cDRX which tends to preserve the parent texture. Some texturing in the prismatic plane was also observed in the pure Mg samples, indicating activation of prismatic slip. The activation of prismatic slip in the as-cast pure Mg, but not in the hot-rolled AZ31B show similarities to the results reported by Agnew et al., where AZ31B which had been initially extruded did not show prismatic texturing after ECAE processing, but the as-cast AZ31B did [69]. As the as-cast microstructure is presumably more random, it is expected that some grains have an orientation where prismatic slip is preferred over basal slip. Therefore, depending on the microstructural evolution and spatially local mechanism of DRX, the preference for prismatic slip may be preserved through multiple ECAE passes.

2.4 Conclusions

This project accomplished its stated goals: the microstructures of pure Mg and AZ31B were characterized and found to be largely homogeneous along the length of the bar. Moreover, the many microstructural differences between the two materials suggest that while the microstructural evolution is similar for both materials, significant differences in the final microstructures appear, suggesting differences in the fundamental mechanisms that are activated. To some degree, the two materials highlight the potential benefits of the dDRX and cDRX mechanisms. The pure Mg microstructure had larger and more variable sized grains, but also a more randomized texture that can result in enhanced ductility. In contrast, the AZ31B had a more consistent texture, which may lead to greater anisotropy in properties, but the grain size was on average, smaller and with a narrower distribution. The characterization work performed here provides a baseline for the following work not only in the anticipated microstructures, but also in the activation and coarse behavior of the grain refinement mechanisms. As an ongoing part of this work, 29 billets of materials produced here have been distributed to 8 principal investigators.

2.5 Appendix: ECAE Extrusion Procedures

Given the strong reliance in this work on ECAE, it may prove useful to elaborate on extrusion preparation and procedures. Beginning with preparation of the sample for extrusion, the sample should be sectioned to ¾" x ¾" x 6-8" and ground to fit within the die. It should be noted that given the short exit channel on the press at ARL, the billets will tend to form a mushroom shape beyond the exit channel, and the excess material will

need to be removed prior to further extrusions. Thus, the final extruded billet will invariably be shorter than the initial billet with the difference in length increasing with number of passes, temperature, and backpressure. In the case of AZ31B, it was found to be useful to wrap the billet in a sheet of Teflon to improve lubrication and prevent leaving flash on the sidewalls. However, the Teflon sheets tended to be taken up into the billet in the case of 99.9% pure Mg. Instead, wrapping the billet in thin copper foil was a suitable substitute. Immediately prior to insertion into the tool, the billets were covered in lubricant. For the temperatures used here, Loctite Brand Silver grade anti-seize compound (Henkel Company, Düsseldorf, Germany) was found to be adequate.

After insertion into the heated tool, the billet was allowed sufficient time to reach the extrusion temperature. Once the billet temperature had equilibrated, the extrusion was allowed to begin. For high temperature extrusions, it was often quicker to preheat the billet in a furnace before transferring it to the tool. Extruded billets were ejected from the ARL press by disconnecting the backpressure and removing the bottom sliding wall. Billet ejection was aided by slightly overextending the punch into the outlet channel so that none of the billet material remained in the inlet channel. A scraper was used to wrench the billet loose if the billet remained adhered to the sidewalls. Following extrusion, the billets were allowed to cool in air. A small number of experiments were carried out where the billets were quenched in oil instead of air. The resulting average grain size was found to be somewhat larger than that in the air quenched samples. The effect was believed to be due to the inhibition of post-dynamic recrystallization processes. Some evidence for this conclusion can be seen in Chapter 6.

2.6 Appendix: AZ31B Precipitates

According to the ASM handbook, the chemical composition for AZ31B is 2.5-3.5% Al, 0.2% Mn min, 0.6-1.4% Zn, 0.04% Ca max, 0.10% Si max, 0.05% Cu max, 0.005% Ni max, 0.005% Fe max, 0.30% max other (total), and the balance is Mg [70]. Although Mn is ostensibly added to improve corrosion resistance, its propensity to form intermetallics with Al has secondary effects on microstructural evolution and performance [70]. The largest precipitates observed in AZ31B are called "stringers" in this work for their long rod-like shapes; although they are generally fractured into many smaller pieces by the rolling and ECAE processes, as seen in figure 2.14. Figure 2.14b shows that the stringers do not have an apparent preferred orientation. EDS analysis of these stringers have shown them to consist mostly of Mn and Al with some Fe [45]. The role of stringers in the spall behavior in AZ31B will be discussed in greater detail in Chapter 4.

A second type of precipitate, roughly 500 nm in diameter, can be seen as bright spots interspersed among nanovoids in figure 4.5. Although the chemical composition of these precipitates were difficult to identify through conventional EDS, they were identified as Al-Zn precipitates with High-Angle Annular Dark-field Scanning Tunneling Electron Microscopy (HAADF-STEM) [71].

The smallest precipitates that have been observed in AZ31B are on the order of 50 nm in diameter, and are believed to be Al_8Mn_5 [72]. These precipitates are thought to inhibit recrystallization by pinning the boundaries of fine, recrystallized grains [72].

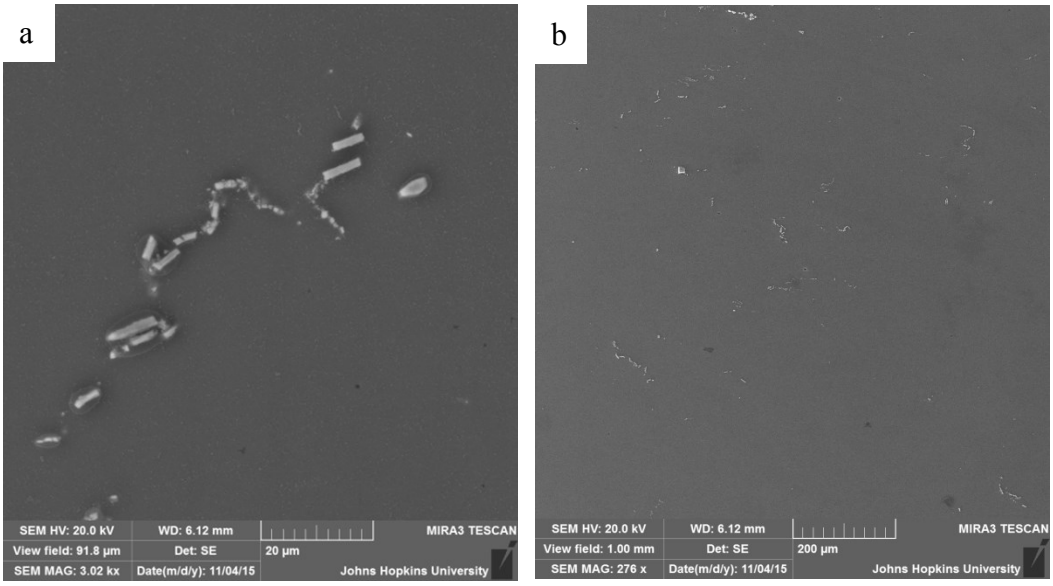

Figure 2.14: Secondary electron SEM micrographs of Mn-Al "stringer" precipitates in ECAE processed AZ31B. (a) Image of fractured stringer precipitate. (b) Large view field showing many stringer precipitates.

2.7 Appendix: Polishing Methods

A number of polishing methods were employed in this work to prepare magnesium samples for EBSD or SEM microscopy. The most useful methods are discussed below.

For high resolution SEM imaging, the samples were first polished to 1200 grit with SiC. This was followed by polishing steps with 3 µm and 1 µm diamond suspensions. Between steps, the samples would be rinsed with water to remove residual particles. Following the 1 µm step, ethanol was used instead of water to rinse the samples. 50 nm colloidal silica was used for the final polishing step instead of alumina, as alumina tends to etch Mg-Al alloys. The silica particles were found to readily adhere to the surface upon drying, after which time they could not be removed without further

polishing. To prevent silica adhesion, it was necessary to fully rinse the sample with ethanol and then sonicate in fresh ethanol immediately following polishing.

For electropolishing, 5% Nitric acid in methanol was found to be a good general purpose electrolyte, which could be adapted for use with pure Mg, AZ31B, or AMX602. Methanol was used in place of the more readily available ethanol for safety reasons; 5% Nitric Acid in ethanol is too volatile to store safely. Prior to electropolishing, the samples were mechanically polished. Pure Mg, lacking large inclusions, was polished to 1200 grit with SiC, and then to 3 μm with a diamond suspension. AZ31B and AMX602 were further polished to 1 μm to minimize the electropolishing time, and thus the electrochemical attack at inclusion interfaces. Mechanical polishing was followed by an acetone rinse and sonication in ethanol. The electrolyte was chilled to around -10°C before use. Initially, this was done with an ice-brine bath for approximately 90 minutes. This was found to be unnecessarily time-consuming, and eventually, liquid nitrogen was poured into the electrolyte instead. Pure Mg samples were electropolished at 18-19V for 40s; while AZ31B was polished at 22 V for approximately 16 s. Samples were then *immediately* thoroughly rinsed with ethanol to minimize chemical attack, and kept in a beaker of fresh ethanol until ready for insertion into the chamber.

In some cases, where electropolishing was not appropriate, such as during the examination of spalled AZ31B where the electrolyte would damage the voids, an ion milling method was developed. A number of different mills were used, but they all provided similar results. The sample was first polished to 50 nm using the procedure described above. In the ion mill, a recipe of 5kV for 3-5 minutes, 3kV for 15 minutes, 1kV for 20 minutes, and 0.5kV for 20 minutes was used. The final 0.5kV step was

observed to produce a distinct improvement in EBSD data collection. If the ion mill did not possess a cold finger, the sample was allowed to cool in low vacuum for 10 minutes, as a precaution against heating the sample too much. After milling the samples were kept in ethanol or under vacuum until ready to insert into the SEM.

2.8 Appendix: EBSD Analysis

It is not uncommon, particularly for Mg, for the EBSD data collection software to mis-index points along the grain boundary, due to the overlap of the Kikuchi patterns. These mis-indexed or "noisy" points may impact the analysis in a number of ways. They reduce the apparent grain size, break up the actual grain boundaries, and introduce random orientations into the texture calculations. As a consequence, the mis-indexed points are generally dealt with in post-processing prior to any analysis. There are many methods to "clean up" the microstructure, including Grain Confidence Index (CI) Standardization, Neighbor CI Correlation, and Neighbor Orientation Correlation. The method preferred in this work is Grain Dilation. During Grain Dilation, a grain tolerance angle and a minimum grain size (in number of data points) are defined, and points within the tolerance angle of each other are grouped into grains. Points that do not belong to any grain are then partitioned to adjacent grains and assigned the orientation of that grain. It is highly unlikely that any EBSD map of sufficiently high resolution has many grains that consist of only 2 or 3 points. An average grain in an EBSD map should contain approximately 20 or more points. Therefore, it is prudent to set a minimum grain size to at least 6-8 points. Another consideration during Grain Dilation is how many clean up iterations to run. Frequently, it is acceptable to allow the software as many iterations as

necessary to, for instance, clean up a small group of noisy points at a triple junction. However, and this is a pitfall of the grain dilation method, care must be taken not to introduce artifacts into the microstructure. Suppose the microstructure contains a number of voids which are unable to be indexed, allowing Grain Dilation to run to completion would entirely fill in the voids. It is entirely possible to run Grain Dilation on a map that is mostly noise and create a microstructure that *appears* realistic and believable. For this reason, where precipitates or voids appear in this work, Grain Dilation was limited to only a single iteration, if used at all.

For texture calculations, there was a concern both that noisy data points would artificially reduce the strength of the measured texture, and that removing the noisy data with Grain Dilation could artificially increase the strength of the measured texture. It was decided to remove all points that had a CI less than 0.1 from the texture calculations under the assumption that low CI points were randomly distributed with regards to orientation.

3. Mechanical Behavior of Rolled and ECAE Processed AZ31B

3.1 Introduction

The discovery that ECAE methods can enhance the mechanical properties of magnesium alloys has generated intense study of both the ECAE method and the mechanical properties of ECAE processed magnesium under various testing conditions. The proclivity of magnesium alloys to twin and undergo DRX makes the mechanical response complex. However, the general trends are well known. Strain along the $\langle c \rangle$ axis must be accommodated either by twinning or by $\langle c + a \rangle$ slip, and the $\{10\bar{1}2\}$ twin is easier to activate than $\langle c + a \rangle$ during $\langle c \rangle$ axis extension. The activation of the $\{10\bar{1}2\}$ twin system has been shown to enhance the ductility in magnesium, a common effect of twins in hcp materials [3,9]. Extension twinning frequently produces a sigmoidal stress strain curve; where a low strain hardening plateau is followed by a rise in the rate of strain hardening [9,73–75].

Three potential causes are typically attributed to the increase in strain hardening following twinning: twin boundary hardening from twin boundaries acting as dislocation barriers, geometric hardening from the reorientation of the lattice, and the Basinski mechanism [75]. The Basinski mechanism is an increase in hardening due to glissile dislocations converting into sessile dislocations, following the twin shear transformation [75–77]. Knezevic et al. argue that the dominant hardening mechanism is due to reorientation of the twinned lattice into orientations more difficult for slip, as the twins tend to totally consume the parent grains – eliminating any additional strengthening effect from the twin boundaries. The presence of twins is a reccurring feature at both quasi-static rates and higher rates, and at higher rates, this includes fine microstructures where

twinning is predicted to be difficult [9,73–75,78–81]. A number of studies have found evidence of strain-rate dependent deformation in magnesium alloys processed via Equal Channel Angular Extrusion (ECAE) methods, with the work by Li et al. covering the largest range of strain rates from 10^{-4} to 10^{3} [79–81]. In addition, Tucker et al. have reported considerable strain rate effects in an AZ31B plate tested at both quasi-static and dynamic rates [82].

Here, we investigated the mechanical properties and microstructural evolution of rolled and ECAE processed AZ31B under quasi-static rates. The intent was to determine how orientation and microstructure impact strain-rate dependent mechanical behavior, and then link changes in this behavior to variations in the alloy's microstructural evolution. This study was performed in conjunction with a high strain-rate study of the same materials, conducted by Kannan et al. using a Kolsky bar apparatus. Thus, we tested samples in compression to achieve congruency between the two sets of mechanical studies, and we examined microstructure evolution in the deformed AZ31B samples, in detail, using Electron Backscatter Diffraction (EBSD).

3.2 Experimental Methods

AZ31B, was selected for the study, and obtained in the warm-rolled H24 condition from Magnesium Elektron. The as-received material possessed a rolling texture in which the basal poles are nearly perpendicular to the plate normal, and an area average grain size of roughly 71.5 ± 42.9 μm. Some of the as-received AZ31B was processed by the $4B_C$ route using the same conditions as in the previous section. Pole figures of the

initial, warm-rolled plate and the resulting ECAE processed material are shown in figure 3.1. The resulting material had an area average grain size of 5.3 μm ± 2.5 μm.

Rectangular compression test samples with a nominal size of 2 mm × 2 mm × 4 mm were machined from both the as-rolled material and the ECAE processed material using an Electrical Discharge Machine (Fanuc Alpha 0iE, Oshino-mure, Yamanashi Prefecture, Japan). Rectangular samples were used in place of cylindrical ones to allow for more direct comparison to the results of the high strain-rate Kolsky-bar tests and to preserve the off-axis orientations. Two orientations were prepared from the as-received and ECAE processed materials as shown in figure 3.2b. In the as-rolled AZ31B, samples were machined with the long axis parallel to the rolling and normal directions of the plate; while in the ECAE processed AZ31B, the samples were cut with the long axis along the transverse and extrusion directions. According to the orientation of their long axis, the samples are named “Rolled R”, “Rolled N”, “ECAE T”, and “ECAE E”.

Compression tests were performed at strain-rates from 10^{-4} to 10^{0} s^{-1} in equal logarithmic increments in a Universal Testing Machine (Instron 5582). A thin layer of molybdenum disulfide was applied as lubricant on the upper and lower platens. Crosshead displacement was used to measure strain, and machine compliance was determined by pressing the lubricated platens together in the manner described by Kalidindi et al [83]. In addition to the standard compression tests, interrupted compression tests were performed on each sample orientation, to an approximate true strain of 2.5%, 5%, and, if possible, 10% at a strain rate of 10^{-4} s^{-1}. Each of the ECAE processed orientations were deformed to an approximate true strain of 2% at 10^{0} s^{-1}, as

well, but in these tests, a collar was necessary to limit the applied strain. 0.2% offset was used to determine the onset of yield.

The interrupted compression test specimens were initially mechanically polished at 1200 grit and then at 50 nm with the Struers (Westlake, OH) OPS non-dry suspension. Specimens were then milled in a Gatan PIPS 2 ion mill (Pleasanton, CA) at 5 kV for 5 minutes, 3 kV for 15 minutes, 1 kV for 20 minutes, and at 0.5 kV for 20 minutes. A gun tilt of 3° was used and the samples were chilled to -100°C. The compression test samples were then characterized by EBSD in a TESCAN MIRA3 GMU FEG-SEM (Libušina, Czech Republic). EDAX TEAM software (Mahwah, NJ) was used to collected the EBSD data at a step size of 0.4 μm. EBSD data was analyzed using the same methods as in Chapter 2. Due to the possibility of there being a considerable amount of deformation in the microstructure, the K1 twin plane was allowed to vary by up to 3°, and the misorientation by up to 7° when determining the presence of twins.

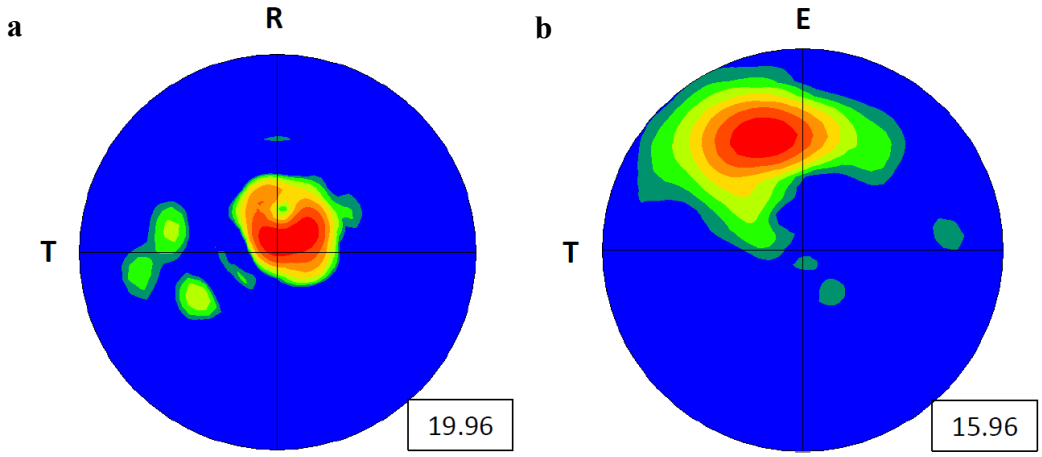

Figure 3.1: {**0002**} pole figures of (a) as-rolled and (b) AZ31B processed by the $4B_C$ route.

3.3 Results and Discussion

3.3.1 Compression Tests

Typical stress-strain curves for each of the strain-rates and orientations are shown below in Figure 3.3, with at least three tests performed for each strain rate and orientation. Rolled N samples display a typical hardening curve for $\langle c \rangle$ axis compression, and only a modest increase in ultimate compressive strength with increasing strain. The 10^0 s^{-1} strain rate samples show smaller strain hardening rates at low strains, but also do not level off as much. The Rolled R samples show no change in yield stress with strain rate, but do exhibit greater strain hardening

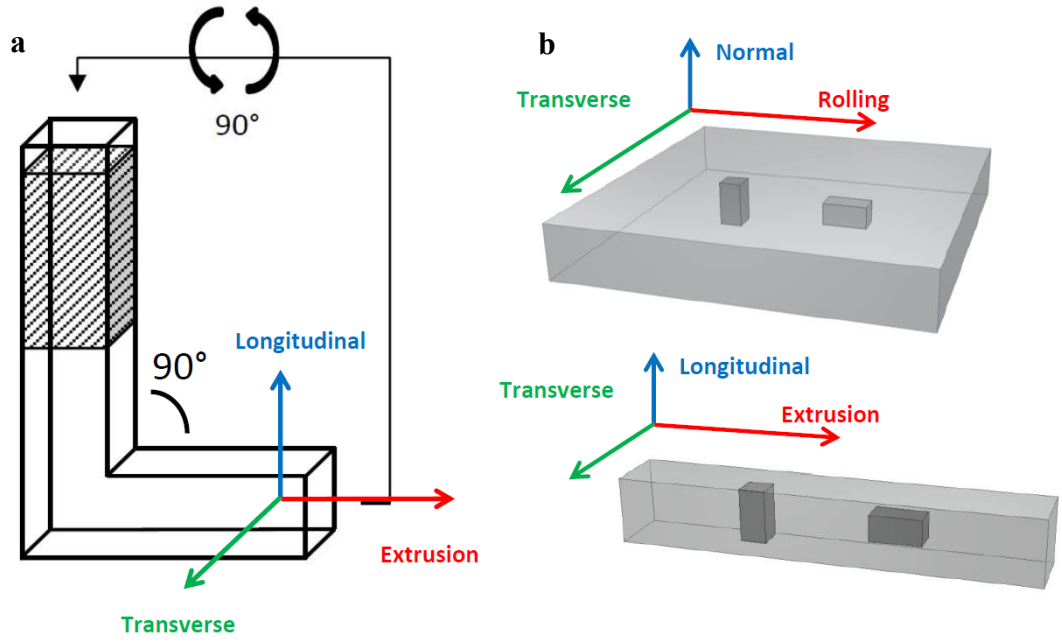

Figure 3.2: (a) Schematic of the ECAE process, including the rotation between passes for the $4B_C$ route. (b) Orientations of the compression test samples cut from the rolled plate and the ECAE billet, respectively. The samples were compressed along their long axis.

rates following the plateau and a reduction in ductility. At all strain rates for the Rolled N and, after the lower hardening plateau, the Rolled R orientations, the rate of strain

hardening is greater than the rate of strain hardening found for the ECAE sample orientations.

Both ECAE orientations display more moderate sigmoidal curves than those shown in the Rolled R samples, and the differences between the two sets of ECAE stress-strain curves are less pronounced than seen between the two sets of rolled samples. Both sets of ECAE samples tend to attain a peak flow stress at approximately 15% strain, and they fail with a gradual or sharp load drop. However, the ultimate compressive stresses measured for the ECAE T samples are generally higher than those found for the ECAE E samples. Both ECAE orientations, aside from the 10^0 rates, display very little strain-rate sensitivity. Note that for each orientation, the samples tested at 10^0 s^{-1} appear to experience less initial strain hardening than the other rates, but achieve parity at about 5% strain. The differences between the highest and lowest strain rates for all the orientations are accentuated in the combined plot in figure 3.4, showing clear drops in yields strength of both ECAE samples at the highest strain rate.

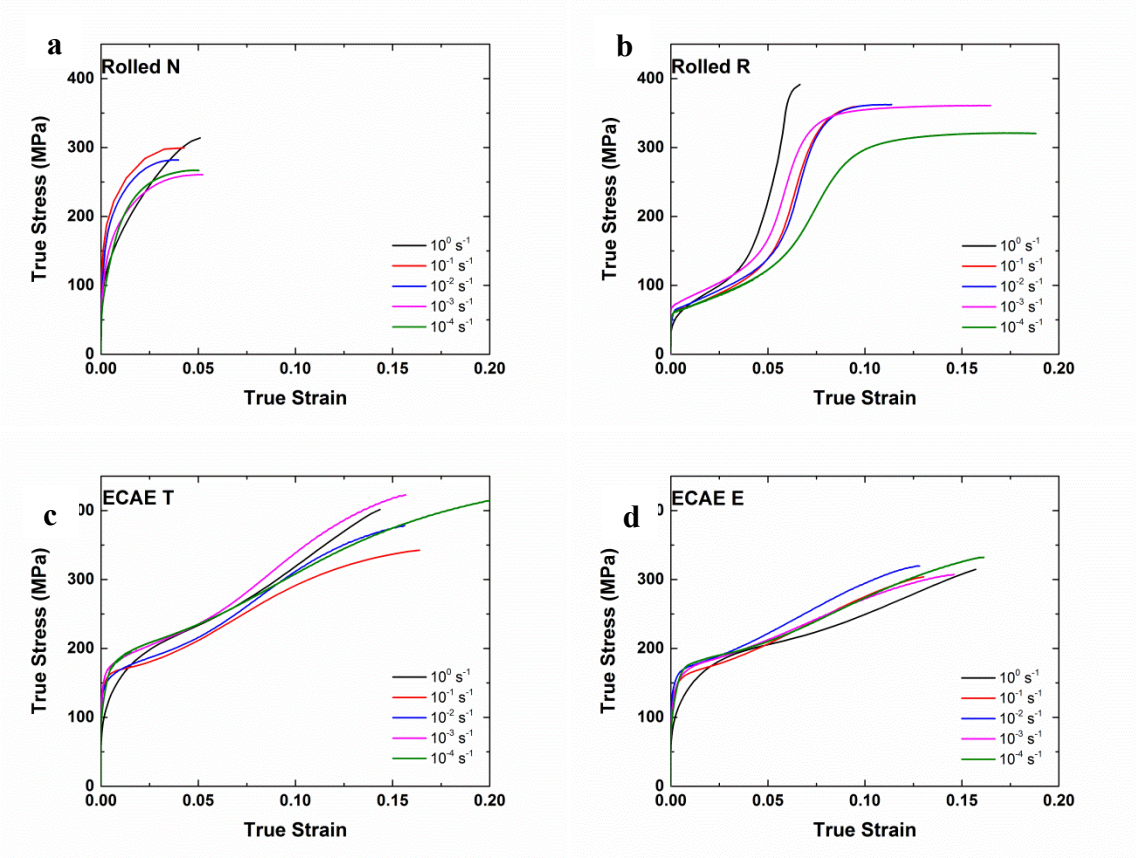

Figure 3.3: True stress-true strain curves cut off at the peak flow stress attained; (a) Rolled N, (b) Rolled R, (c) ECAE T, and (d) ECAE E. For ECAE T 10^{-4} s^{-1}, the line extends just beyond the right border of the graph. Note the differences in the shape of the curves.

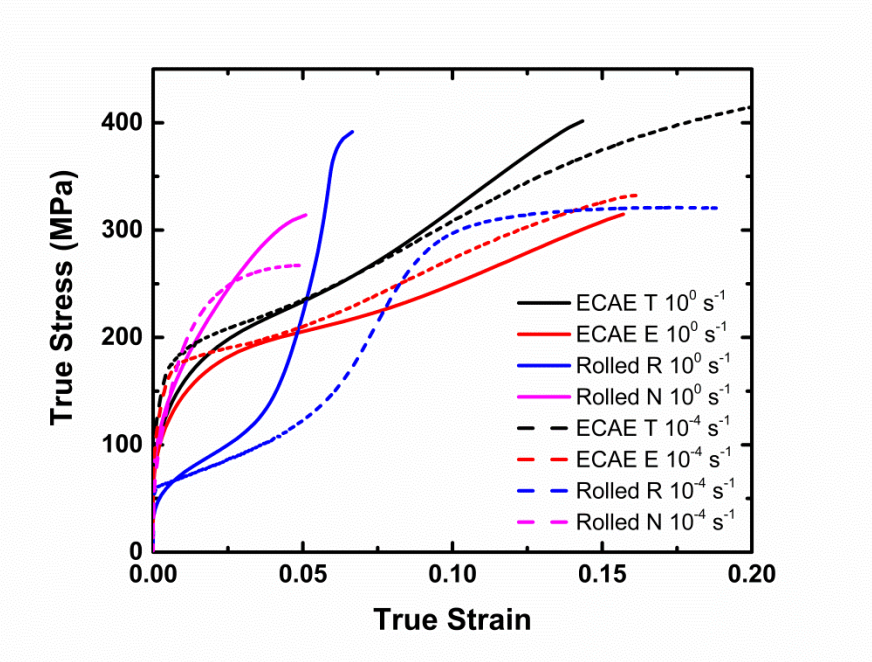

Figure 3.4: Combined stress-strain plots for the various orientations from each of the sample types at the fastest (10^0 s^{-1}) and slowest (10^{-4} s^{-1}) strain rates. For ECAE T 10^{-4} s^{-1}, the line extends just beyond the right border of the graph.

3.3.2 Compressed Sample Microstructure

Inverse pole figures and pole figures for rolled N samples compressed to 2.5 and 5% true strain are shown in Figure 3.5. Rolled N samples fail before a plastic strain of 10% is attained, and thus are not included here. High angle boundaries – boundaries with a misorientation greater than 15° - are shown in black. A large reduction in area average grain size from approximately 71.5 ± 42.9 μm to 37.7 ± 11.5 μm is seen in the rolled N sample compressed to 2.5%, whereas the decrease from 2.5% to 5% was a more modest reduction to 31.6 ± 13.8 μm. The large reduction in average grain size is attributed to extensive grain fragmentation and subsequent dynamic recrystallization at grain boundaries, which is observed in both figures 3.5a and 3.5b. The majority of the lenticular twins in both the 2.5% and 5% microstructures are the $\{10\bar{1}2\}$ extension type,

most likely remaining from the parent microstructure. In comparison, very few contraction twins were observed. The measured texture was found to change very little from 0% to 5% strain.

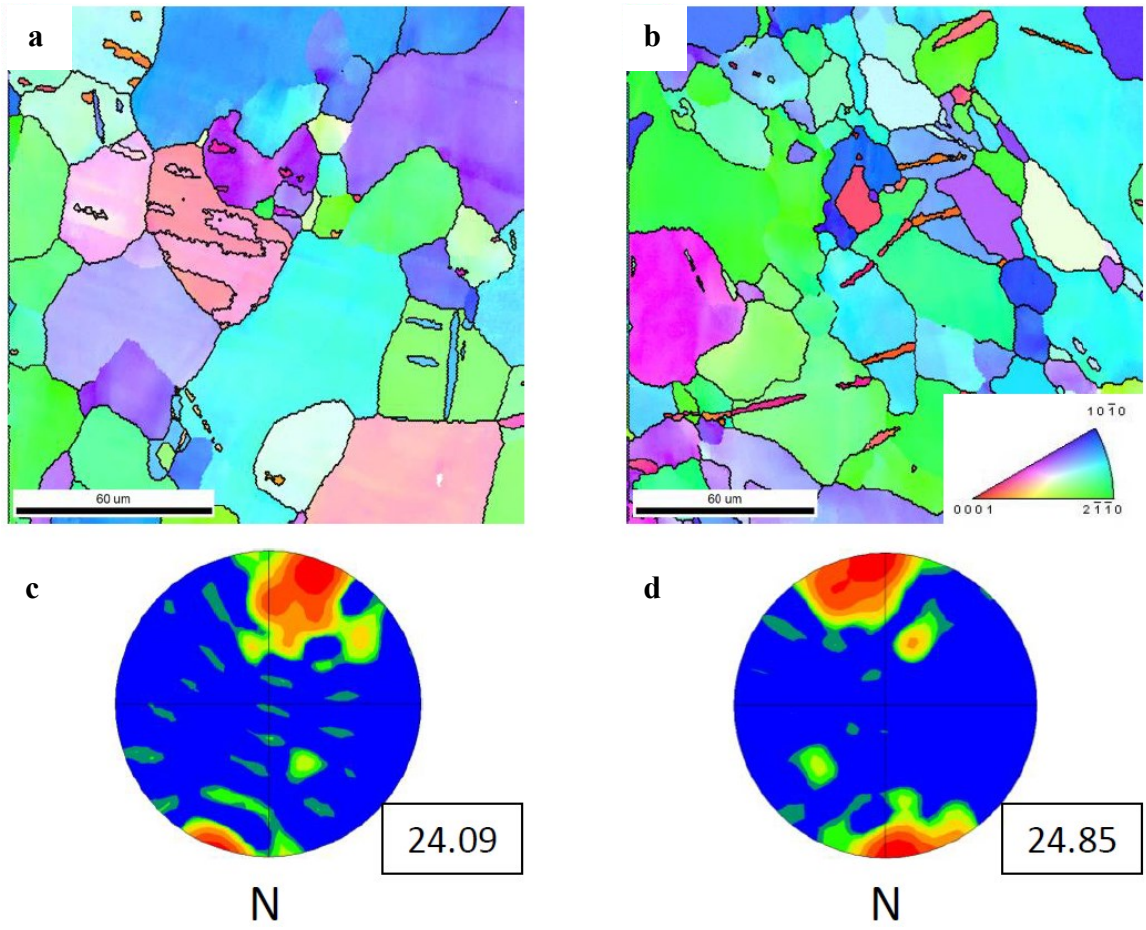

Figure 3.5: (a) IPF of Rolled N sample compressed to 2.5% true strain; (b) IPF of Rolled N sample compressed to 5% true strain; (c) (0001) Pole figure of Rolled N sample compressed to 2.5% strain; and (d) (0001) Pole figure of Rolled N sample compressed to 5% strain. Compression axis is vertical and the strain rate for both tests is 10^{-4} s^{-1}. The number in the box next to each pole figure is the maximum strength of the texture.

In contrast to compression of rolled samples along the normal direction, extensive twinning is observed following compression of these samples along the rolling direction,

as seen in figure 3.6. Multiple variants of the $\{10\bar{1}2\}$ extension twin type are contained in the microstructures, but $\{10\bar{1}1\}$ contraction twins are also occasionally seen. Approximately 25% of the area fraction in the Rolled R sample that was strained to 2.5% (figure 3.6a) is twinned. While still heavily twinned, the microstructure of the Rolled R sample strained to 5.0% (figure 3.6b) possesses a prominent grain almost devoid of twins. In addition, the pole figure for this sample (figure 3.6d) shows that the basal poles have shifted from an orientation almost perpendicular to the compression axis, to one that is nearly parallel to it. These results suggest that twin variants in the 2.5% strain sample have preferentially grown and now dominate the microstructure in the 5% strain samples. In addition, a number of the thin lenticular features in figure 3.6B were probed and were found to have basal poles aligned horizontally, matching the primary texture of the 2.5% strain sample.

The microstructural evolution exhibited by the ECAE material is drastically different from that of either of the two rolled sample orientations. Part of this difference can be attributed to the fact that the ECAE process refines the grain size and reorients the texture of the as-rolled material. Through the $4B_C$ ECAE processing route, the basal pole is tilted away from both the extrusion and transverse axes, allowing for higher resolved shear stresses on basal planes during compression along the E and T directions. Figures 3.7a-d show apparent grain growth and texture evolution with increasing strain for compression along the transverse direction. After 2.5% true strain, the texture has weakened, with the misorientation distribution shifting towards values greater than 30°. However, there is not yet a change in the average grain size, as shown in figure 3.8. Following 5.0% true strain, though, an increase in grain size is apparent in the

IPF, and the 30° peak, a result of dynamic recrystallization in Mg, has disappeared completely [64–66]. The texture at 5% is not significantly weaker, but the orientation of the as-processed ECAE texture has been lost. Grain growth continues up through

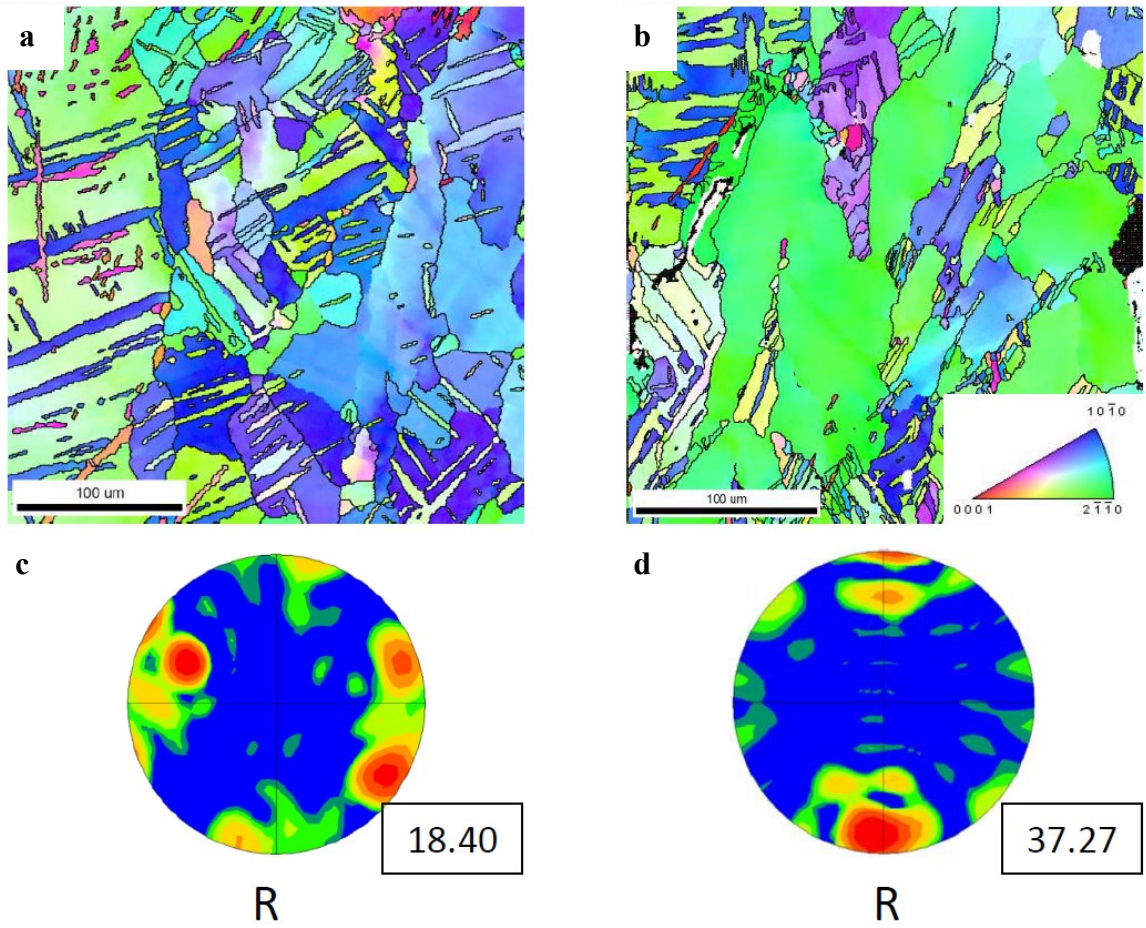

Figure 3.6: (a) IPF of Rolled R sample compressed to 2.5% true strain; (b) IPF of Rolled R sample compressed to 5% true strain; (c) (0001) Pole figure of Rolled R sample compressed to 2.5% strain; and, (d) (0001) Pole figure of Rolled R sample compressed to 5% strain. Compression axis is vertical and the strain rate for both tests is 10^{-4} s^{-1}. The number in the box next to each pole figure is the maximum strength of the texture.

10% true strain, but a number of the grains possess distinctly nonequilibrium shapes. Additionally, some of the larger grains also display subdivision by intermediate angle boundaries. In the misorientation angle distribution, the 30° peak has reappeared. The texture has sharpened and it has achieved an orientation and strength similar to that of the

initial ECAE texture. These results collectively suggest that by 10% strain, the microstructure has achieved a large enough grain size for DRX to restart.

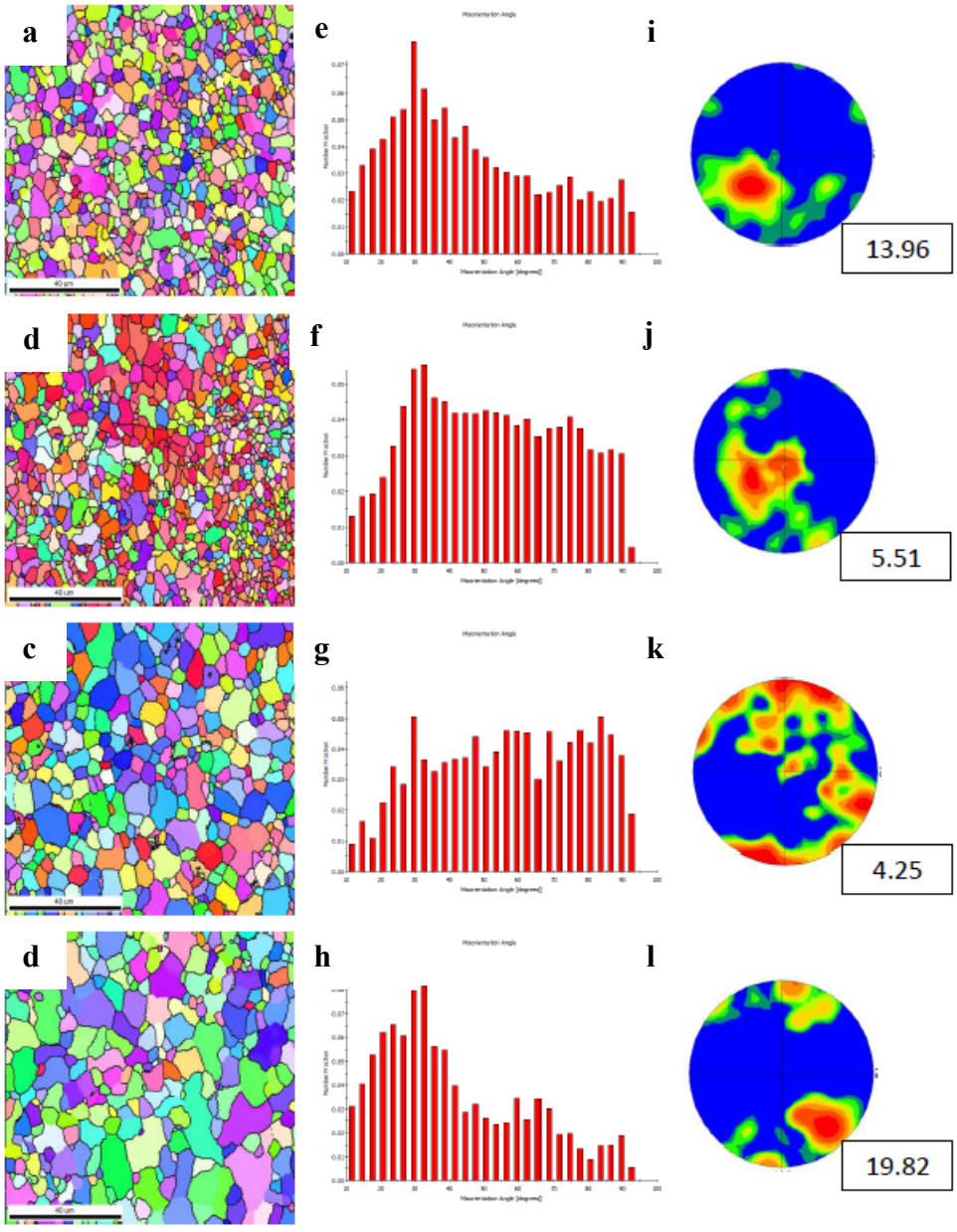

Figure 3.7: (a-d) IPFs of ECAE T sample compressed to 0%, 2.5%, 5%, and 10% true strain, respectively; (e-h) Misorientation angle distributions of ECAE T samples compressed to 0%, 2.5%, 5%, and 10% true strain, respectively; and (i-l) (0001) Poles figure of ECAE T samples compressed to 0%, 2.5%, 5%, and 10% true strain, respectively. The compression axis is vertical and the strain rate is 10^{-4} s^{-1}. The number in the box next to each pole figure is the maximum strength of the texture.

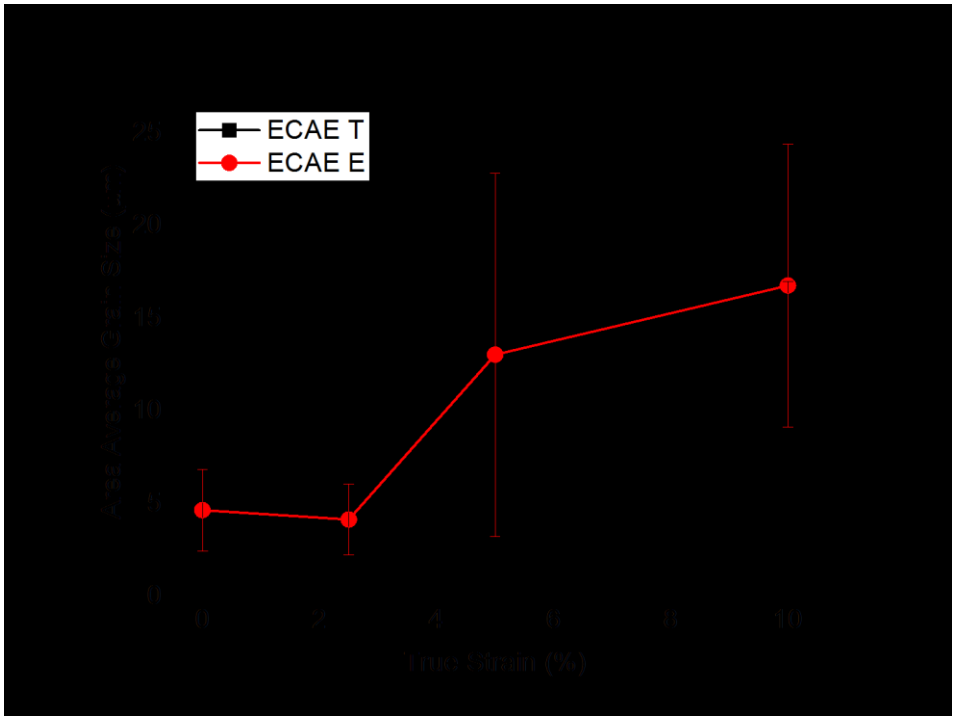

Figure 3.8: Area average grain size as a function of strain for the ECAE samples compressed along the T and E directions, respectively; the strain rate for these tests was 10^{-4} s^{-1}.

The grain growth displayed by the ECAE material compressed along the extrusion (E) axis in figure 3.9 is pointedly different from that of the ECAE samples compressed along the T direction. For both loading orientations, there is no apparent grain growth at 2.5% strain, but after 5% and 10% strain, the average grain size for E compression samples is larger than that of the T compression samples, at the same strains. The increase in the standard deviations observed in Figure 8 after 5% is not reflective of an increase in uncertainty in the grain size. Instead, they are indicative of a redistribution of grains sizes due to abnormal grain growth. To a significant extent, the original grain size distribution still exists, but it is convoluted with a smaller number of much larger grains that have grown abnormally. Additionally, the EBSD images in figures 3.9c and 3.10b suggests that the grain growth is more nonuniform in the E

compression samples than in the T compression samples. In terms of texture, there is little weakening or change in the as-extruded texture up through 2.5% strain, for both orientations. However, the crystallographic texture of the ECAE T samples begin to change at 5% strain (figures 3,7i-l), while there is no significant change in the texture until 10% strain for the ECAE E samples (figures 3.8i-l). This delay can also be seen in the misorientation angle distributions, which remain largely static until 10% strain for loading in the ECAE extrusion direction. It should also be noted that twins are rarely observed in either ECAE orientations.

ECAE T and E samples were also compressed to approximately 2% true strain at rates of 10^0 s^{-1} to investigate the cause of the sudden drop in yield stress associated with the highest strain rate. As in the samples compressed at the lowest strain rate of 10^{-4} s^{-1}, the ECAE T samples compressed at 10^0 s^{-1} exhibit grain growth and possibly minor amounts of recrystallization. These samples also show a weakening of the texture in figure 3.7c. However, the dynamic grain growth at a strain rate of 10^0 s^{-1} occurs at a smaller strain (2%) compared to the tests conducted at 10^{-4} s^{-1}, where grain growth does not show until 5% strain. The area average grain size has grown to 13.46 μm ± 6.72 μm after straining to 2% strain at a rate of 10^0 s^{-1}, while grain size remains relatively constant at 4.96 μm ± 2.08 μm, after straining to 2.5% at the much slower rate of 10^{-4} s^{-1}. Dynamic grain growth also occurs in the ECAE E sample, but the phenomena is more heterogeneous and, overall, appears to occur relatively infrequently in the microstructure. In fact, the heterogeneous grain growth observed in figure 3.10b is similar to the heterogeneity that is seen for dynamic abnormal grain growth. The larger than average grains in figure 3.10b also display an increased propensity to twin. In addition, the large

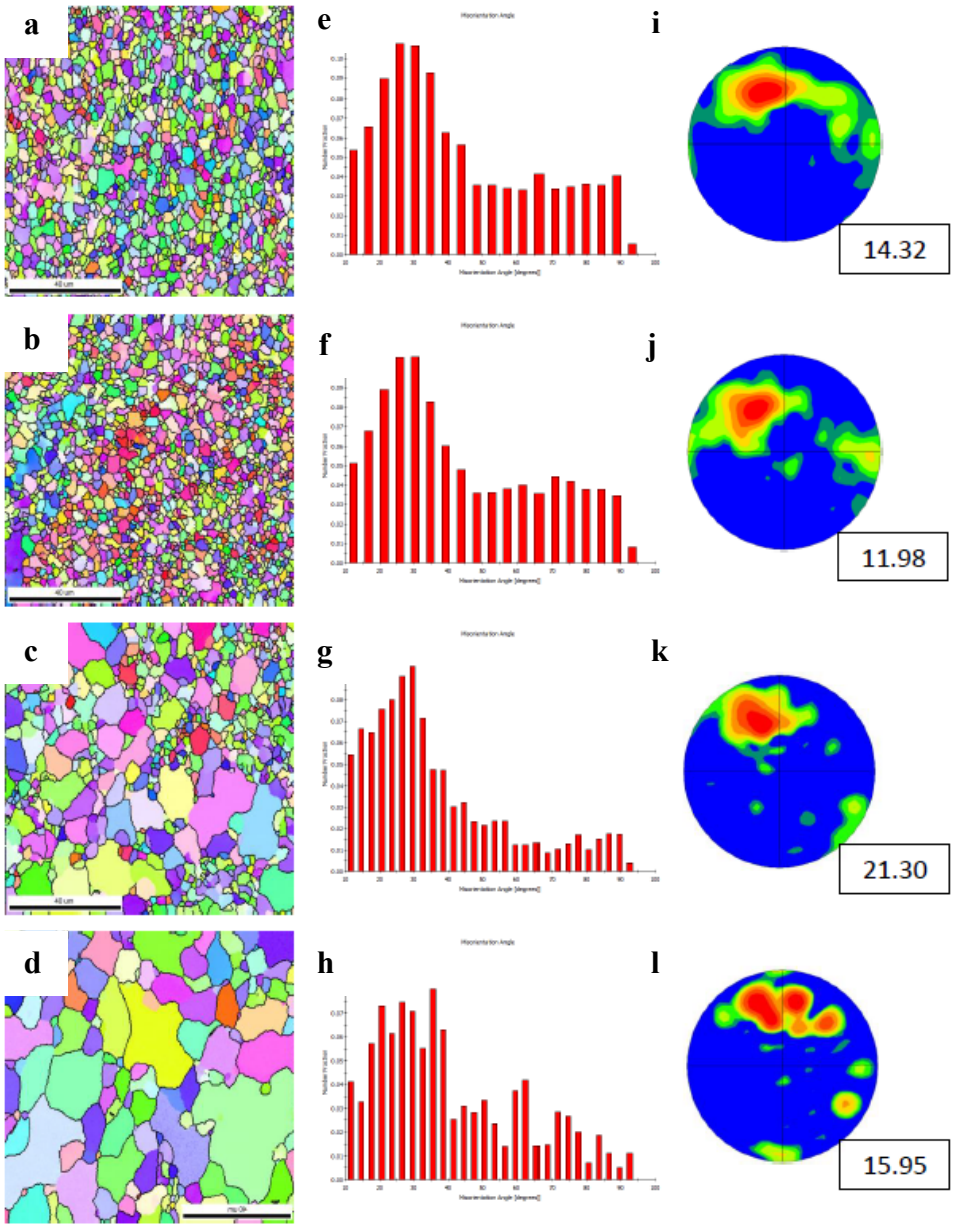

Figure 3.9: (a-d) IPFs of ECAE E samples compressed to 0%, 2.5%, 5%, and 10% true strain, respectively; (e-h) Misorientation angle distributions of ECAE E samples compressed to 0%, 2.5%, 5%, and 10% true strain, respectively; and, (i-l) (0001) Poles figure of ECAE E samples compressed to 0%, 2.5%, 5%, and 10% true strain, respectively. The compression axis is vertical and the strain rate is 10^{-4} s^{-1}. The number in the box next to each pole figure is the maximum strength of the texture.

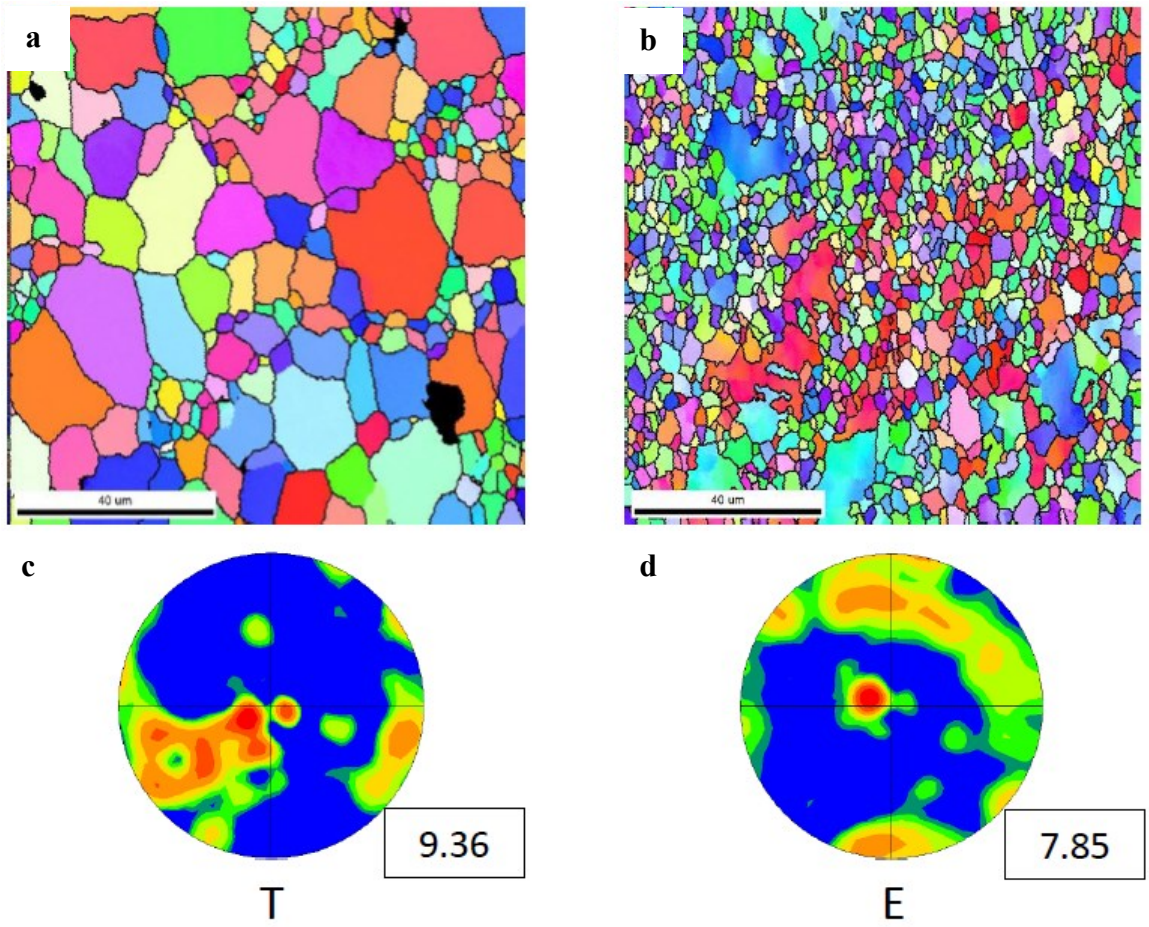

Figure 3.10: IPF of (a) an ECAE T sample and (b) an ECAE E sample, both compressed to 2% strain at strain rate of 10^0 s^{-1}. (0001) Pole figures of (c) an ECAE T sample and (d) an ECAE E sample compressed to 2% strain at a strain rate of 10^0 s^{-1}. The compression axis is vertical. The number in the box next to each pole figure is the maximum strength of the texture.

grains, approximately 18-23 μm in diameter, frequently possess a corrugated grain boundary indicating that these grains are of sufficient size for DRX to resume. The pole figure in 3.10d shows a local weakening of the texture for the ECAE E sample, and a comparatively strong twinning (link to text below)orientation. However, the majority of the microstructure retains a texture comparable to the initial, as-extruded texture, and similar to the texture of the ECAE E samples compressed at the slower 10^{-4} s^{-1} strain rate.

3.3.3 Microstructural Analysis of Compressed Samples

EBSD analysis of the Rolled N samples reveals very few contraction twins in the microstructure, implying that plasticity is entirely due to dislocation motion. The extension twins that are observed in the microstructure appear to have no impact on the overall mechanical response. In contrast, twinning plays a major role in the mechanical response of the Rolled R samples. This is because of the fact that in these samples, due to warm rolling, the basal poles are oriented such that they are unfavorable for slip mediated deformation. The considerable extension twinning observed in the early stages of deformation is eventually replaced in the microstructure by a single twin variant that possesses a twinned orientation, where the $\langle c \rangle$ axis is parallel to the compression axis. This observation agrees with those seen by Khan et al., who reported the replacement of the original rolling texture by a twinned texture [74]. The realignment of the lattice into a geometrically harder orientation is the apparent source of strain hardening in the Rolled R samples.

Unlike the Rolled R samples, the compressed microstructures of the ECAE samples contain very few twins. The misorientation angle distributions and the pole figures suggest that twinning is insignificant during loading. Thus, the shallow sigmoidal stress-strain curves in the ECAE processed samples cannot be attributed to twinning. Instead, the microstructural evidence suggests the activation of a number of interacting and competing mechanisms. Taylor hardening is likely the primary source of hardening in these materials, with orientation hardening being a secondary source. Evidence of softening mechanisms in the form of grain growth and DRX are also present. Together, the mechanisms produce a complex mechanical response.

The most apparent aspect of the ECAE samples' microstructures is the distinct abnormal grain growth, which shows some similarities to stress-assisted grain growth. To the best of the authors' knowledge, stress-assisted grain growth has mainly been reported for nanocrystalline materials – including magnesium [84–88]. Cahn and Taylor have put forth a theory, later confirmed by simulations and experiments, that shear stresses on a grain boundary can produce normal motion of that grain boundary [89–91]. It can be inferred from this theory that stress-induced grain boundary migration can produce both grain growth and grain rotation [90]. Figure 3.7 appears to support this theory as it shows simultaneous grain growth and a substantial weakening in the texture of the microstructure in the intermediate stages. It is possible that texture softening provides some strengthening during grain growth. The initial texture of the material is well suited for basal slip; thus, a weakening of the texture is likely to reduce the overall activity of the basal slip system. An additional factor for consideration is that it is currently unknown how the sub-micrometer, Mn-rich precipitates that are typically found in wrought AZ31B are interacting with evolving microstructure [92].

A comparison to the grain growth in this study may be found in work by Gianola et al., who performed microtensile experiments on nanocrystalline Al thin films, and observed apparent stress-assisted grain growth [85]. Similar to the findings here, Gianola reported discontinuous grain growth and associated extended ductility [85]. However, the stress-strain curves of the AZ31B/ECAE samples studied here have a sigmoidal shape, while the curve of the nanocrystalline Al had a concave shape, typical of dislocation dominated deformation, before rapidly reaching a plateau [85]. The difference between the ultimate tensile strength and the yield strength in the nanocrystalline Al appeared to

be less than 50 MPa [85]. Gianola et al. attributed the rapid grain boundary motion to unpinning from solutes, but the greater homogeneity of grain growth and the differences in mechanical response suggest an alternate mechanism is active in AZ31B [85].

If stress-assisted grain growth is indeed active, an explanation of the drop in the yield stress at the 10^0 s^{-1} rate may be offered by examination of the EBSD samples tested at 10^0 s^{-1}. The grain growth in the 10^0 s^{-1} samples occurs much earlier than in the 10^{-4} s^{-1} samples, suggesting that increasing strain rate allows grain growth to occur at lower plastic strains. The relative rate of grain growth between ECAE E and ECAE T has also changed. Whereas the ECAE E sample possesses larger grains than the ECAE T sample by 10% strain at the lowest strain rate of 10^{-4} s^{-1}, the grains in the ECAE T sample are both larger and grain growth has occurred more frequently within the microstructure at the higher strain rate of 10^0 s^{-1} and the lower total strain of 2%. At the higher strain-rate, local stresses can accumulate more rapidly and achieve the magnitude necessary for the onset of stress-assisted grain growth. If the stress required to induce grain boundary motion is lower than that required for dislocation motion or twinning, then the material could be yielding due to the onset of grain growth instead of slip. Within this context, as the ECAE T orientation is plastically harder, as the strain-rate increases, the local stress accumulation must also be greater than in ECAE E. In fact, Gianola et al. reported lower yield stresses for thin films where stress-induced grain growth occurs, than in otherwise similar films [85]. In the context of this argument, it can then be suggested that the yield stress drops because the higher strain rate helps to drive stress-induced grain growth.

Given that stress-induced grain growth has typically been reported in nanocrystalline or ultrafine grained materials, it would seem to raise the questions of why

and how does this process occur in micrometer-sized grains. In truth, local migrations of high angle boundaries are common events in the microstructural evolution of magnesium, specifically during discontinuous dynamic recrystallization (dDRX). The dDRX process is dependent on the initial bulging of a high angle boundary, which is itself caused, at low temperatures, by the interaction of dislocations with the grain boundary [49,93]. It is at this point where it is proposed that the dDRX and potential stress-induced grain growth diverge. During dDRX, a low angle boundary develops across the bulge, stabilizing it and forming the nucleus of a recrystallized grain [93]. If, however, that low angle boundary did not form, a combination of local stresses and curvature may drive expansion of the bulge and, eventually, a net translation of that grain boundary. Whether the local stresses are relaxed by emission of dislocations from the grain boundary (forming a low angle boundary) or are a wholesale migration of the boundary may depend on the overall length of the boundary, and hence the grain size. As the grain size and length of the grain boundary increases, it is expected that dDRX becomes more likely than stress-assisted grain growth. This transition would account for the apparent renewal of DRX in the later stages of grain growth. This implies that at sufficiently high strains, the process of stress-assisted grain growth is counteracted by the resumption of DRX.

It is important to note that the different mechanisms appear to dominate at different stages of deformation and strain-rates. Taylor and orientation hardening appear to dominate the effects of grain growth at intermediate stages, while DRX dominates the later stages where the rate of strain hardening decreases. At higher strain rates, the onset of grain growth appears to occur earlier, as shown in figure 3.10. Ultimately, grain growth may occur early enough to compete with slip and produce the reduction in yield

stress observed in figure 3.11. Hypothetically, there are three mechanism regimes in these ECAE samples that depend on strain rate. At the low strain-rates (10^{-4} s^{-1}), slip appears to dominate the mechanical response. At intermediate rates (10^{0} s^{-1}), the onset of stress-assisted grain growth occurs and may dominate the mechanical response. At sufficiently high rates (10^{4} s^{-1}), not seen in this work, twinning is activated and appears to control the mechanical response.

3.3.4 Mechanical Analysis

Yield stress is shown as a function of strain rate in figure 3.11. Values for the ECAE samples remain relatively constant at approximately 150 MPa before dropping to values near 100 MPa at a strain rate of 10^{0} s^{-1}. In contrast, the rolled samples compressed along the normal direction display a yield stress of roughly 100 MPa at a strain rate of 10^{-4} s^{-1}, then rise to the levels of the ECAE samples with increasing strain rate, before also dropping at the highest rate of 10^{0} s^{-1}. Compressed along the rolling direction, though, samples have a yield stress near 50 MPa and show no change with strain rate. A significant drop in yield stress at a strain rate of 10^{0} s^{-1} is absent. Despite the larger initial grain size in the rolled samples, the Rolled N samples possess a yield strength close to that of the ECAE samples.

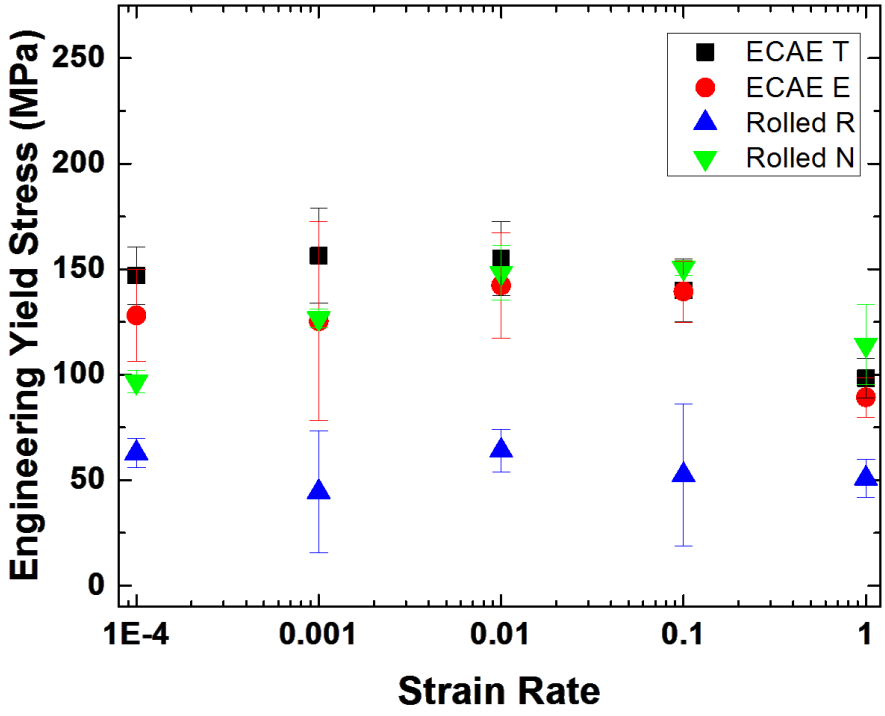

Figure 3.11: Yield stress plotted against strain rate for each orientation.

The true flow stress at different strain increments is shown for a strain rate of 10^{-4} s^{-1} in figure 3.12. The stresses at each increment are reflective of the trends already discussed. The Rolled R samples display the greatest increase in flow stress between 5 and 10% strain, achieving a flow stress comparable to that of ECAE T samples, despite the ECAE T specimens possessing a higher yield stress. However, the Rolled R samples never achieve the same degree of compression as the ECAE processed samples.

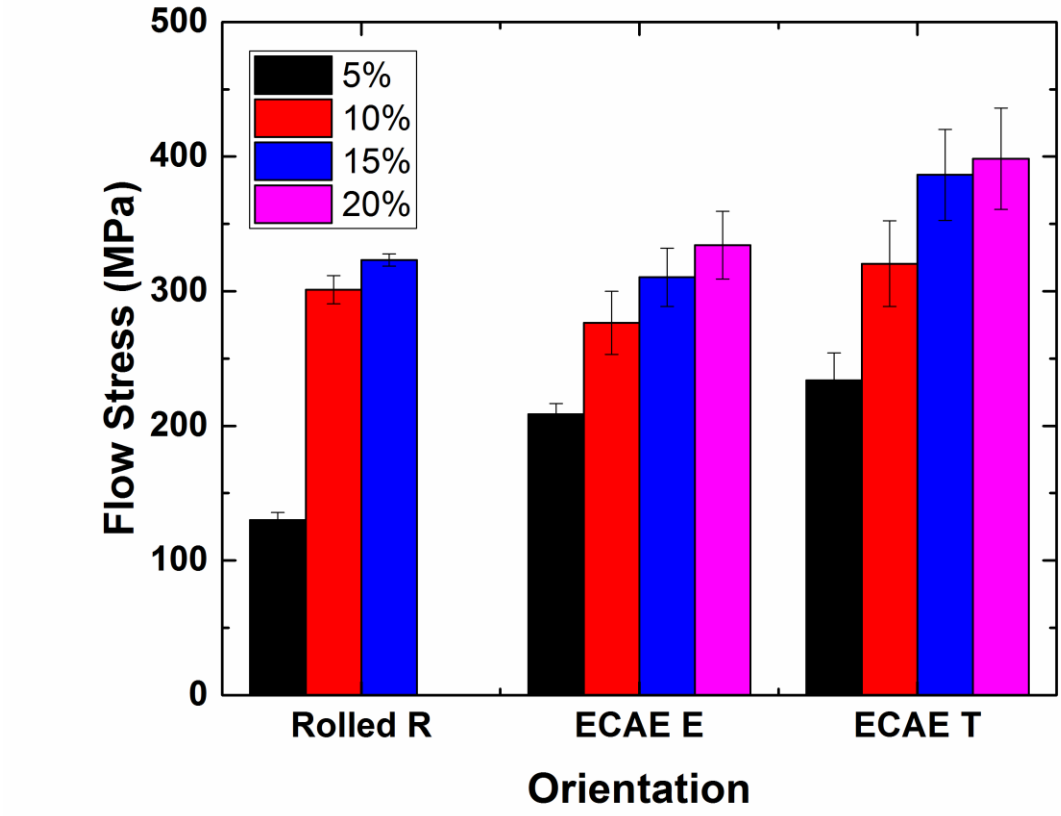

Figure 3.12: Flow stress at different strain increments for each orientation plotted for a strain rate of 10^{-4} s^{-1}. Rolled N samples were not included as they typically did not achieve greater than 5% strain. The lack of a bar indicates that all samples failed before reaching that strain increment.

The mechanical results shown here are in strong agreement with the literature. Al-Maharbi et al. reported similar strengths and ductilities for ECAE processed AZ31B, including the slight increase in strength in the transverse direction compared to the extrusion direction [78]. The results for the rolled AZ31B samples also show agreement with those found by Tucker et al. who observed an increase in strain hardening rates at higher strain rates, and a loss in ductility when compressing in the rolling direction [82]. However, the lower yield stress and the initial hardening rate displayed by all samples

compressed at 10^0 s^{-1}, except those compressed along the rolling direction, has not been reported elsewhere.

3.4 Conclusions

Samples of warm rolled and ECAE processed AZ31B were mechanically tested under compression at rates from 10^{-4} s^{-1} to 10^0 s^{-1} in multiple orientations. Both rolled and ECAE processed AZ31B were found to strain harden, at all strain rates, but the hardening rates were highest for the rolled materials, and in the case of the Rolled R samples, this hardening rate is attributed to the substantial activation of extension twinning. In contrast, no twinning is observed in the ECAE processed samples. The rolled material also showed a greater dependence of strain-rate hardening on strain rate than the ECAE material. However, the rolled samples tested in the rolling direction and both sets of ECAE processed samples – excluding the 10^0 s^{-1} rate – show no change in yield stress with strain rate. In contrast, the yield stress of the rolled samples tested in the normal direction does increase with strain rate before dropping again at 10^0 s^{-1}. All samples, except the Rolling N samples, which already had very limited ductility, exhibit a reduction in ductility with increasing strain rate. Investigation of the deformed microstructures showed that the ECAE materials underwent abnormal grain growth that increases with plastic strain and strain rate.

3.5 Appendix: ECAE Grain Size Distributions

Figure 3.13 shows the change in the grain size distribution of ECAE T and ECAE E after deforming to 0%, 2.5%, 5%, and 10% plastic strains at a strain rate of 10^{-4} s^{-1}.

Figure 3.14 shows the grain size distributions for ECAE T and ECAE E strained to 0% and 2% at a strain rate of 10^0 s^{-1}. Both figures show changes in the grain size distribution from the initial microstructure. The violation of statistical self-similarity during grain growth indicates that abnormal grain growth is occurring during mechanical testing in this experiment [94,95].

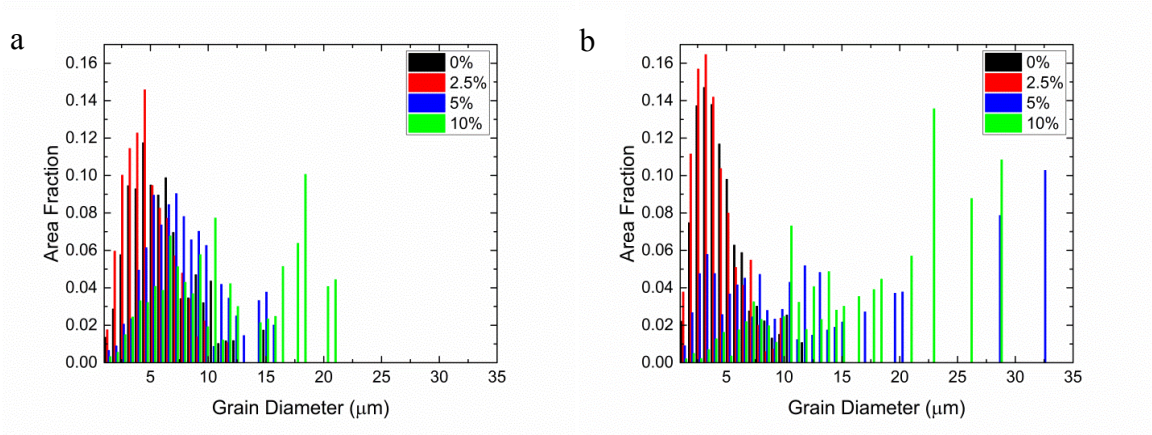

Figure 3.13: Grain size distribution plots of (a) ECAE T and (b) ECAE E samples deformed to different levels of strain at a strain rate of 10^{-4} s^{-1}.

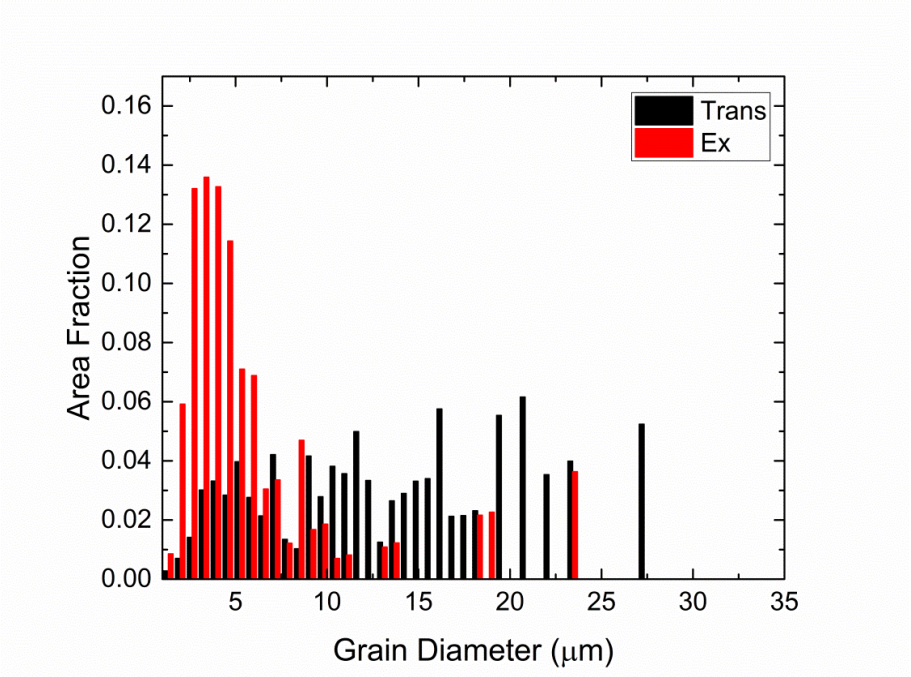

Figure 3.14: Grain size distribution plots of ECAE T and ECAE E loaded to 0% and approximately 2% strain at rate of 10^0 s^{-1}.

3.6 Appendix: Compiled Stress-Strain Diagrams

Stress strain plots for Rolled N, Rolled R, ECAE T, and ECAE E are shown in figure 3.15 for the full range of strain rates.

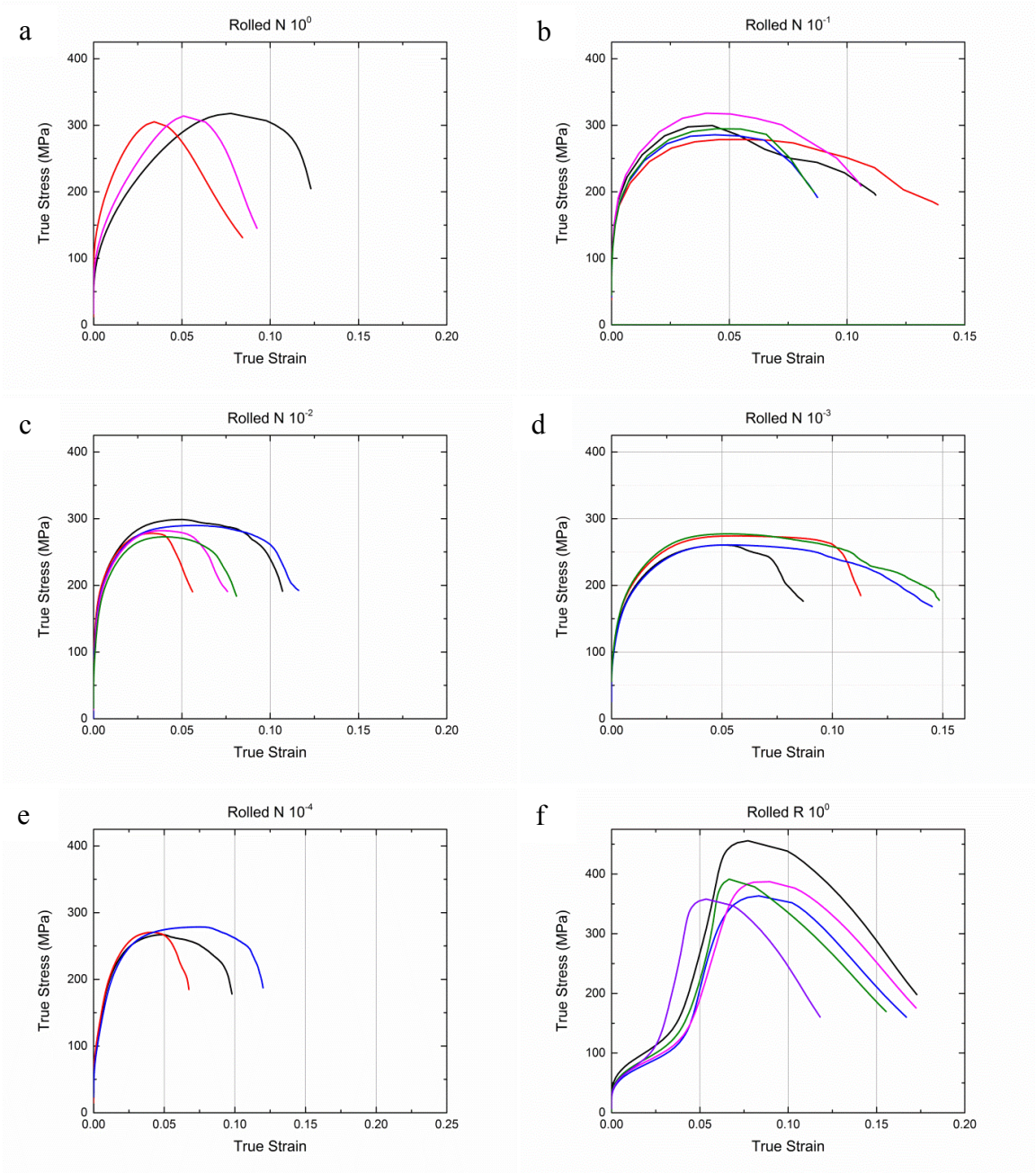

g

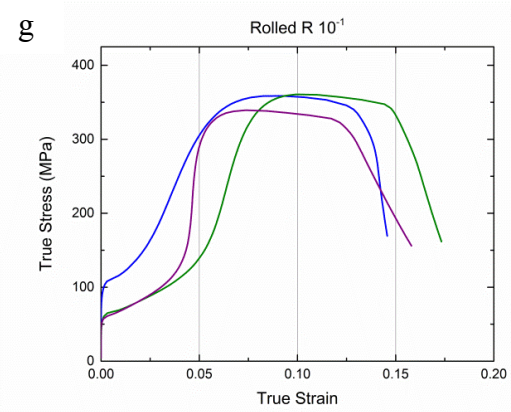
Rolled R 10-1
True Stress (MPa)
True Strain
0
100
200
300
400
0.00
0.05
0.10
0.15
0.20

h

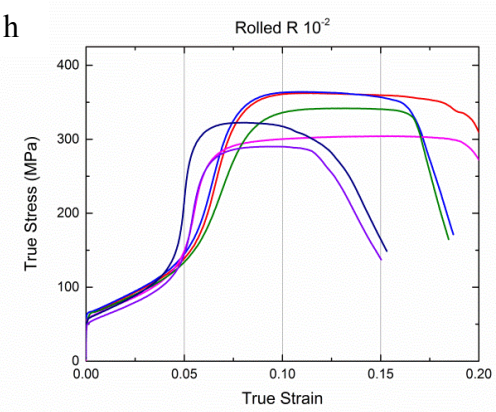
Rolled R 10-2
True Stress (MPa)
True Strain
0
100
200
300
400
0.00
0.05
0.10
0.15
0.20

i

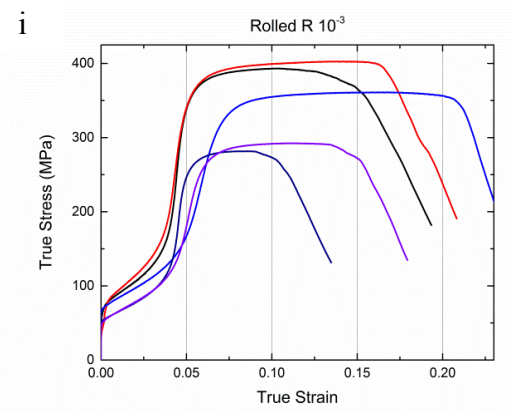
Rolled R 10-3
True Stress (MPa)
True Strain
0
100
200
300
400
0.00
0.05
0.10
0.15
0.20

j

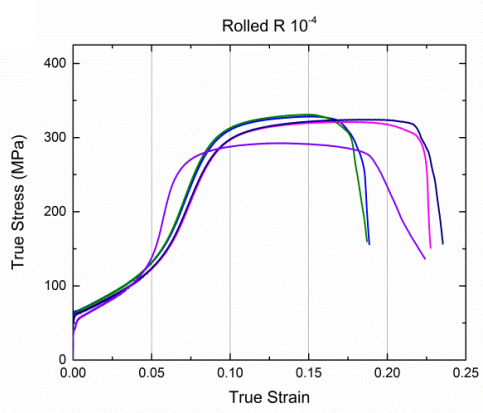
Rolled R 10-4
True Stress (MPa)
True Strain
0
100
200
300
400
0.00
0.05
0.10
0.15
0.20
0.25

k

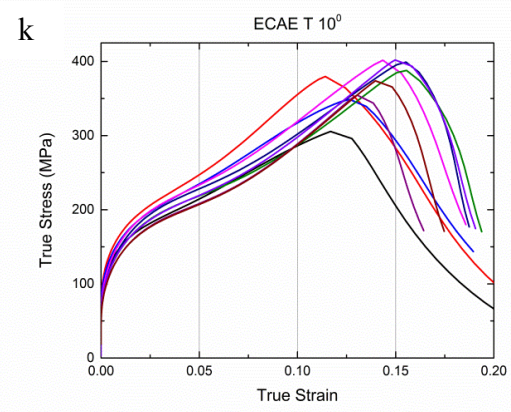
ECAE T 100
True Stress (MPa)
True Strain
0
100
200
300
400
0.00
0.05
0.10
0.15
0.20

l

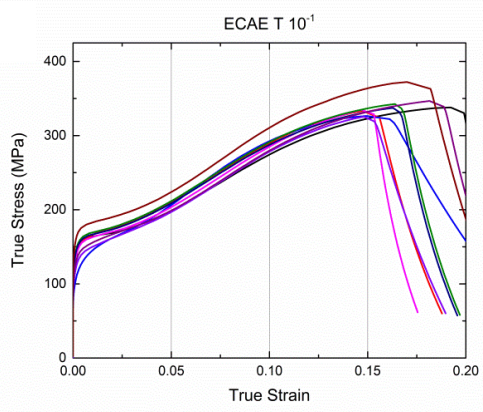
ECAE T 10-1
True Stress (MPa)
True Strain
0
100
200
300
400
0.00
0.05
0.10
0.15
0.20

m

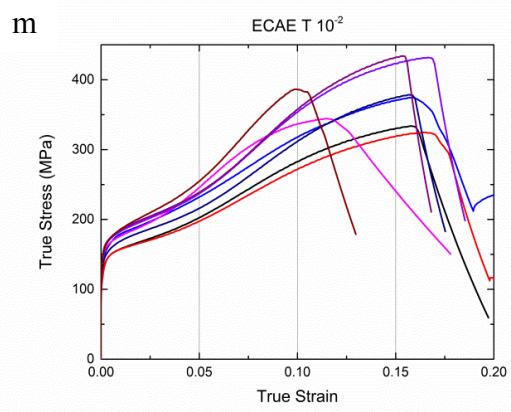
ECAE T 10-2
True Stress (MPa)
True Strain
0
100
200
300
400
0.00
0.05
0.10
0.15
0.20

n

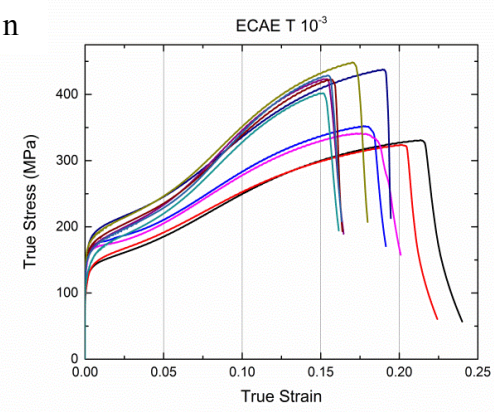
ECAE T 10-3
True Stress (MPa)
True Strain
0
100
200
300
400
0.00
0.05
0.10
0.15
0.20
0.25

o

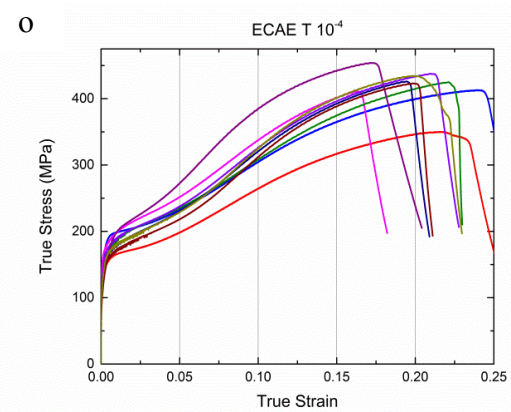
ECAE T 10-4
True Stress (MPa)
True Strain
0
100
200
300
400
0.00
0.05
0.10
0.15
0.20
0.25

p

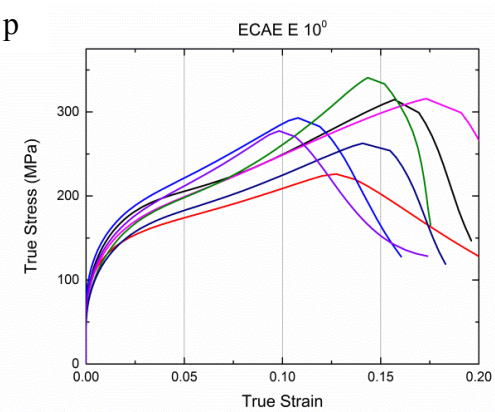
ECAE E 10^0
True Stress (MPa)
True Strain
0
100
200
300
0.00
0.05
0.10
0.15
0.20

q

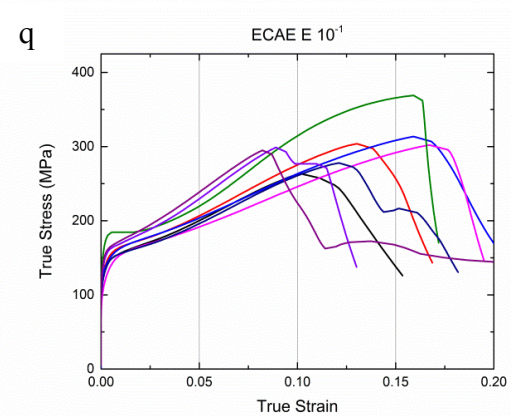
ECAE E 10-1
True Stress (MPa)
True Strain
0
100
200
300
400
0.00
0.05
0.10
0.15
0.20

r

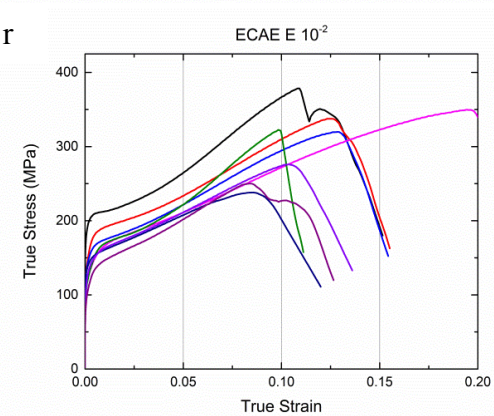
ECAE E 10-2
True Stress (MPa)
True Strain
0
100
200
300
400
0.00
0.05
0.10
0.15
0.20

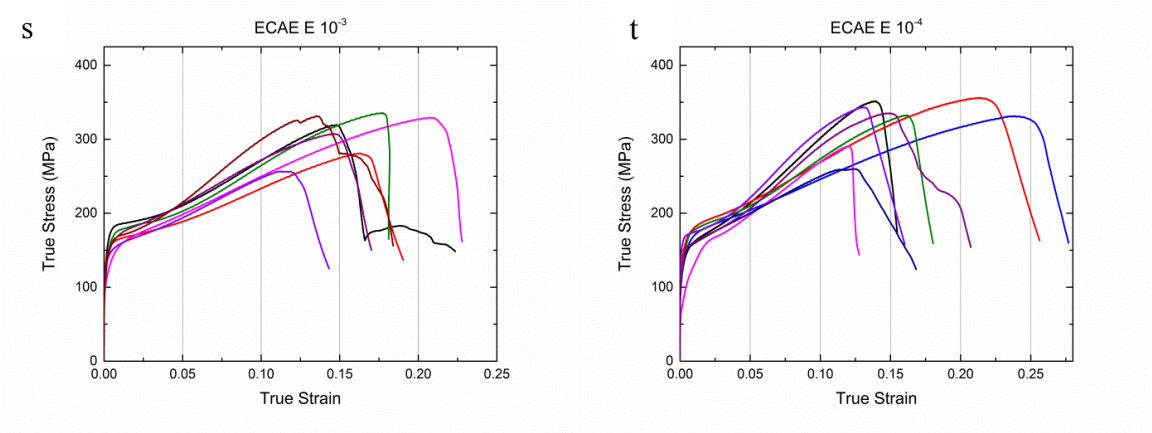

Figure 3.14: True stress-true strain plots for (a-e) Rolled N from 10^{0} s^{-1} to 10^{-4} s^{-1}, (f-j) Rolled R from 10^{0} s^{-1} to 10^{-4} s^{-1}, (k-o) ECAE T from 10^{0} s^{-1} to 10^{-4} s^{-1}, and (p-t) ECAE E from 10^{0} s^{-1} to 10^{-4} s^{-1}.

4. Characterization of Spalled AZ31B Processed by ECAE

4.1 Introduction

A considerable number of studies have investigated the mechanical properties of magnesium (Mg) and its alloys. However, the majority of these studies focus on the mechanical properties at quasi-static rates. There have been comparatively few studies of Mg alloys under shock conditions, where the failure behavior may be considerably different. Spall failure is one of the primary mechanisms for failure of Mg alloys at high rates, and understanding spall behavior is a necessary component to improving high strain-rate mechanical properties in Mg. Failure by spallation – either by void growth or fracture – occurs where tensile release waves of sufficient amplitude collide, and the local tensile stresses exceed a critical value [39]. A schematic of shock and spallation was provided in Chapter 1 as figure 1.4.

In this study, AZ31B samples processed via the $4B_C$ ECAE route were subjected to shock loading to investigate how sample orientation impacts their spall behavior. It is already known that large precipitates play a key role in the spallation of AZ31B, but it is currently unclear how they interact with the microstructure [45]. To achieve this objective, more detailed fractography was performed, and the area around nearby voids was inspected via (EBSD).

4.2 Experimental Methods

Samples of AZ31B were processed in the manner outlined in Chapter 2. Following ECAE processing, ECAE processed samples of AZ31B were cut into disks measuring nominally 18 mm in diameter and 6 mm in thickness via Electro Discharge

Machining (EDM) with the disk normal directions parallel to the Extrusion (Ex) and Transverse (Trans) directions. Shock recovery experiments were performed on these samples at the Shock Physics Laboratory, U.S. Army Research Laboratory (ARL, Aberdeen Proving Ground, MD) with a single stage 102 mm (slotted bore) diameter gas gun. The experiments used flyers with a nominal diameter of 42 mm and thickness of 2 mm, and impact velocities of approximately 200 and 400 m/s. In total, four samples were tested: 191 m/s along the extrusion direction, 414 m/s along the extrusion direction, 213 m/s along the transverse direction, and 394 m/s along the transverse direction. These samples have corresponding shock stresses of 0.8 GPa, 1.8 GPa, 0.9 GPa, and 1.7 GPa, respectively. Given the loading direction and the approximate impact velocities, the samples were assigned the labels “200 Ex”, “400 Ex”, “200 Trans”, and “400 Trans”. A more complete description of the shock experiment is included in previous works by Williams et al. [96–98].

The samples were sectioned in the shock direction using a diamond wire saw to minimize the surface damage and in such a way that the basal poles were located within the plane of the fresh surface. The specimens were gently mechanically polished at 1200 grit with SiC paper and then at 50 nm with the Struers (Westlake, OH) OPS non-dry suspension. Care was taken to immediately rinse the surface with ethanol and sonicate for 15 minutes in ethanol to remove the colloidal suspension from the cracks and voids. Specimens for EBSD were then ion milled in a Fischione 1060 ion mill (Export, PA) at 5 kV for 3 minutes, 3 kV for 15 minutes, 1 kV for 20 minutes, and at 0.5 kV for 20 minutes. A gun tilt of 3° was used. Samples were imaged and characterized by EBSD in a

TESCAN MIRA3 GMU FEG-SEM (Libušina, Czech Republic). The EBSD data was analyzed in the manner detailed in Chapter 1.

4.3 Results and Discussion

4.3.1 Fractography

Wide-field SEM micrographs of the examined specimen cross-sections are shown below in figure 4.1. At 200 m/s, damage is not visible to the unaided eye in either the extrusion or the transverse direction. By 400 m/s, however, a highly developed spall plane has evolved in the 400 Ex sample, and the 400 Trans sample has spalled completely.

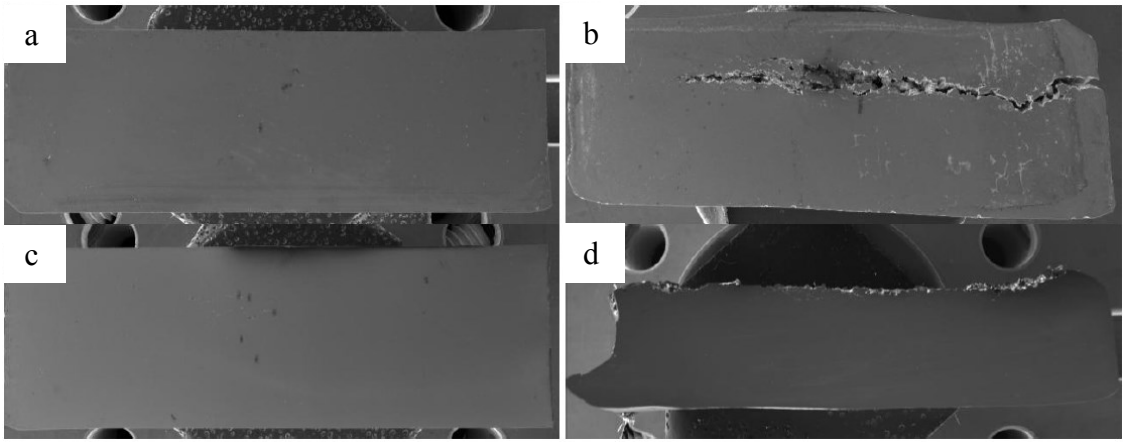

Figure 4.1: Secondary electron SEM micrographs of the spall tested samples. (a) 200 Ex sample (b) 400 Ex sample (c) 200 Trans sample (d) and lower half of the 400 Trans sample.

A closer examination of the 200 Ex sample with SEM revealed voids both near and far from the spall plane, suggesting that the ECAE processed microstructure contains incipient voids. Evaluation of the incipient voids far from the spall plane revealed two

categories. The first category was observed where coarse "stringer" particles had fractured during processing, leaving voids in the gaps, such as those seen in figure 4.2a. This category of voids is observed most frequently, and similar voids that nucleated from fractured precipitates were also reported by Farbaniec et al. [45]. The other category of incipient voids did not appear to involve precipitates, and a particularly large example can be seen in figure 4.2b. Only a few examples of this category of voids were observed; the vast majority incipient voids belonged to those that formed from fractured precipitates.

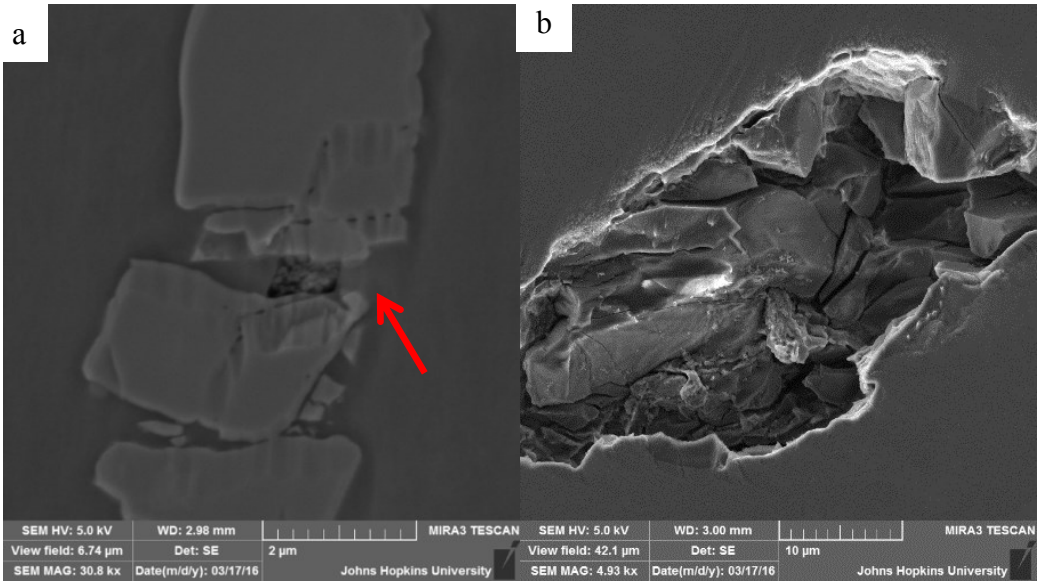

Figure 4.2: Secondary electron SEM micrographs of the 200 Ex sample. (a) A void between fractured precipitates. (b) A large void near of the bottom of the sample that does not appear to involve precipitates.

The two varieties of incipient voids appear to result in different behavior as spall progresses. Figure 4.3 suggests that the voids near precipitates prefer to grow by driving brittle fracture in the precipitates. Note in figure 4.3b that the cracks will grow along near vertically oriented precipitates rather than in the horizontal plane of spall. The sharp

crack tips in figure 4.3a suggest that early growth of voids may occur by crack propagation within the Mg matrix. In addition, voids that are in close proximity appear to form ligaments, as seen in figure 4.3b.

The voids that grow solely out of the matrix have a different morphology than those that grow via precipitate fracture. The voids from precipitate fracture are highly elongated, as shown in figure 4.3. In comparison, the voids formed in the matrix are more equiaxed, as seen in figure 4.4a. These voids frequently contain large clusters of submicrometer voids. The voids in figure 4.4b are approximately 150-200 nm wide. A TEM investigation by Voisin et al. found that the nanoprecipitates in AZ31B measure between 26 and 70 nm, and their spacing may range from 270 nm to 700 nm [99]. The nanovoid spacing approximately corresponds to the lower end of the nanoprecipitate spacing range, but no nanoprecipitates were observed within the nanovoids in this work.

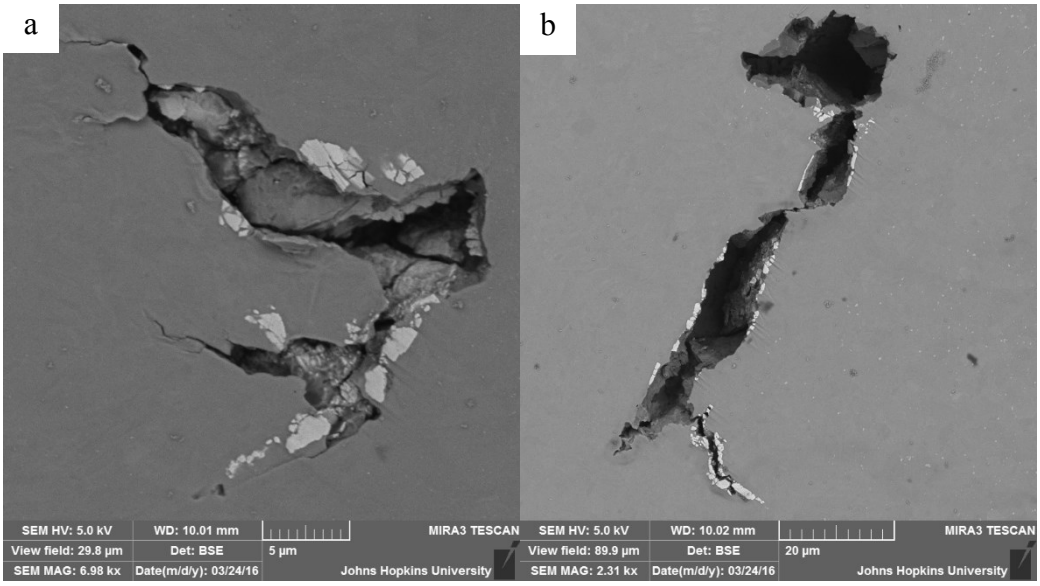

Figure 4.3: Backscattered electron SEM micrographs from the 200 Ex sample. Extrusion and loading directions are vertical. (a) Fractured precipitates line a void that has opened. Note the sharp crack tips. (b) Void growing along three separate precipitate clusters.

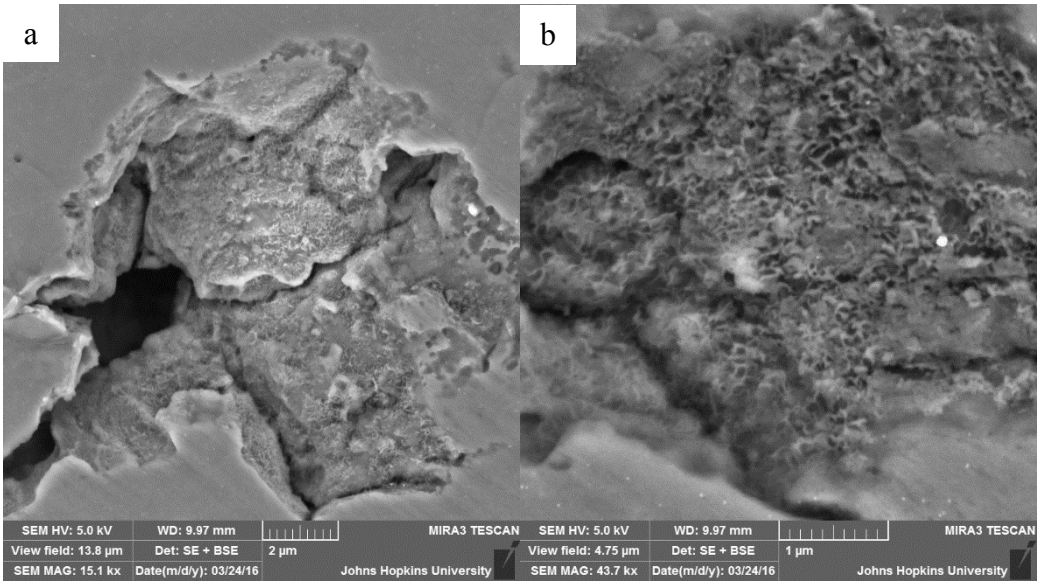

Figure 4.4: Secondary and backscattered electron composite SEM micrographs from the 200 Ex sample. Extrusion and loading directions are vertical. (a) Void that has grown out of the matrix containing submicrometer voids. (b) Enlarged image from (a). The bright spot is an Al-Zn plate-like precipitate.

The 400 Ex samples shows a far greater extent of spall failure than the 200 Ex sample. Similar to Farbaniec et al. findings, a large fraction of the spall surface is covered in nanovoids, which can be seen in figure 4.5a [45]. The 500 nm bright precipitates that are clearly visible in figure 4.5 are thought to be Al-Zn plate-like precipitates [71]. These precipitates have frequently been observed in the current work in regions of nanovoids, although the precipitates themselves are not located within voids. What role they play, if any, in nanovoid formation is unclear. Some regions of the spall surface display faceted surfaces intermixed with local clusters of nanovoids. An example of such a region is shown in figure 4.5b. Here, the nanovoids display elongation in the vertical direction, which is the orientation perpendicular to the spall plane. This morphology suggests that the voids grew in a ductile manner prior to failure. As the spall failure is so advanced, it

cannot be ascertained whether this faceted surface is related to the bridge-joining type of void sheet in the 200 m/s sample seen in figure 4.3b.

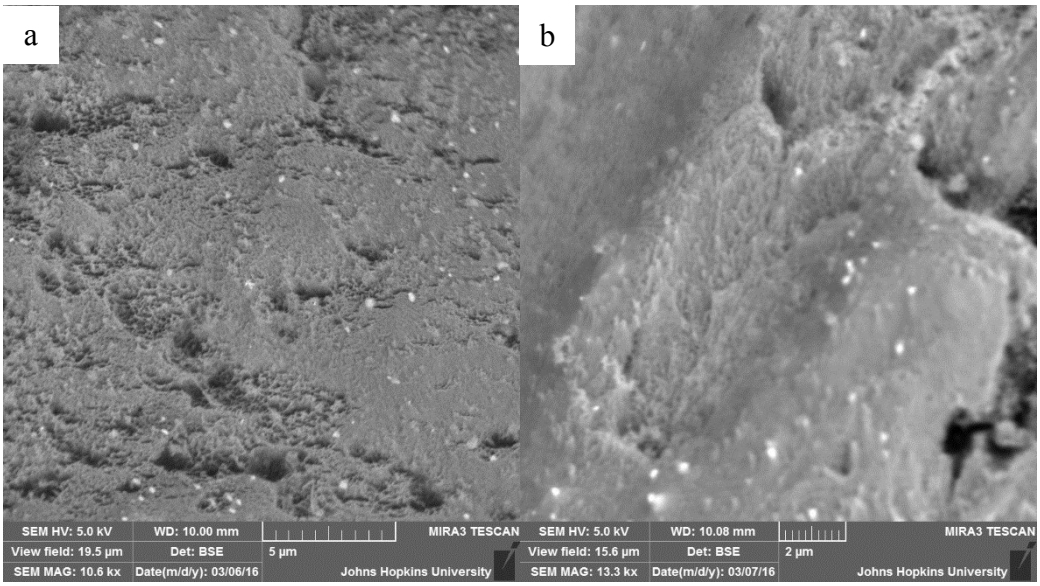

Figure 4.5: Backscattered electron SEM micrographs from the 400 Ex sample. Extrusion and loading directions are vertical. (a) Spall surface showing a large field of nanovoids. (b) Nanovoids and a faceted surface.

Like the 200 Ex sample, the spall damage in the 200 Trans sample is only visible by close inspection in the SEM. Likewise, fractured precipitates can be seen in figure 4.6a to play a critical role in the early stages of void growth. Unlike the 200 Ex sample, however, spall appears more developed, and voids connected by ligaments are frequently observed. Indeed, the voids in the 200 Trans sample display a greater propensity to form ligaments as shown in figures 4.6a and 4.6b.

The 400 Trans sample displays complete spall failure. This behavior suggests that the texture may be playing a role in the spall process. An optical image is shown in figure 4.7. Like in figure 4.6b, and the samples examined by Farbaniec et al., the spall failure in the 400 Trans sample shows significant out of plane features [45]. It is not evident that

multiple spall planes exist, contrary to what was reported by Farbaniec et al. [45]. However, that feature may be obscured by the complete spallation.

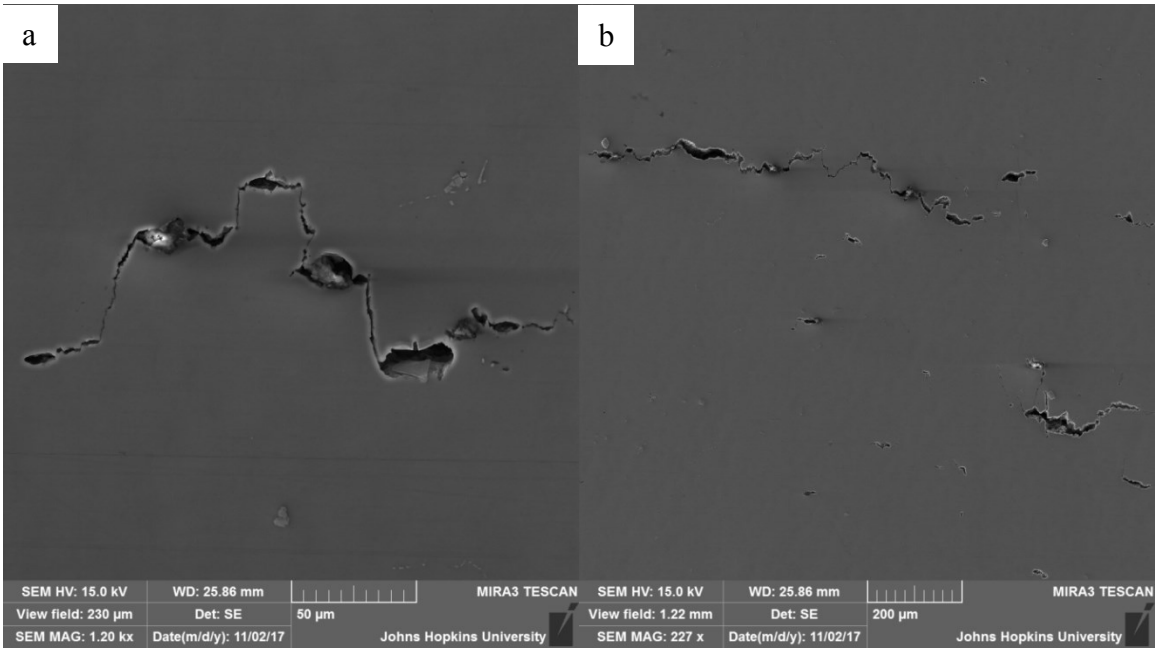

Figure 4.6: Secondary electron SEM micrographs from the 200 Trans sample. Transverse and loading directions are vertical. (a) A series of small voids are connected by ligaments. Note that the edges of the second, third, and fifth voids from the left are decorated by broken precipitates. The center right of the image also contains a fractured precipitate that did not produce a large void. (b) A series of interconnected and growing voids that could be the likely locus of the spall plane.

Figure 4.7: Optical image showing the complete spall failure of the 400 Trans sample.

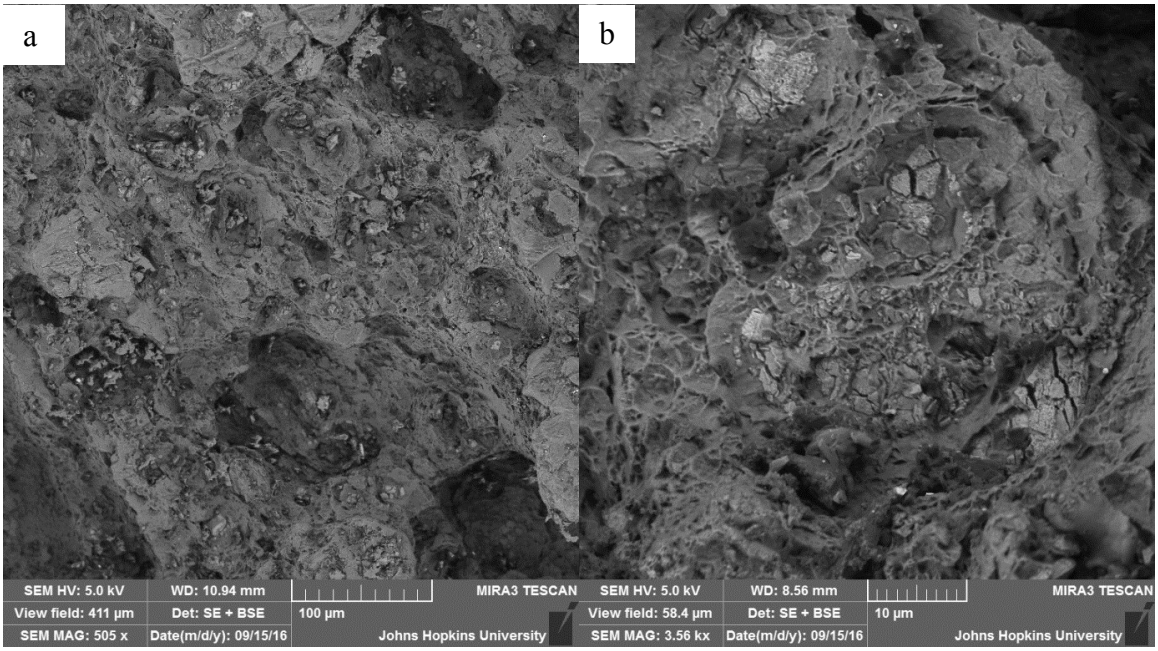

Figure 4.8: Secondary and backscattered electron composite SEM micrographs from the 400 Trans sample. Transverse and loading directions are out of the page. (a) SEM image of the spall surface showing many fracture precipitates. (b) Enlarged SEM image showing two fractured precipitates. The precipitates appear to be couched in large voids.

Unlike in the extrusion orientation samples, the failure surface of the sample loaded in the transverse direction is littered with clusters of fractured precipitates, as indicated in figure 4.8a. In addition, the precipitate clusters appear to reside in shallow pits that are reminiscent of void pits, such as those seen in figure 4.8b. Figure 4.8b also displays the presence of microvoids around the precipitates. Microvoids are the most common size void observed in this sample and can be seen in figure 4.9. Voids approximately 1 µm in diameter are also very common. Although they are all roughly the same size, some of these clusters contain precipitates while others do not. Figure 4.10 contains SEM images of 1 µm void clusters with and without nanoprecipitates. Nanovoids the size of those observed in the extrusion orientation sample have yet to be seen along the transverse orientation failure surface.

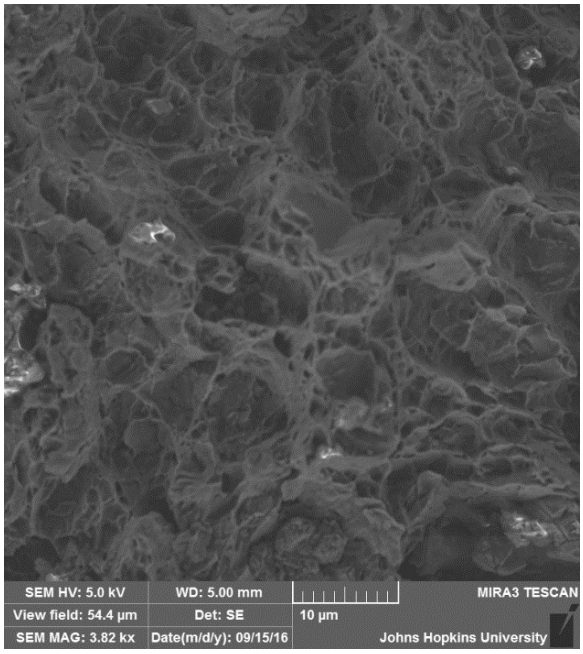

Figure 4.9: Secondary electron SEM micrographs of the 400 Trans sample. Transverse and loading directions are out of the page.

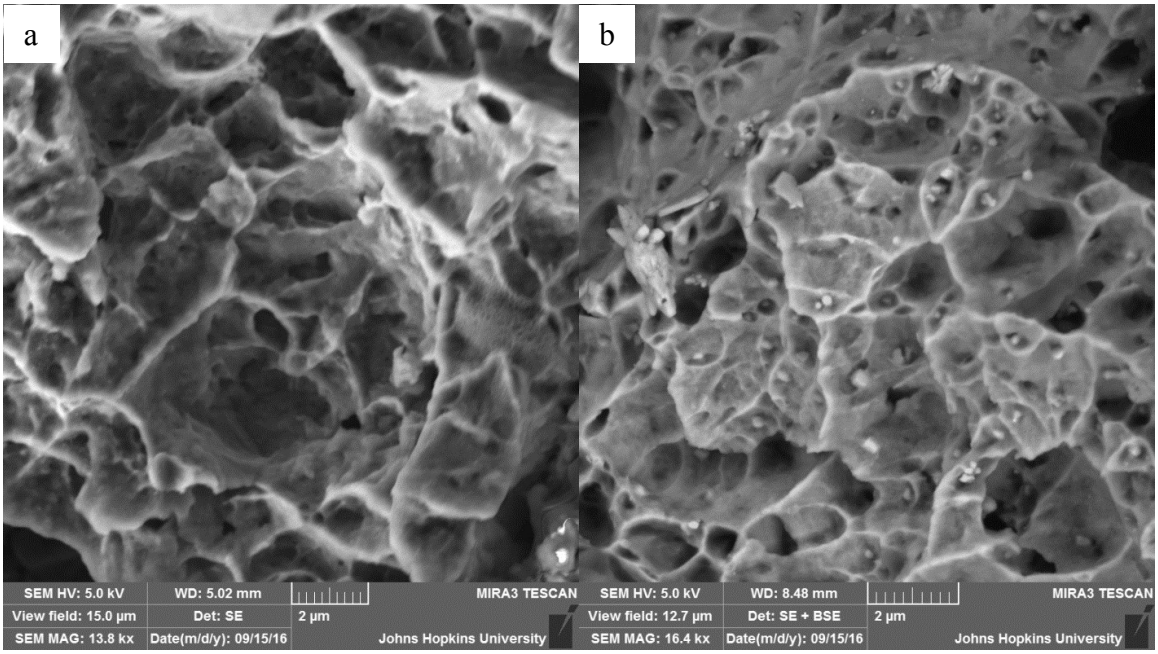

Figure 4.10: Secondary electron and composite SEM micrographs of the 400 Trans sample. Transverse and loading directions are out of the page. (a) Micrometer sized void clusters lacking nanoprecipitates. (b) Micrometer sized void clusters with nanoprecipitates in more than 50% of the void, indicating precipitate fracture.

4.3.2 Microstructural Examination

EBSD was used to inspect the microstructure both away from the spall plane and near smaller voids immediately surrounding the spall plane. The areas adjacent to the spall plane and near ligaments were unable to be indexed, presumably due severe deformation.

The microstructure around the middle of the 200 Ex sample displays no significant change in grain size from the as-processed material, but the pole figure, seen in figure 4.11a, displays an overall weaker texture and a secondary pole near the plane normal. Twins, mostly of the $\{10\bar{1}2\}\langle\bar{1}011\rangle$ extension type, were found to constitute 4.0% of the indexed area. When looking near a horizontal void, the twin fraction increases to 6.7% of the indexed area, but the pole figure in figure 42b shows a significant strengthening of the secondary pole and an evolution of a tertiary orientation. The apparent disparity between the fraction of directly observed twins and the strength of the twinning orientation in the pole figure may be reconciled by study of the IPF map in figure 4.11b. It reveals an increase in the number of grains with a basal pole near the plane normal. It is likely that many of these grains are extension twins that have entirely consumed their parent grains.

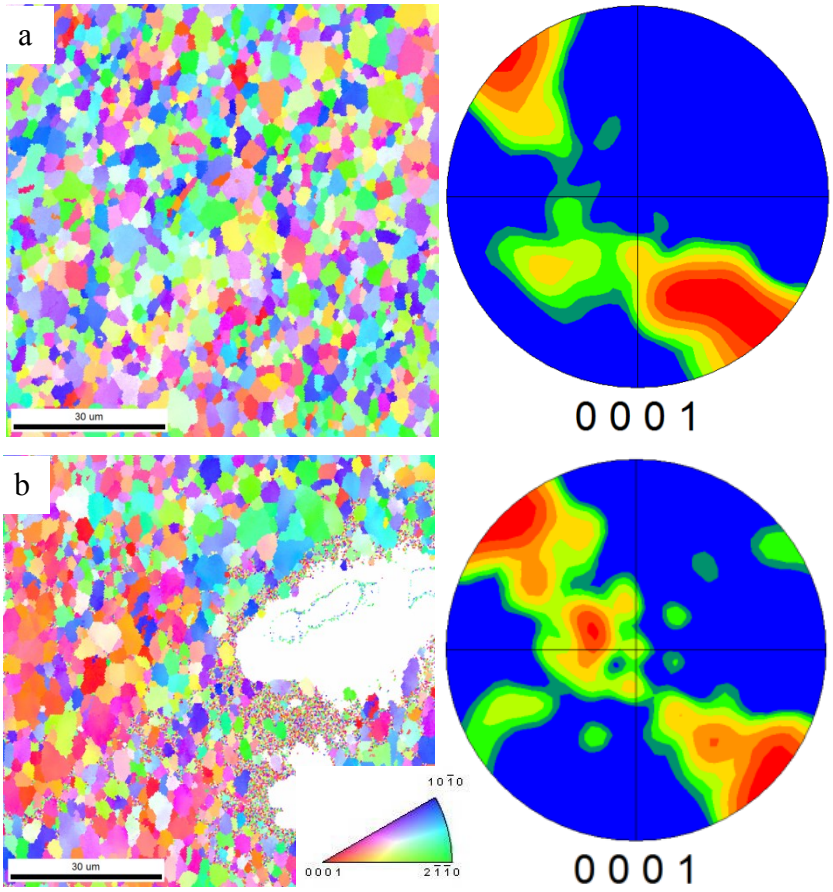

Figure 4.11: Inverse Pole Figure (IPF) maps and basal pole figures from the 200 Ex sample. Extrusion and loading directions are vertical. (a) Map (left) and pole figure (right) from an area below the spall plane and far from growing voids (b) Map (left) and pole figure (right) of an area on the left side of a large, horizontal void.

Figure 4.12a shows the microstructure that has likely evolved from figure 4.12b Many of the grains are deformed, elongated along the shock direction, and possess the twinning orientation. While the nonindexed regions in figures 4.12a and b appear to be similar in size, the regions in figure 4.12a belong to a large, mature void much larger than what is shown within the image's field of view. In the pole figure within figure 4.12a, the twinning orientation has strengthened to become the primary orientation. However, the microstructure near two small voids in figure 4.12b remains largely similar to that of figure 4.11a. Most of the twinning orientation observed around the small voids appears to

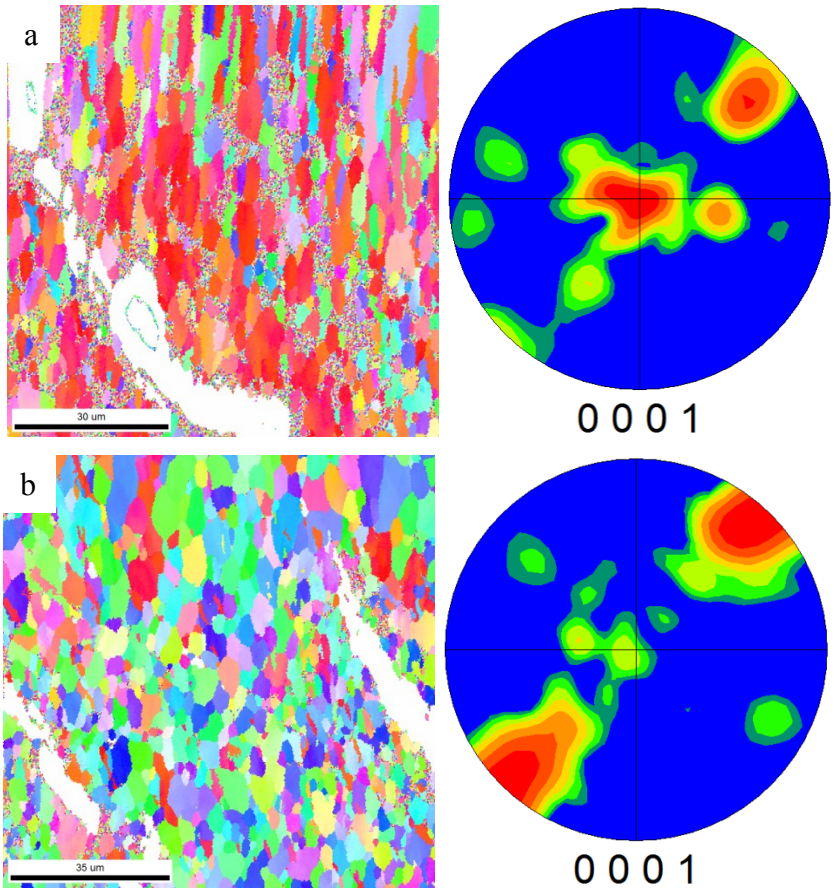

Figure 4.12: Inverse Pole Figure (IPF) maps and basal pole figures from the 400 Ex sample. Extrusion and loading directions are vertical. (a) Map (left) and pole figure (right) from an area near a large voids (b) Map (left) and pole figure (right) of an area near two small voids. The nonindexed regions in (a) all belong to one void that extends far beyond the view field.

be from lenticular twins, rather than twins that have consumed parent grains. There also appears to be some grain refinement near the small voids.

Figure 4.13a depicts the microstructure far from the spall plane in the 200 Trans sample. It is largely unremarkable except for the very large grain at the end. This grain seems to constitute almost the entirety of the out of plane basal twinning orientation in the pole figure. In addition, an extension twin variant appears to have been activated in the plane of the sample. Significant twinning is not readily apparent in the IPF map near a large void in figure 4.13b. However, the pole figure shows that in comparison to the

extrusion orientation samples, the out of plane twin variant is weaker, but three other twin variants have been activated – two more variants than have been observed in the extrusion samples. The area around the small void in figure 4.13c follows the trend observed previously, where the area degree of twinning and activated twin variants is highly similar to the area in the middle of the sample.

The IPF map from the middle of the 400 Trans sample in figure 4.14a displays a significant change from those in figure 4.12a and figure 4.13a. Most of the twinning orientation present appears to be in the form of nearly vertical lenticular twins, many of which have nucleated twins across the grain boundary. Figure 4.14b displays a similar behavior, but in addition, vertically elongated grains are also observed. Due to the apparent tendency for voids to form ligaments at smaller sizes, it was difficult to find a large void of comparable size to those in other samples.

4.3.3 Role of Precipitates in Spall Behavior

As noted by Farbaniec et al, voids in these AZ31B samples appear to grow in the early stages by decohesion between the Mn-Al intermetallic "stringers" and the Mg matrix [45]. The source of these voids appears to almost invariably be from precipitates that fractured during processing. There are qualitative differences in the immediate growth following the decohesion stage of growth between the orientations. In the Extrusion direction samples, where possible, the voids grow along the direction of the stringers as seen in figures 4.3 and 4.12a. As the voids follow the orientation of the

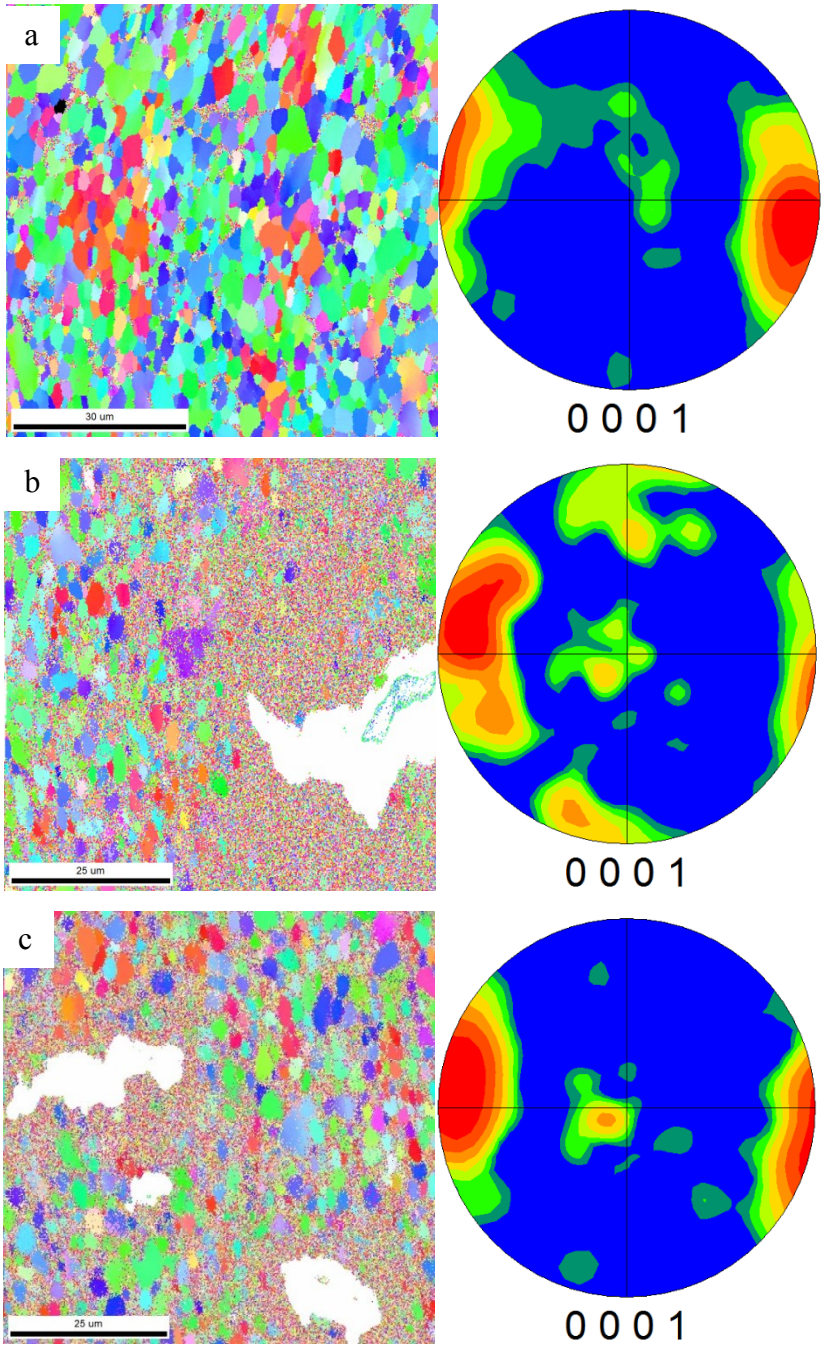

Figure 4.13: Inverse Pole Figure (IPF) maps and basal pole figures from the 200 Trans sample. Transverse and loading directions are vertical. (a) Map (left) and pole figure (right) from an area well below the spall plane. (b) Map (left) and pole figure (right) from an area near a large void. (c) Map (left) and pole figure (right) of an area near two small voids.

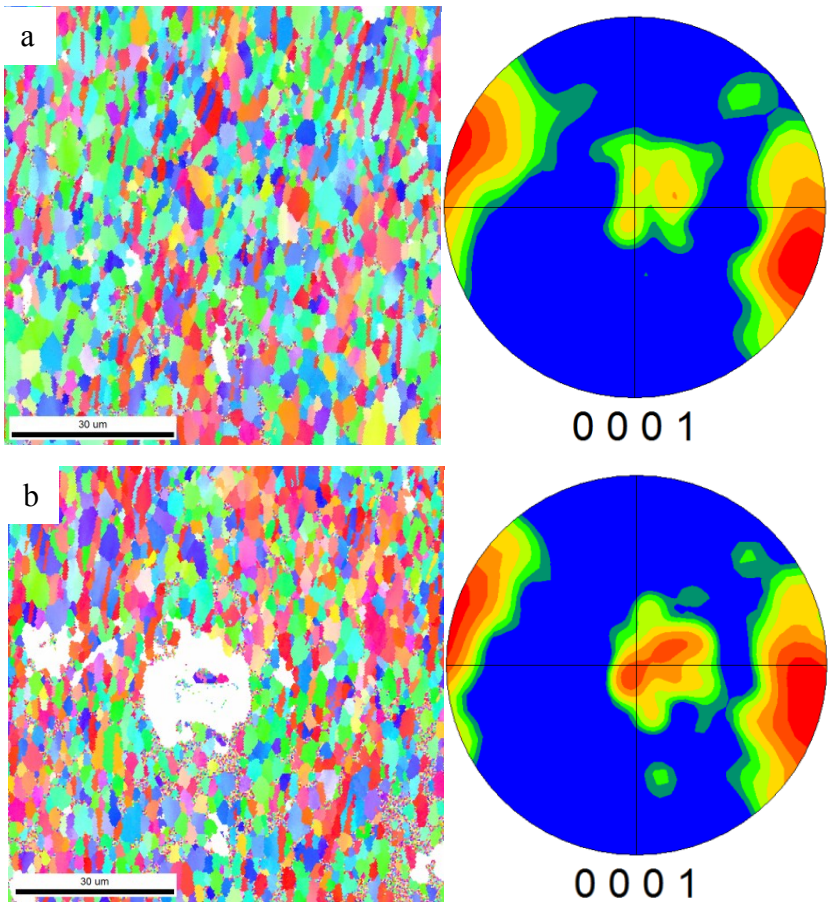

Figure 4.14: Inverse Pole Figure (IPF) maps and basal pole figures from the 400 Trans sample. Transverse and loading directions are vertical. (a) Map (left) and pole figure (right) from an area well below the spall plane.(c) Map (left) and pole figure (right) from an area near a small void.

stringers, void growth is not limited to the horizontal direction, but may also be in the vertical direction. When the sites for growth in this mode are apparently exhausted, the voids transition to a more ductile growth in the horizontal direction. This is the stage where nanovoid formation is expected to take over from decohesion. After growing to the 100 μm range, the voids begin to link up by the formation of ligaments. Nanovoid and ligament formation appear to be the terminal stage of void growth.

Void formation during shock loading in the Transverse direction shares the same source of voids as the Extrusion direction in the fractured precipitates, but the precipitate

decohesion stage of growth appears to be shorter in duration. Ligament formation begins at much smaller voids sizes, as seen in figure 4.15b, joining primarily horizontal voids. It may be this difference in the direction of initial void growth that produces a delay in the formation of a spall plane in the Extrusion direction, and thus delays the spall failure in the Extrusion direction relative to the Transverse direction.

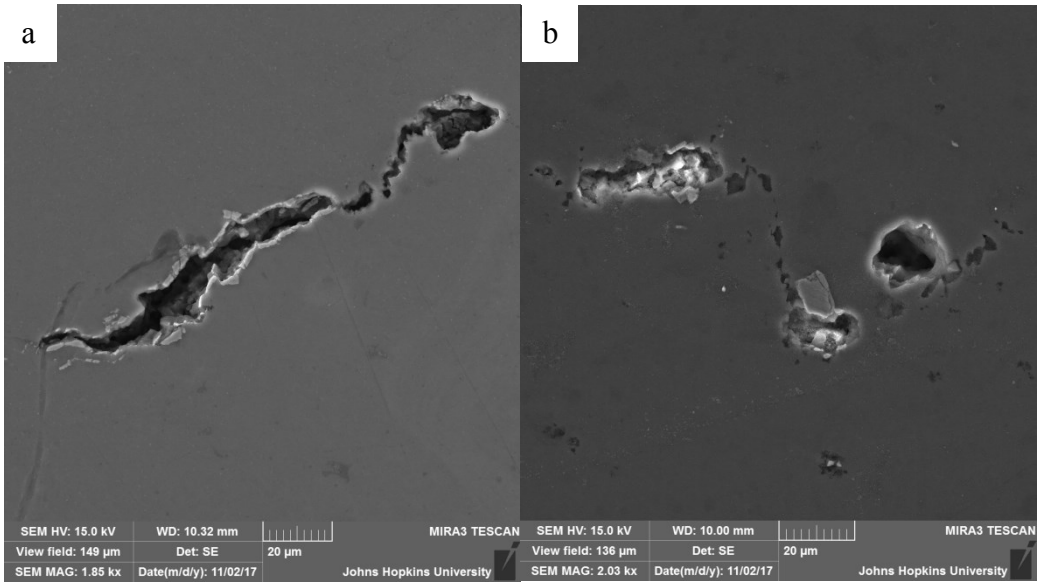

Figure 4.15: Secondary electron SEM micrographs. Loading directions are vertical. (a) 400 Ex sample. Note the stringer precipitates decorating the rim of the void. (b) 400 Trans sample. Here, the void does not grow much beyond the precipitate before forming a ligament.

While the large precipitates clearly play a critical role in the spall behavior of AZ31B, the differences in void size, morphology, and nucleation between the two orientations of samples tested at 400 m/s suggests that sample orientation and microstructural variations also impacts the spall behavior. AZ31B is known to contain Mn-Al nanoprecipitates, but these precipitates do not appear to play a role in the formation of nanovoids in the Extrusion direction [72,99]. It is possible that nanoprecipitates within the nanovoids are below the resolution of this SEM or that they

were removed during sonication. An explanation is offered in the work by Wielewski et al, which suggests that strain incompatibilities across grain boundaries are able to nucleate voids [42]. It may be the case that certain grain boundary triple junctions are weaker than the intermetallic-matrix interface.

Larger, approximately micrometer sized voids are observed on the Transverse direction spall surface. Some of these voids contain nanoprecipitates, but their presence varies within the sample. Where the precipitates are present, more than half of the voids contain them, suggesting that void nucleation occurred by precipitate fracture, rather than decohesion. However, the voids appear to be the same size even where the precipitates are not present. This would appear to suggest that void size in this sample is largely independent of precipitate size. It is unclear whether the discrepancy in the presence of nanoprecipitates occurs due to regional variations in precipitate distribution, as noted by Voisin et al., or local microstructural effects [99].

4.3.4 Orientation Dependence of Spall Behavior

The different orientations examined exhibit somewhat different basal orientations. The Extrusion direction samples possess a basal pole with inclinations approximately 50° inclined from the horizontal axis, while the Transverse direction samples have a basal pole inclined only 5° on average from the horizontal axis. Since many of the twins observed were extension type twins, this suggests that twinning was slightly favored during the relaxation phase in the Extrusion direction samples, while twinning was favored in compression phase in the Transverse direction samples. The opportunity for detwinning during relaxation in the Transverse direction samples may offer an

explanation for why a greater number of lenticular twins are observed. And, while it is clear from the present work that twinning does occur during shock, the growth of larger voids also drives twinning and apparent plastic deformation. In many cases, the lenticular twins grow so as to completely consume the parent grains, resulting in major changes to the local texture. Given the large tensile stresses involved during spallation, it is not clear what direct effect the microstructural reorientation has on further void growth.

A difference in the twin variants is observed near large grains in the extrusion and transverse samples. Both orientations, even far from voids, seem to favor the twin variant that produces a basal pole in the out of plane direction. In the extrusion direction, another variant with the basal poles in plane is observed. Some maps in the 200 Trans sample displayed two additional, nearly vertical variants. Possibly, due to the inability to find larger voids in the 400 Trans sample, only the out of plane variant was observed. However, the 400 Trans sample largely preserved the lenticular shape of the twins, and both figures 4.14a and 4.14b show long series of vertical lenticular twins and elongated grains. These microstructural features bear a striking resemblance to the vertical ligaments observed in the SEM micrographs. It is a possibility that these features ease the formation of the ligaments, limiting the early growth of the voids.

4.4 Conclusions

Samples of AZ31B were ECAE processed via the $4B_C$ route. In turn, these samples were used to perform spall recovery experiments at 200 and 400 m/s with the sample disk normal parallel to the extruded Extrusion and Transverse directions. The samples were sectioned and then fractography and EBSD were performed. It was found

that Mn-Al precipitates which had fractured during processing were the initial source of voids. These voids initially grew by decohesion between the precipitates and the matrix before transitioning to a more ductile growth mode. Differences in the spall surface between the testing orientations were observed. Mature voids in the Extrusion direction sample display fracture surfaces with large numbers of nanovoids containing no nanoprecipitates, but voids in the Transverse direction sample displayed larger, sub-micrometer voids that intermittently contained precipitates. EBSD revealed that extension twinning played a role in the growth of larger voids, with the area near the mature voids containing an increased area fraction of twinning orientations. The 400 Ex sample displayed large numbers of lenticular twins and elongated grains. The combination of these features is hypothesized to play a role in ligament formation.

5. Effect of Strain-rate on the Microstructural Evolution of Pure Mg during ECAE

5.1 Introduction

Aside from texture evolution trends common to most HCP metals, a full understanding of the effect of processing parameters on microstructural evolution during ECAE is incomplete. A significant number of studies have investigated the effect of processing parameters to remedy this deficiency; the majority have focused on the effects of route design and temperature. Out of these efforts, exceptionally refined microstructures have been produced through a combination of hybrid routes and a step-down temperature technique [27,30,38,78,100]. However, the effect of extrusion rate on microstructural evolution has been largely overlooked. While there are no known examinations of the effects of strain rate in magnesium, there are a few studies in other material systems. Berbon et al. extruded pure Al at various rates, but reported no effect on grain size or texture [101]. However, they observed that recovery appeared to occur more readily at lower extrusion rates [101]. More recently, Kim et al. reported that the deformation mechanisms transform from primarily twinning to slip with decreasing extrusion rate in commercially pure Ti [102]. Although these findings are limited, they merit further inspection, as they suggest the possibility of texture modification by twinning without compromising grain size reduction and the associated Hall-Petch strengthening.

5.2 Experimental Methods

Samples of pure Mg were extruded up to four passes by the B_C route at 0.127, 0.381, and 0.762 mm/s under a constant temperature of 250°C. The samples were characterized via EBSD after each pass. The details of the processing method are as described in Chapter 2. As in the earlier characterization of pure Mg, the initial grain size was approximately 19 mm with an as-cast texture. Thus, care was taken to collect data in areas far away from each other to avoid sampling the same parent grains multiple times. The EBSD analysis was performed in the typical manner.

5.3 Results and Discussions

5.3.1 Microstructure After the First Pass

The microstructures and textures that appear after the first pass are shown in figure 5.1 for the three extrusion rates. The IPF maps demonstrate that while DRX is active, it is incomplete after the first pass for every strain rate. The microstructures displayed significant image to image variation in the extent of recrystallization. The reasons for this are twofold: recrystallization is orientation dependent, and the parent grains are large relative to the size of the images. Al-Maharbi et al. have reported that the ease of recrystallization is dependent on the ease of basal slip [78]. Grains where basal slip was activated displayed significant recrystallization. Grains where slip was difficult appeared to have twinned profusely by the $\{10\bar{1}2\} < 11\bar{2}0 >$ extension system before activation of DRX and show less recrystallization. Because the grains were so large, the deformation activity of a single grain tended to dominate the field of view. The parent grains recrystallize where slip is easy and the recrystallized grains have readily adopted a

45° inclination from the extrusion axis; typical of the ECAE texture. Plastically hard grains have largely retained their original texture. Despite the orientation dependence of recrystallization and large image to image variations at all strain rates, the higher strain rates show a distinct increase in the average area fraction that was recrystallized, as can be seen in figure 5.2. This behavior suggests that the higher strain rates are more effective at breaking down plastically hard orientations.

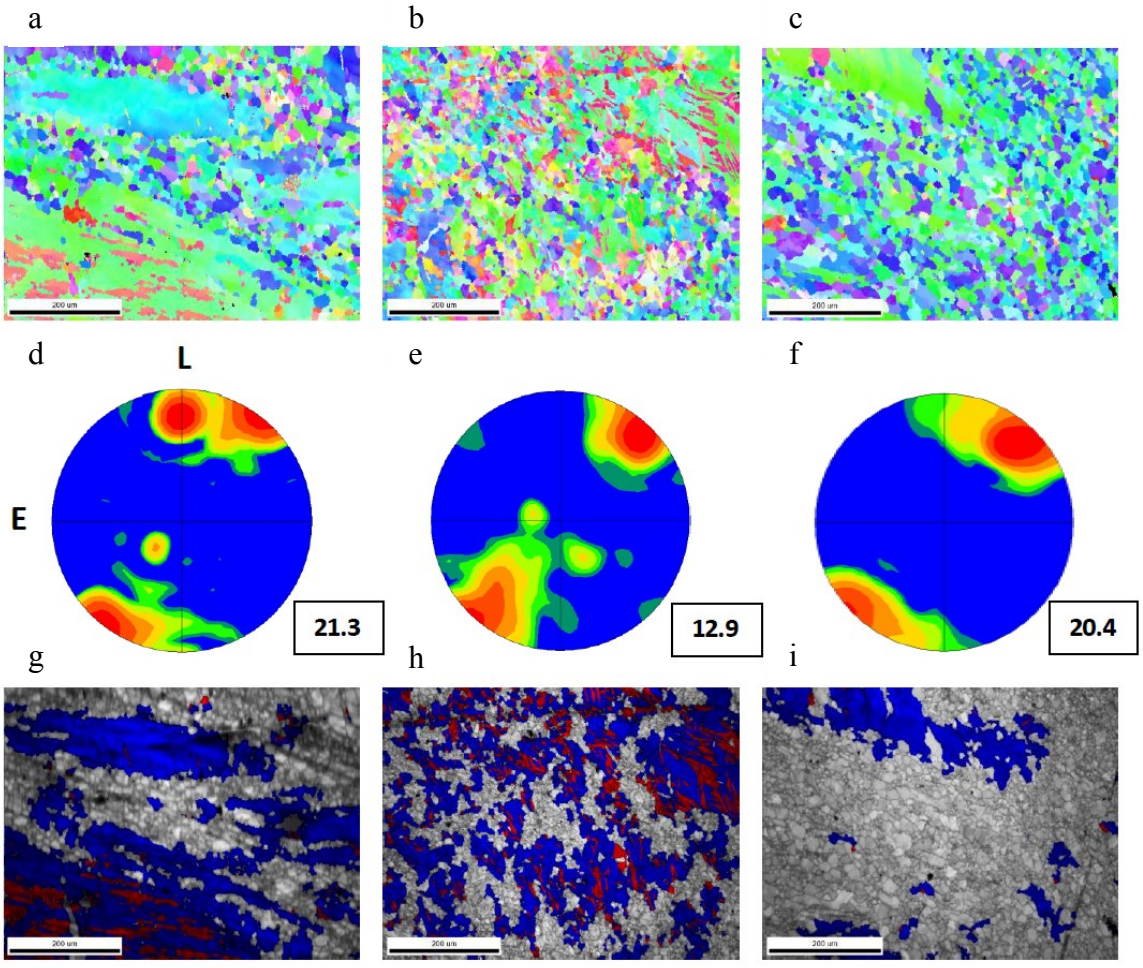

Figure 5.1: (a-c) Inverse Pole Figure maps after the first pass from the 0.127, 0.381, and 0.762 mm/s samples. (d-f) (0001) Pole figure maps with maximum intensity from the samples above. (g-i) Parent grains containing twins are colored in blue while the coherent $\{\mathbf{10\bar{1}2}\} < \mathbf{11\bar{2}0} >$ extension twins are displayed in red.

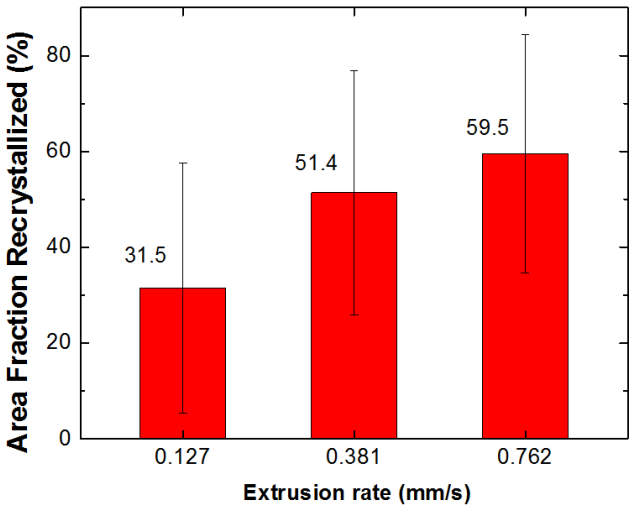

Figure 5.2: Average area fraction of recrystallized grains after the first pass for each extrusion rate. Pure magnesium extruded via ECAE at 250 °C.

An examination of the microstructures in figure 5.3 offers insight into the active DRX mechanisms. Figure 5.3a contains a number of extension twin variants, but DRX is only observed in one variant, an observation also reported by Al-Samman et al. [50]. In the upper left corner, a number of grains appear to be nucleating heterogeneously at low angle boundaries (boundaries less than 15° misorientation). The hetereogeneous nucleation suggests dDRX, but the mobility of low angle boundaries are generally too low for the mechanism to activate [47]. Figure 5.3b shows another region with the low and high angle boundaries highlighted. Here, twins and DRX grains can be seen nucleating on opposite sides of mixed high and low angle boundaries. Between the two images, the apparent dependence on boundaries for nucleation and the nonuniformity of the nucleation sites all suggest that dDRX is active. As a result, we can expect the fully refined microstructures to have large variations in grain size distribution.

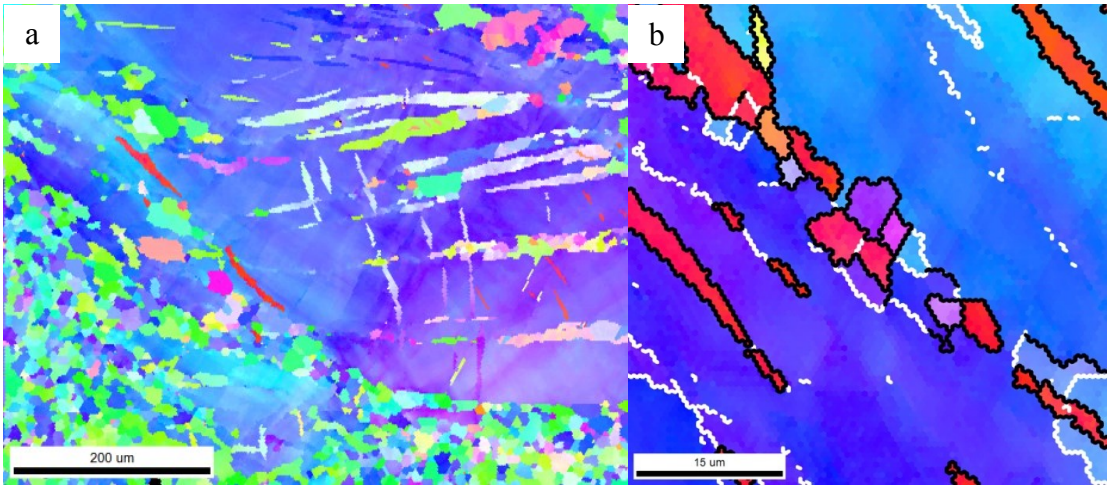

Figure 5.3: Pure magnesium extruded via ECAE at 250 °C. (a) IPF map showing DRX nucleation in multiple areas in 0.381 mm/s sample. (b) Enlarged IPF map of a DRX nucleation site in the 0.381 mm/s sample. Black lines are high angle boundaries, and white lines are boundaries with misorientations between 5° and 15° degrees.

5.3.2 Microstructure After the Multiple Passes

IPF maps for the subsequent extrusions can be seen in figure 5.4. With subsequent passes, the remaining parent grains are broken down. Remnant parent grains are infrequently observed after the $2B_C$ pass, and none after further passes. As the parent grains are almost entirely gone, the orientations of the parent grains, and thus the recrystallization patterns, can no longer be detected. Bands of similarly clustered orientations may be attributed to local variations in recrystallization mechanisms, and were less frequently observed following additional extrusions. Largely consistent with past findings, the average recrystallized grain size was found to reach an approximate saturation or minimum value, as shown in Table 5.1 [101]. Even with twins and parents discounted, the grain sizes still show significant variation, matching both the observation regarding the large standard deviations relative to the means following recrystallization in Chapter 2, and the prediction of a wide range of grain sizes due to dDRX made after noting the heterogeneous nature of recrystallization after the first pass. The 0.762 mm/s

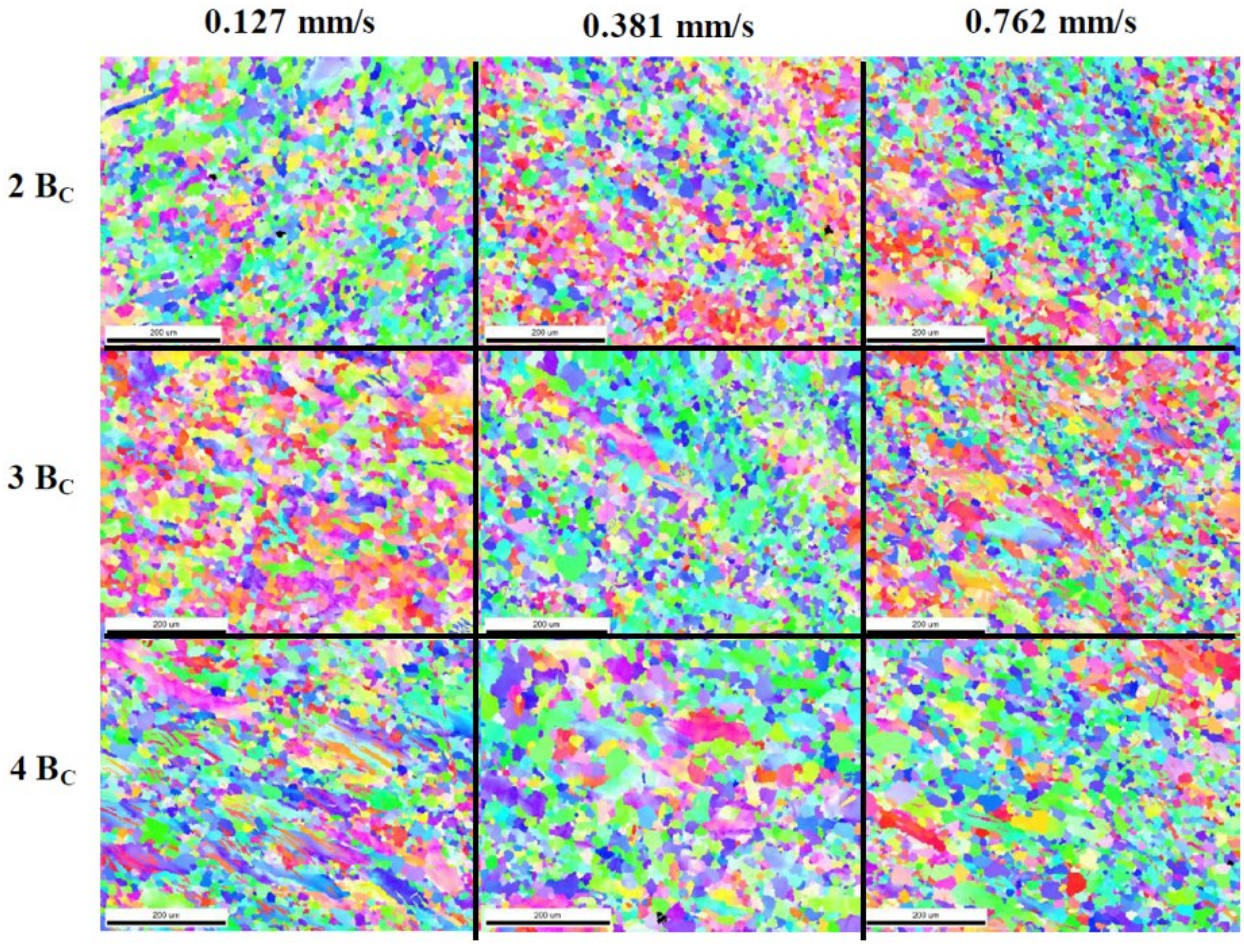

Figure 5.4: IPF Maps from passes $2B_C$ through $4B_C$. Pure magnesium extruded via ECAE at 250 °C.

Extrusion Rate (mm/s)	0.127	0.381	0.762
$2B_C$	27.2±20.0	31.9±26.7	28.5±23.6
$3B_C$	40.3±31.9	42.6±36.5	25.8±20.0
$4B_C$	43.4±35.5	47.8±38.5	30.3±20.4

Table 5.1: Area average grain size for each extrusion condition. Twins have been discounted.

extrusion rate does exhibit a lower average grain size than the other rates after passes $2B_C$ and $4B_C$.

5.3.3 Grain Size and its Distribution

A partial explanation for the large variation in average grain size is found by examining how the EBSD analysis program defines a grain with misorientation angle. Figure 5.5 displays two unique grain color (UGC) maps from the same view field. In figure 5.5a, 15° of misorientation is used to define the grain boundary, and the high angle boundaries are highlighted. Notice that a number of the larger grains are highly deformed and segmented, containing a number of relatively high angle boundaries within them. Figure 5.5b uses 5° of misorientation to define the grain boundary. Many of the severely deformed grains are replaced and the microstructure appears overall, more uniform and well-equiaxed. This suggests that the consistently large variation can be attributed to the large, deformed grains. This behavior is an expected component of a steady state dDRX microstructure. To paraphrase Chapter 1.1.5, the nucleation of grains during dDRX is fundamentally heterogeneous in both time and space. Thus, as recrystallization progresses, a given microstructure will consist of grains in all stages of dDRX recrystallization, from new, small, dislocation-free grains to old, large, heavily deformed grains. Because both new and old grains simultaneously coexist within the microstructure, a measurement of the grain size will naturally produce a wide variation.

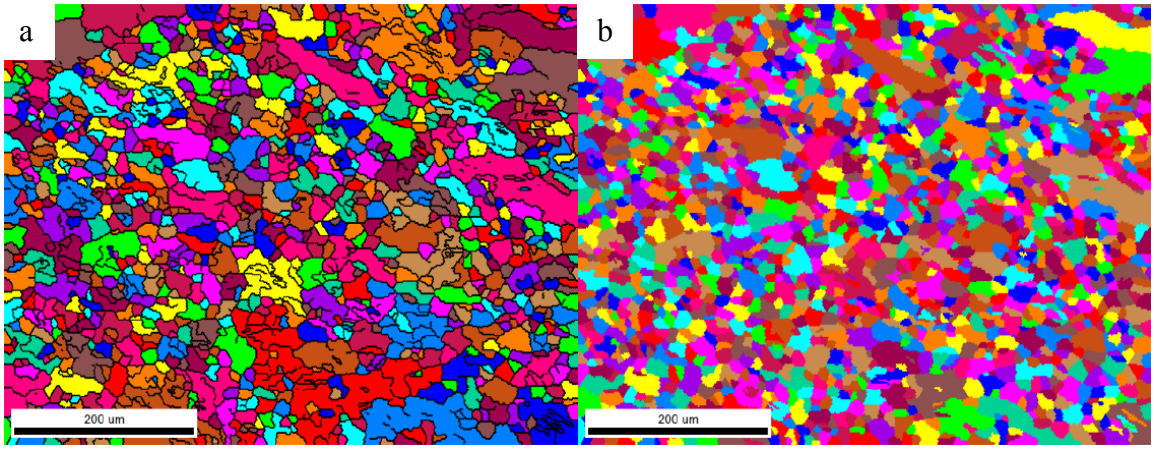

Figure 5.5: Unique grain color maps from the same view field. (a) Grain boundary defined as 15° degrees of misorientation. Black lines are also 15° degrees. (b) Grain boundary defined as 5° degrees misorientation. Pure magnesium extruded via ECAE at 250 °C.

The change in grain size for the final two passes of the 0.762 mm/s rate sample is unexpected. While under the action of cDRX, the subgrain size is known to be sensitive to strain rate. During dDRX, where there is long range grain boundary motion, the grain size is expected to be largely independent of strain rate. An explanation for the smaller average grain size for the higher processing speed can be seen in the comparison of the grain size distributions shown in figure 5.6. The grain size distributions of the strain rates after four passes show that the 0.762 mm/s rate sample has a grain size distribution that is similar to the other passes, in accordance with expectations, but it has a reduced maximum grain size. This suggests that the 0.762 mm/s rate is more effective at breaking down large grains than the lower rates. Here, a 5° misorientation was used to show that this effect was independent of the effect of misorientation definitions on the homogeneity of the microstructure.

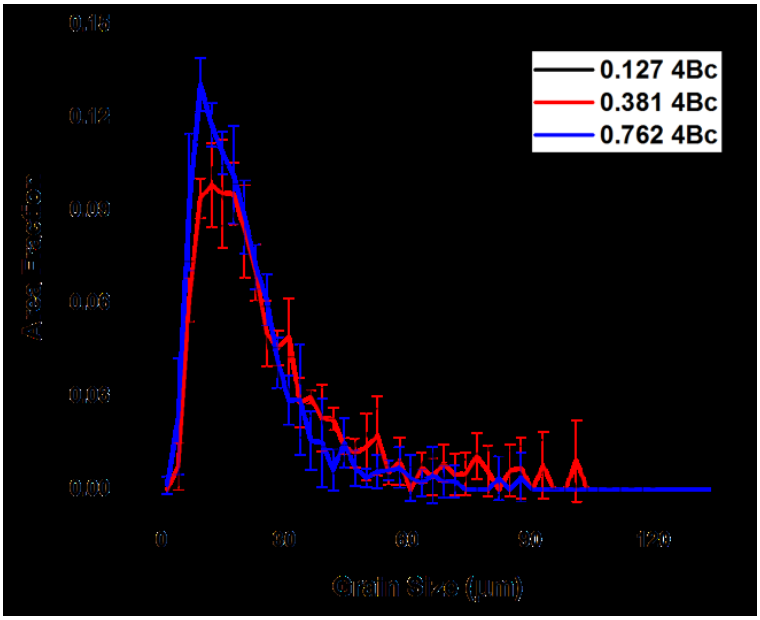

Figure 5.6: Grain size distribution of the various rates after four passes. 5° misorientation is used to define the grain boundary. Pure magnesium extruded via ECAE at 250 °C.

5.3.4 Mechanisms of Microstructural Evolution

It is apparent that DRX activity is the primary driver for the microstructural evolution of magnesium in the early stages of deformation. A number of investigators have examined magnesium and its alloys to better understand the underlying DRX mechanisms. Extensive DRX limited to twins has been reported by a number of groups including Al-Samman et al. [103]. Agnew has also provided evidence for both continuous DRX, where accumulated dislocation networks recover into a recrystallized structure, and discontinuous DRX which occurs by the bulging mechanism in AZ31B [46,69]. Both DRX located within twins and apparent DRX at existing boundaries are also observed in this work. Multiple instances were found where DRX grains nucleated at intermediate and low angle boundaries without outward evidence of assistance by grain boundary bulging, as highlighted in figure 5.3b. In some cases, recrystallized grains were accompanied by an extension twin. Many of these recrystallized grains appear to grow

preferentially along these low-to-intermediate boundaries resulting in grains that are non-equiaxed. A number of these low angle boundaries lie close to the shear direction, and thus, preferential growth along these low-to-intermediate boundaries offer an explanation for the presence of highly elongated recrystallized grains even after 4 passes, such as those seen in the 0.127 mm/s $4B_C$ UGC map in figure 5.7.

5.3.5 The Influence of Extrusion Rate on Twinning

After multiple passes, the 0.127 mm/s and 0.762 mm/s strain rates tend to exhibit more extension twins that the 0.381 mm/s rate. While it is likely that the higher strain rate drives the formation of twins in the 0.762 mm/s sample, an explanation is not readily available for the twins observed in the 0.127 mm/s rate. Hence, the twin volume fraction as a function of grain size was examined to determine whether the behavior was due to a grain size effect. A chart showing the twin volume fraction below and above the *overall* average grain size is shown in figure 5.8. There is no apparent difference in the twin volume fraction between the 0.762 mm/s and 0.127 mm/s samples in either the less than or greater than 35 μm categories.

As the effect is not a result of grain size, it is currently unclear why the 0.127 mm/s has a higher twin volume fraction than the 0.381 mm/s sample. An alternate hypothesis is that the high twin volume fraction for the lower 0.127 mm/s rate is the product of maintaining favorable grain orientations and morphologies for twinning during the four passes. Figure 5.9 shows an IPF map of the 0.127 mm/s sample after four passes. Twins can clearly be seen in grains oriented favorably for twinning and generally along the long axis of elongated grains, grains that tend to be broken down at higher rates.

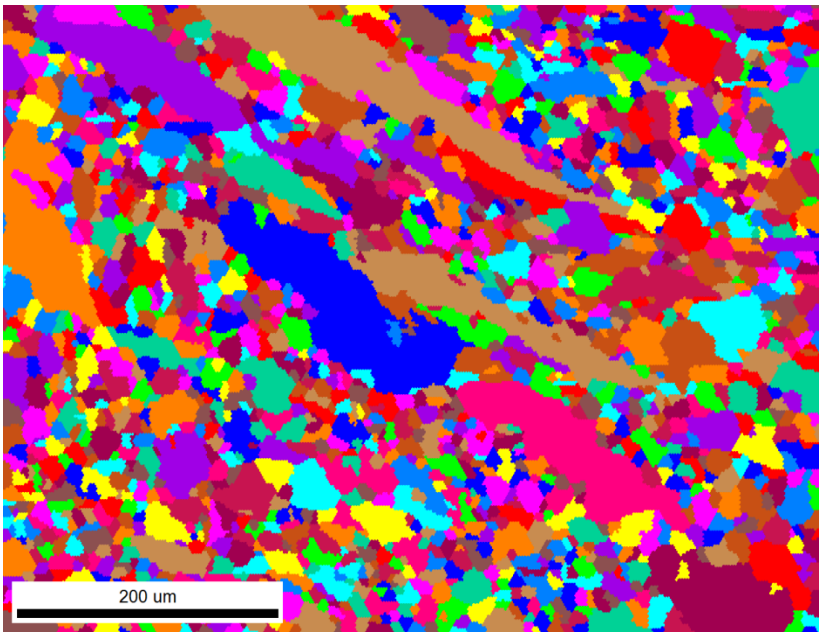

Figure 5.7: Unique grain color map of the 0.127 mm/s $4B_C$ sample. A 15° of misorientation was used to determine grain size.

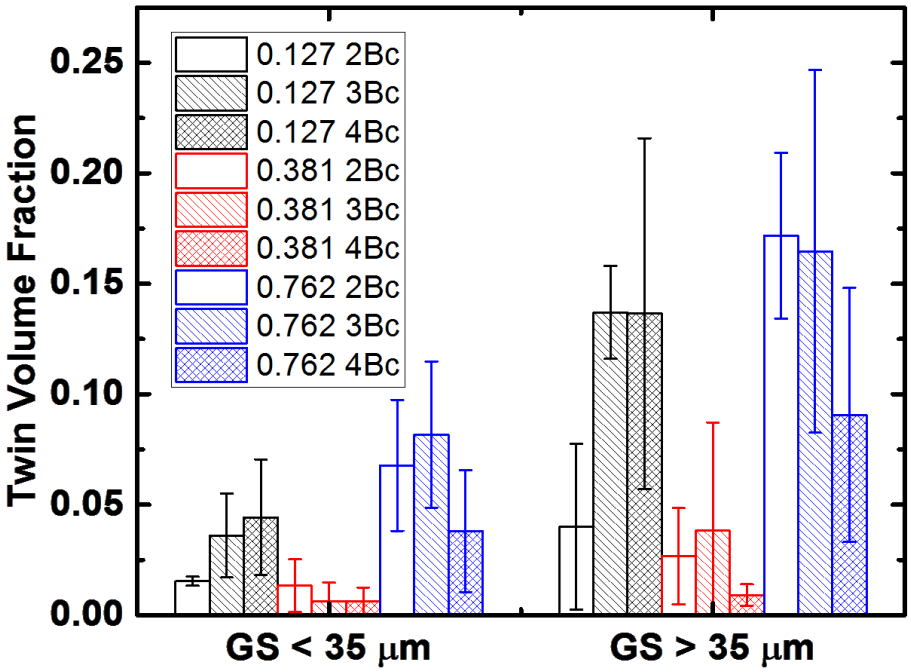

Figure 5.8: Twin volume fraction normalized by the fraction of the view field that contained twins plotted for average grain sizes above and below 35 μm. Pure magnesium extruded via ECAE at 250 °C.

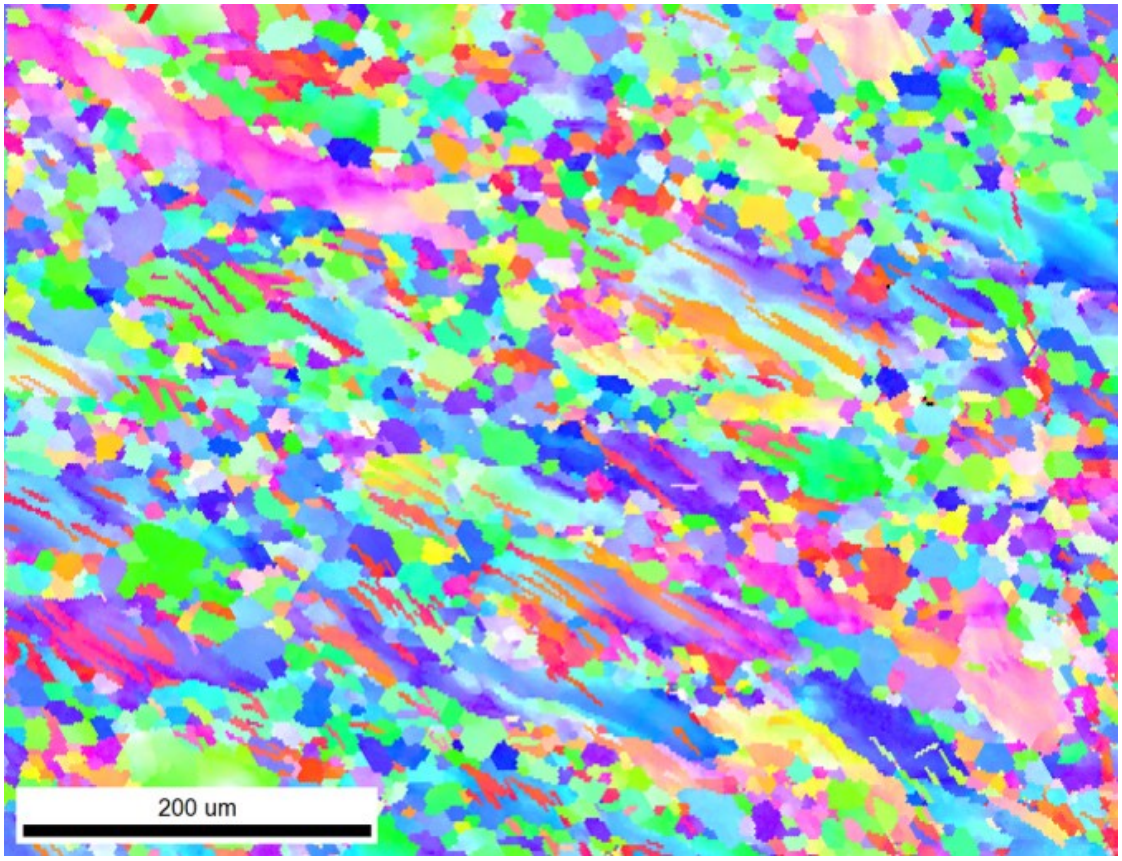

Figure 5.9: IPF map of pure Mg 4B_C extruded at 0.127 mm/s.

The results in this project offer the potential for new and potentially beneficial ECAE processing methods. Although twinning has been activated in refined microstructures under high strain rate loading before, the ability to induce twinning during ECAE invites the possibility to weaken texture (and thus enhance ductility in the final product) while still strengthening through grain size refinement [81]. In addition, grain size homogeneity can be improved with just modest increases to strain rates. Finally, the large twins after the first 0.127 mm/s pass can be used to create banded structures as seen after the second pass. This offers the potential to create bimodal banded structures through the careful selection of routes at low rates. Overall, this work expands

the capability of the ECAE process to produce engineered microstructures, a step towards achieving materials by design in magnesium alloys.

5.4 Conclusions

Pure magnesium was extruded by ECAE at three different rates, and the samples were characterized after each pass. The faster extrusion rates were found to refine the microstructure more rapidly than the slow rates, including orientations unfavorable for basal slip. Saturation of grain size refinement was attained early, and the average grain size was found to change very little with additional passes, with the exception of the 0.762 mm/s rate showing a slight reduction in average grain size compared to the other two rates. This reduction is attributed to a break-down of the largest grains. Evidence of multiple mechanisms of DRX was observed, including nucleation at low and intermediate angle boundaries. The 0.127 mm/s and 0.762 mm/s rates were found to generally have a greater twin volume fraction than the 0.381 mm/s rate.

6. *In-situ* Neutron Diffraction of Pure Mg during ECAE

6.1 Introduction

ECAE has attracted a great deal of attention for its capacity to produce ultrafine microstructures, even in materials that are difficult to work such as magnesium [104]. Schematics of ECAE have been shown previously in figure 1.3. The basic shape of the ECAE die is an L-shaped channel, and is unique among the author's known processing techniques in that applies only simple shear to the material. In the configuration shown in figure 1.3, and later in figure 6.1, the 90° interchannel angle applies approximately 1.12 strain per pass to the extrudate. The severe plastic strain imparted with each pass tends to activate dynamic recrystallization and improves mechanical properties primarily through grain refinement and the associated Hall-Petch strengthening.

As mentioned in previous chapters, the interactions that control DRX are highly intricate and identifying the active DRX mechanism during ECAE *ex situ* is challenging. The extrusion process imparts a large amount of strain during a single pass, and the initial recrystallized microstructure is altered and subsumed by further deformation or post-dynamic recrystallization. Furthermore, not only do the microstructures of intermediate stages of dDRX and cDRX look similar to one another, but some literature argues that both mechanisms of DRX are active simultaneously [48]. To address these issues, Liss et al. performed *in-situ* XRD during hot compression of Zr and titanium aluminide alloys [105,106]. Recovery and recrystallization behaviors were identified using qualitative analysis of the diffraction patterns. Specifically, as the temperature was ramped up with the load held constant, subgrains accumulate misorientation between themselves, creating a spread of orientations called a mosaic spread [106]. Upon recovery into dislocation-free

subgrains, some orientations disappear because they no longer meet the Ewald condition [106]. This results in a fragmentation of the mosaic spread. With increased temperatures, strains, and, as a result of the onset of necking, increased strain rates, Liss et al. observe dynamic recrystallization [106]. In terms of the definitions used in this work, this is a transition from cDRX to dDRX. Due to the heterogeneity of dDRX nucleation and the apparent randomness of the resulting reorientation, the apparent dDRX mechanism is characterized by "the sudden appearance and fluctuation of new orientations" [106]. In this work, Liss et al.'s observations are used as a roadmap to probe the recrystallization process during ECAE processing using neutron diffraction.

6.2 Experimental Methods

Towards this end, a miniaturized ECAE was designed and fabricated for *in situ* neutron diffraction studies, and can be seen in figure 6.1. The O1 steel die has a clamshell design for easy ejection of the sample following extrusion, and the sidewalls are sufficiently thin, so as to be neutron transparent. The design incorporates a number of elements that are known to improve the efficacy and uniformity of the extrusion process, including a sharp outer corner, dry powder lubrication, heating, and backpressure capabilities.

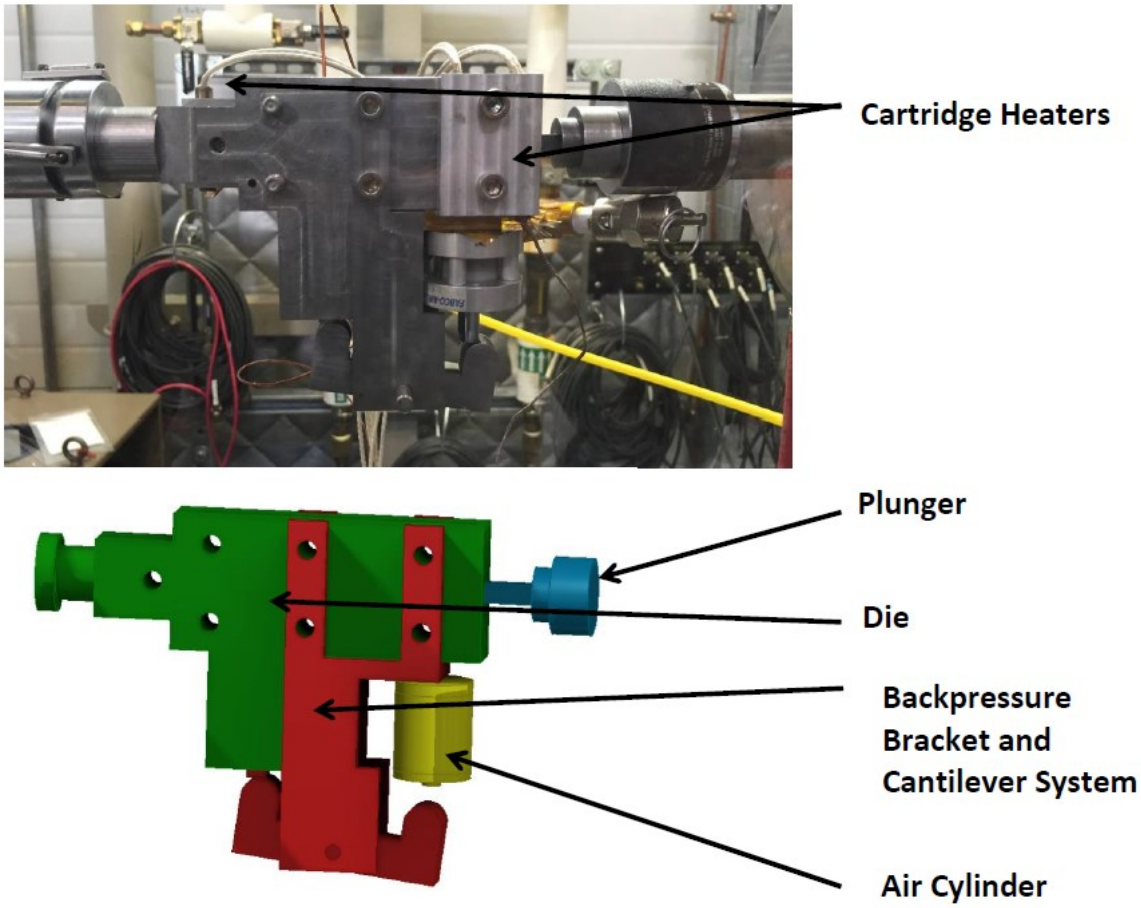

Figure 6.1: Picture and schematic of ECAE die in the VULCAN load frame with backpressure and heating systems attached.

This experiment required particular consideration regarding sample selection and processing conditions. Pure magnesium was used instead of AZ31B in order to eliminate the effect of precipitates on the material, which are known to encourage cDRX [46]. The sample was warm rolled to give it a very strong texture, and annealed, which strengthened the texture and removed residual stress. The resulting microstructure can be seen in figure 6.2. Given the work by Wu et al., a strain rate of 2×10^{-4} s^{-1} was estimated to be necessary to obtain good statistical diffraction results [107]. This strain rate can be used to approximate an extrusion rate using the equation provided by Segal where [29]:

$$\xi = \frac{(6-12)V\cos\theta}{a} \tag{3}$$

Here, ξ is the effective strain rate, V is the extrusion rate, a is the thickness of the sample, θ is half the angle between the channels, and the constant ranges from 6 to 12. From a rearrangement of the equation, an extrusion rate of 0.45 μm/s was desired. The processing temperature was determined by using the temperature-compensated strain rate given by the equation:

$$Z = \dot{\varepsilon}e^{Q/RT} \tag{4}$$

where $\dot{\varepsilon}$ is the strain rate, Q is the activation energy and assumed to be 92 kJ/mol, R is the gas constant, and T is the temperature [51,108]. If Z is calculated for our large ECAE experiments, the reduction in temperature required for this experiment can be determined using the above strain rate and holding Z constant. With this method, the required temperature was found to be 396 K. Additional temperatures were determined by varying Z by a factor of ten, while maintaining the same strain rate. The other temperatures were found to be 366 K and 432 K. However, during the experiment, the samples were found to shear localize and fail during extrusion under these conditions, possibly due to a reduction in backpressure compared to the large scale experiments. Increasing the extrusion rate to 0.71 μm/s was found to enable successful extrusion. Therefore, all samples were extruded at a rate of 0.71 μm/s. The samples are named based on their initial orientation and the extrusion temperature in degrees Centigrade: T93, E93, T123, E123, T159, and E159.

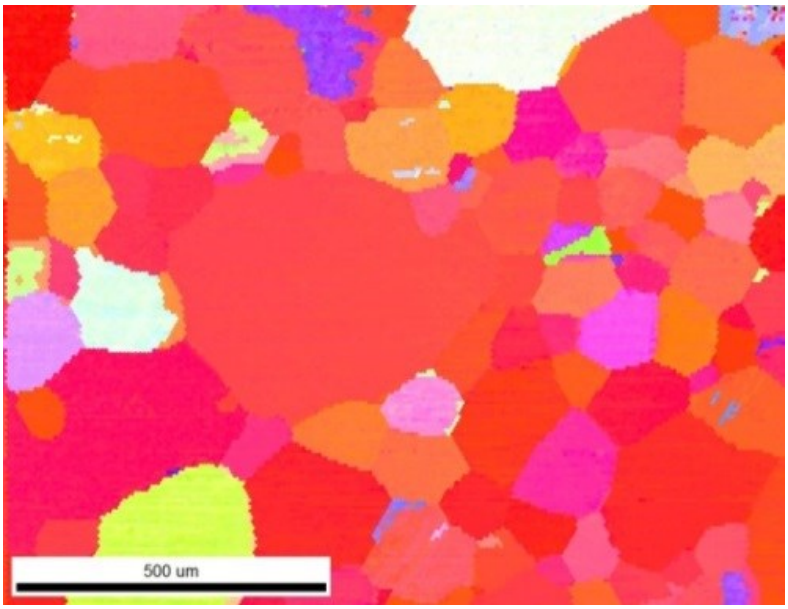

Figure 6.2: IPF map of rolled and annealed pure magnesium.

During deformation, the texture evolution is captured by positioning the neutron beam within the shear zone and collecting data over time. Post deformation, diffraction data is also collected from five regions in the sheared and unsheared zones to evaluate texture changes as a function of distance from the shear zone. These scans are referred to as dynamic and static scans, respectively. Schematics of the experiment can be seen in figure 6.3. The die is oriented at 45° with respect to the beam and two detectors, as seen in figure 6.3. This configuration allows collection of diffraction data from both the transverse and longitudinal directions of the die. Horizontal slits and radial collimators are used to restrict the beam to a volume measuring 2 mm × 2 mm × 3 mm.

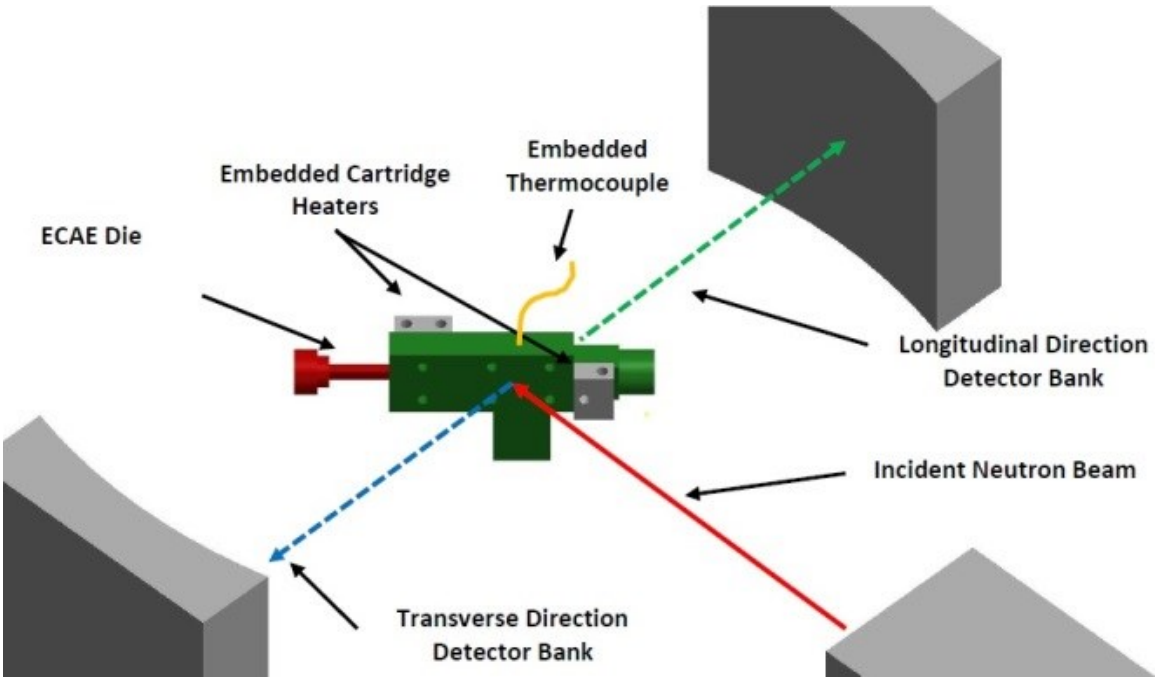

Figure 6.3: Schematic of the ECAE die in the neutron diffraction setup.

The VULCAN engineering diffractometer at the Spallation Neutron Source has several features that benefit this experiment. Most importantly, VULCAN is at a neutron source. X-rays are unable to penetrate the steel die, whereas neutrons can do so with ease, and hence, are a critical component of this experiment. Secondly, VULCAN is a time-of-flight diffractometer, allowing a larger d range than what could otherwise be acquired. The principle behind time-of-flight is that because every neutron collected is assigned a time stamp, the flight time of the neutrons, their distance travelled, their velocity, and hence, their wavelengths can be determined. With this information, the Bragg angle of different energy neutrons can be normalized. Finally, the VULCAN diffractometer allows for event-based data acquisition. Generally, during *in-situ* mechanical testing, the experiment must be interrupted to collect a sufficient number of neutrons. The sample must be held in either constant strain or constant stress modes. If the frame is held in

strain-control mode, there is stress relaxation, and if the frame is held in stress-control modes, the material tends to flow and plastically strain [107]. The event-based data acquisition solves this dilemma by allowing continuous loading during deformation, and binning the data into appropriate time steps during post processing, with the VDRIVE software [107]. Since directions like transverse can describe both the initial orientation of a sample and the diffraction vector of a detector in this work, a distinction between the two variants is necessary. Sample orientations will be referred to with a shortened form and a capitalized first letter (such as Trans), while the detector directions will use the full lowercase term (as in transverse).

6.3 Results and Discussion

6.3.1 Static Scans

Static scans were collected from five regions centered on the theoretical shear zone taken 1 mm apart along the primary axes of the intersecting channels. In other terms, the region called Preshear2 is located 2 mm prior to the shear zone along the longitudinal axis, Preshear1 is 1mm from the shear zone along the longitudinal axis, Postshear1 is located 1 mm after the shear zone along the extrusion axis, and Postshear2 is 2 mm from the shear zone along the extrusion axis. The diffraction patterns for the static scans of T123 are displayed in figure 6.4. Despite the sample initially possessing a strong basal texture in the Trans direction, all regions of the static scan have a strong basal peak in the longitudinal direction. The large basal peak can be interpreted as being the result of twinning since the reorientation of the matrix by extension twinning is approximately 87°. Moreover, the primary and secondary prismatic peaks in figure 6.4a are very weak.

Taken together, with the presence of a basal peak in figure 6.4b, this suggests that there are few, if any, twins that have rotated towards the extrusion direction. Although the intensities of the primary prismatic peak in figure 6.4a and the basal peak in figure 6.4b decrease approaching the shear zone, the peak intensities appear largely static after the shear zone in the transverse direction. In the longitudinal direction, the basal peak intensity decreases continuously. Lacking apparent redistribution of the volume fraction into other peaks, it suggests that grains oriented along the longitudinal direction are being deformed and rotate out of the basal diffraction condition into high order pyramidals that are not within the observable range of d-spacings.

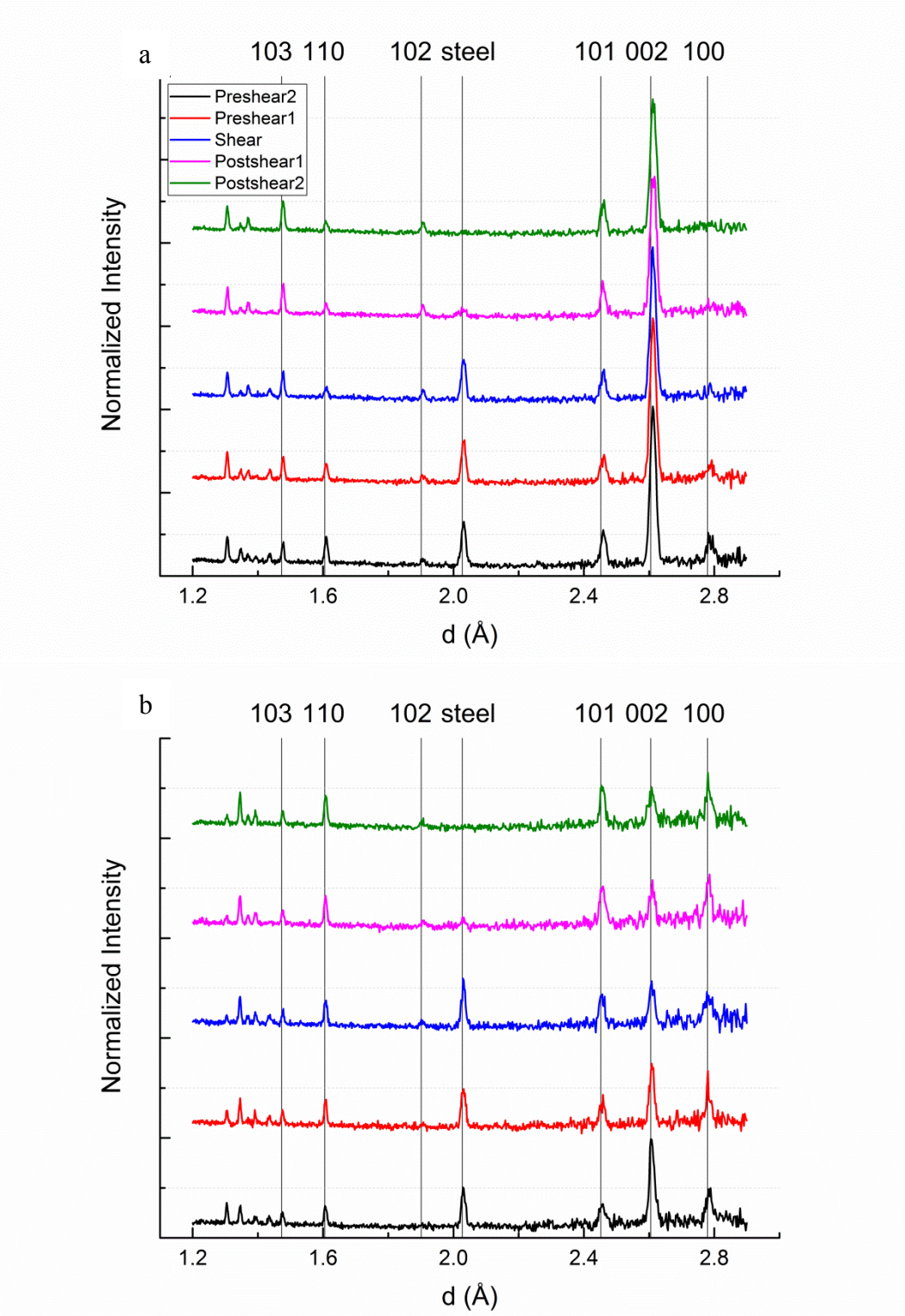

Figure 6.4: Static scans of T123 from (A) The longitudinal direction and (B) the transverse direction with the major peaks labelled.

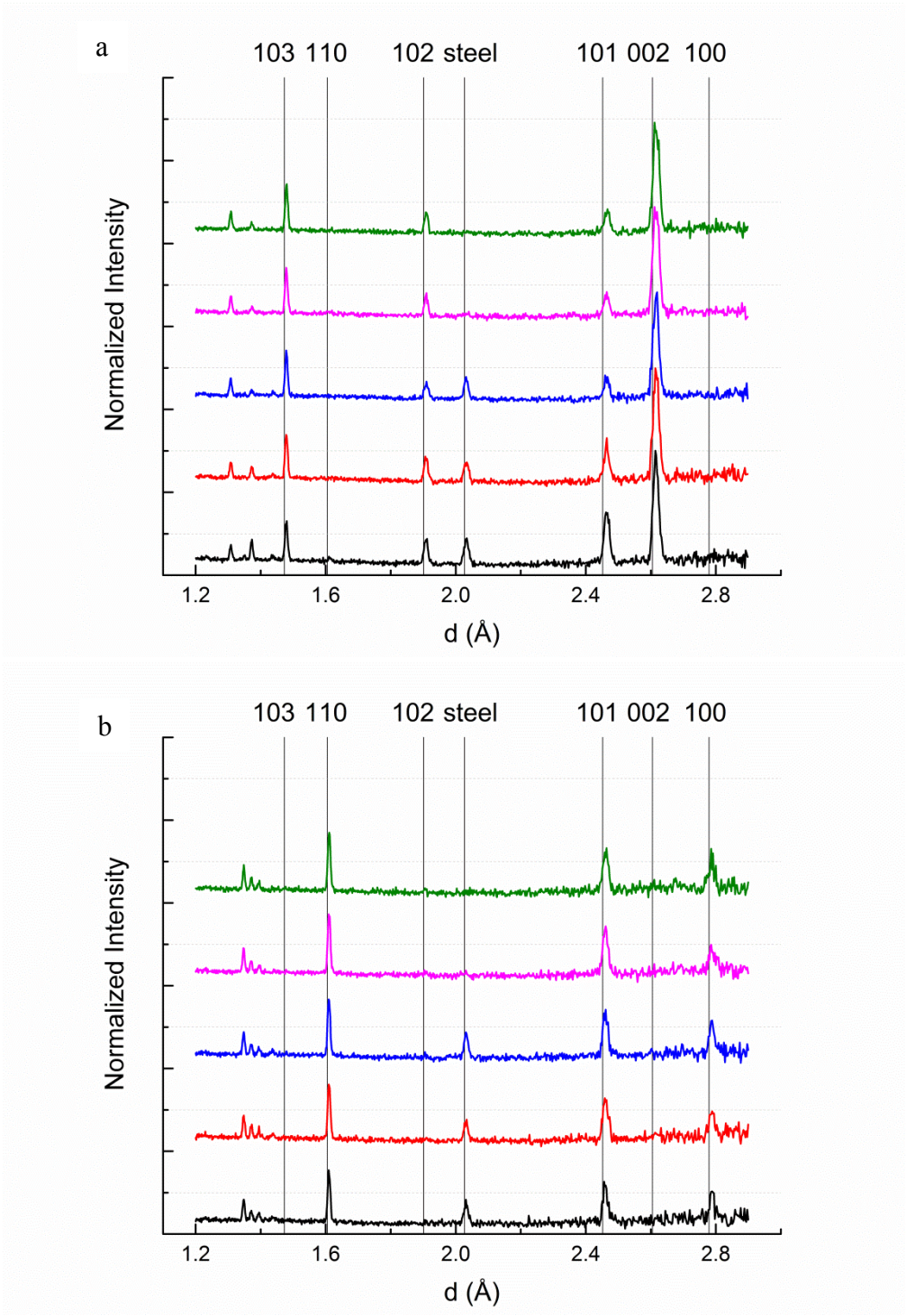

Figure 6.5: Static scans of E123 from (a) The longitudinal direction and (b) the transverse direction with the major peaks labelled.

Figure 6.5 contains the static scans for E123. Similar to T123, the longitudinal direction in E123 possesses a strong basal beak. The complete absence of a basal peak in figure 6.5b reinforces the argument that only variants that reorient into the longitudinal direction are activated. In addition, 6.5a lacks any evidence of prismatic peaks. Since the E123 sample is in a very soft orientation, the combined action of slip and twinning may have reoriented the basal poles of the entire volume out of the extrusion direction. The basal peak does not noticeably decrease in intensity as it does in the T123 sample. This may be due to some grains with the (101) orientation, having been rotated into even softer orientations due to the actions of slip and deformation away from the extrusion direction, taking up the deformation in place of the plastically harder grains with basal peaks in the longitudinal direction.

6.3.2 Dynamic Scans

Select diffraction patterns from the dynamic scans are displayed in figures 6.6 to 6.11. During the scan, the die was held static for 30 minutes to establish a baseline after which compression started. Diffraction patterns for the static hold, after 45 minutes of extrusion, and after 120 minutes of extrusion are shown. T93 in figure 6.6 is the exception because the neutron beam lost power after approximately 30 minutes of extrusion. In that instance, the pattern for 75 minutes of extrusion was used. As in the static scans, twinning into the longitudinal direction and a lack of twinning into other orientations is observed in every sample. For all samples, the basal peak is

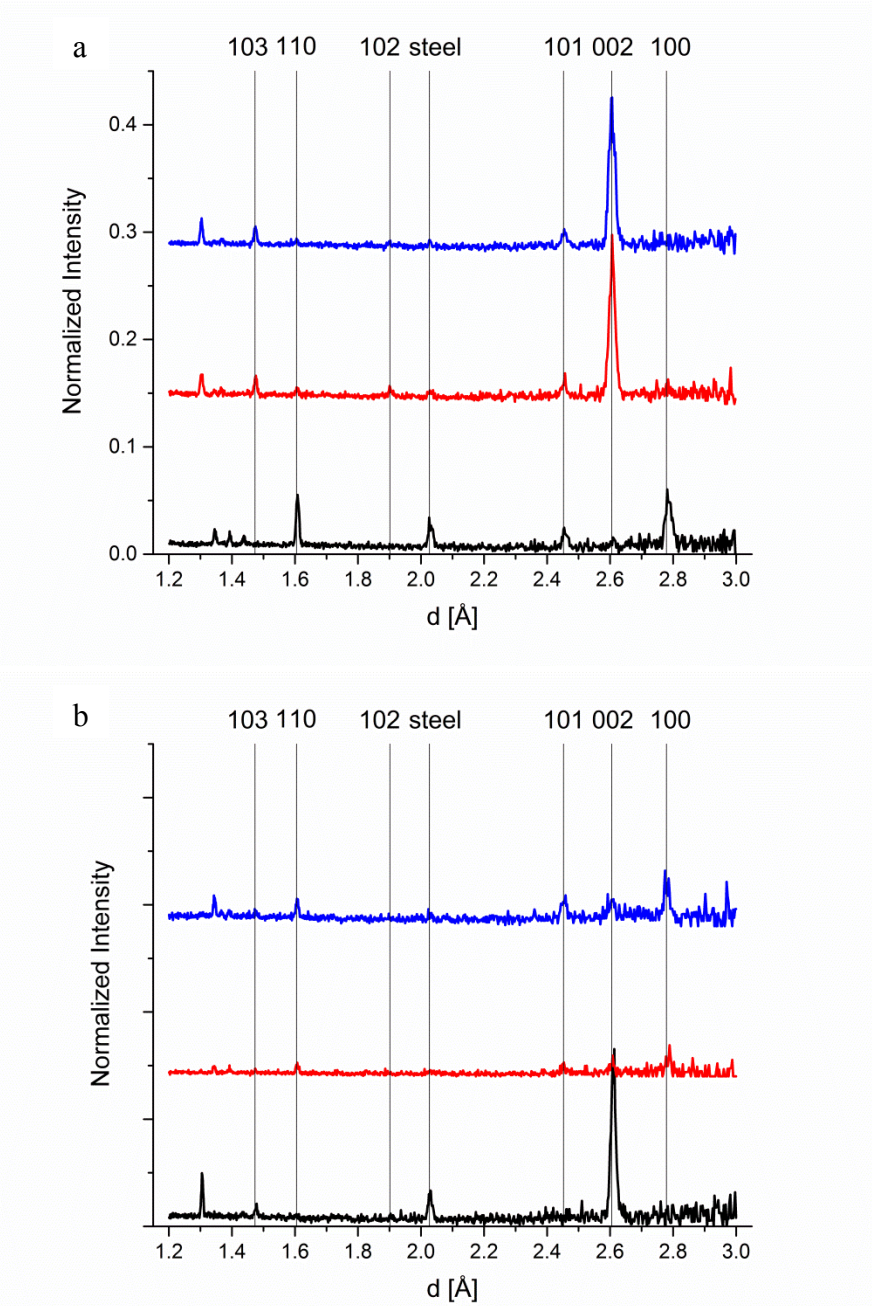

Figure 6.6: Dynamic scans of T93 from (a) The longitudinal direction and (b) the transverse direction with the major peaks labelled.

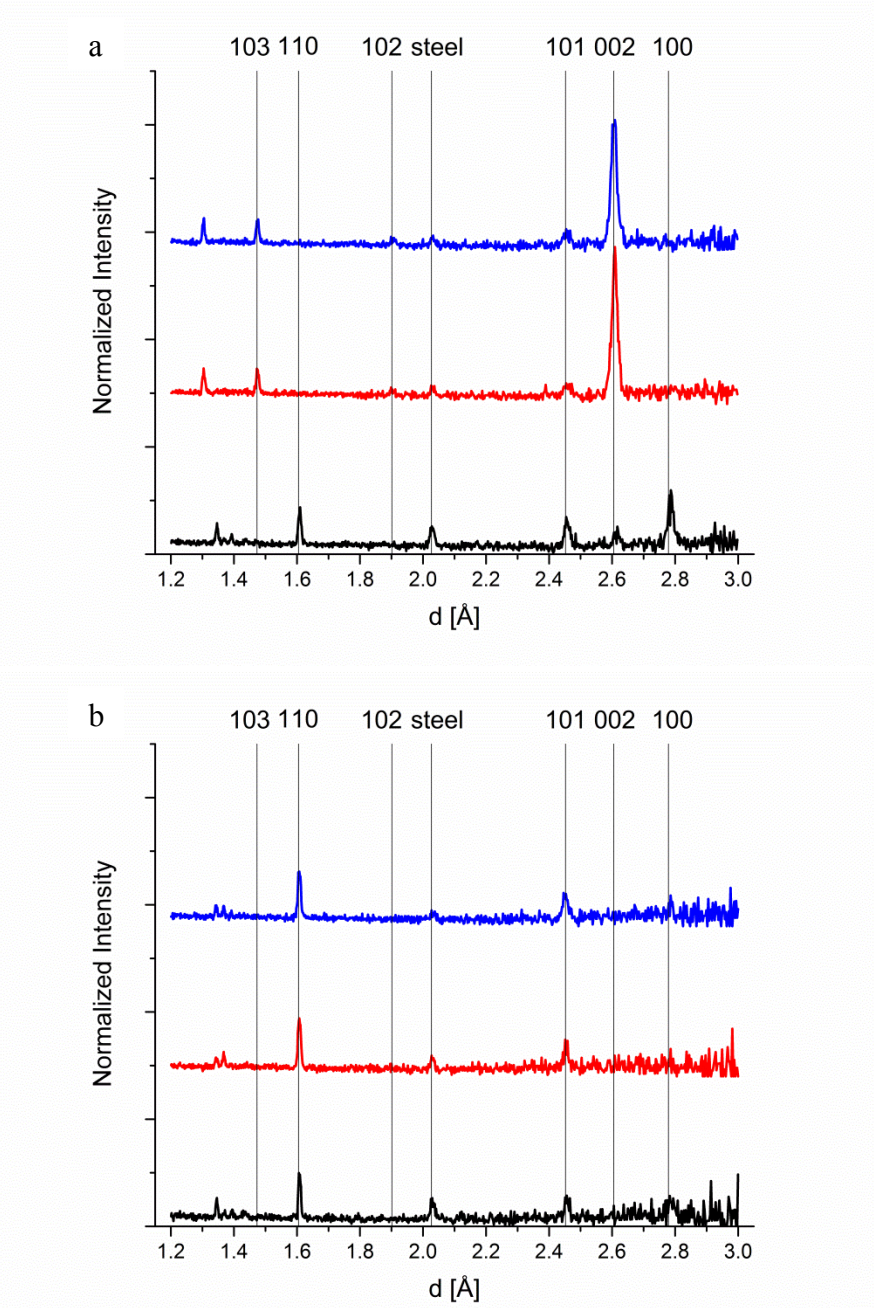

Figure 6.7: Dynamic scans of E93 from (a) The longitudinal direction and (b) the transverse direction with the major peaks labelled.

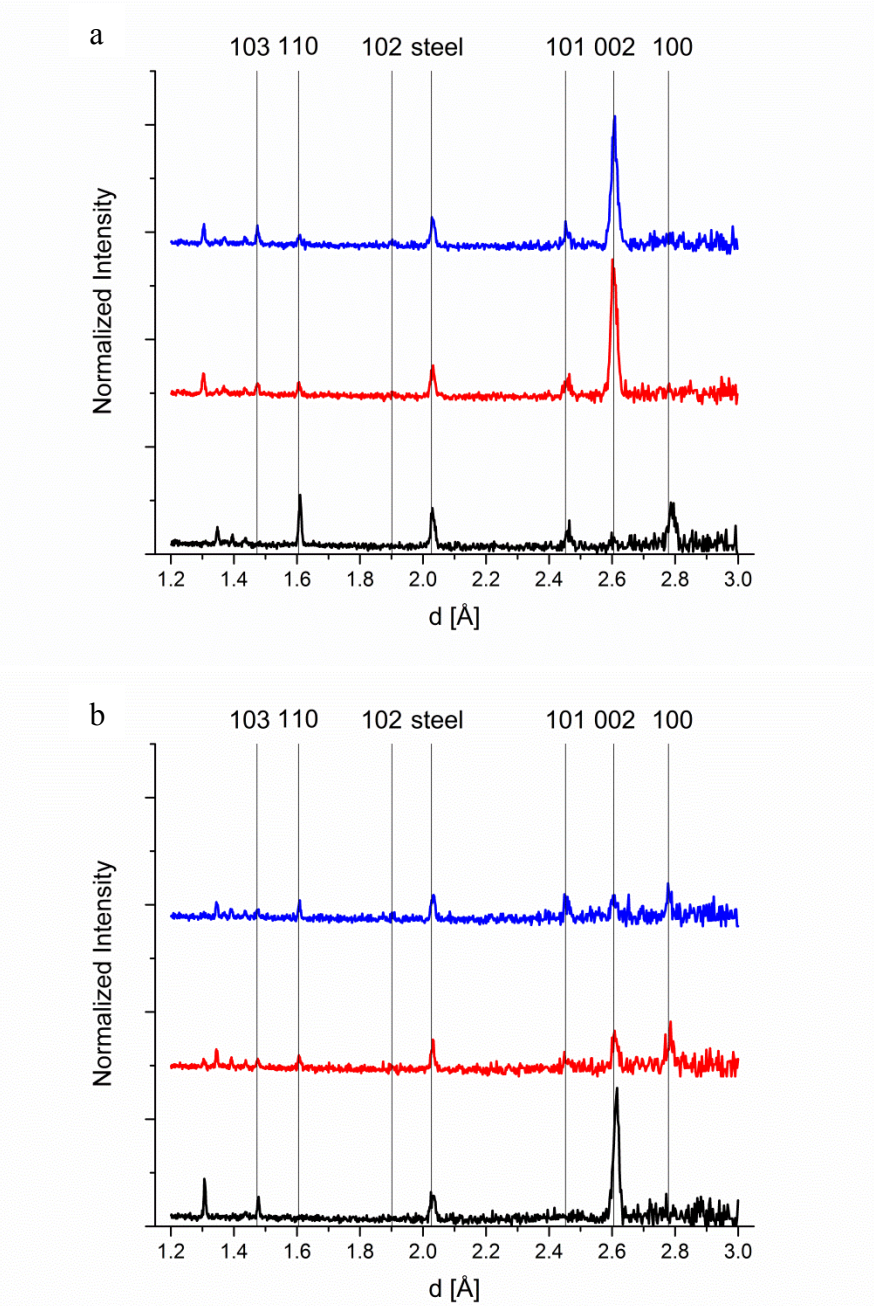

Figure 6.8: Dynamic scans of T123 from (a) The longitudinal direction and (b) the transverse direction with the major peaks labelled.

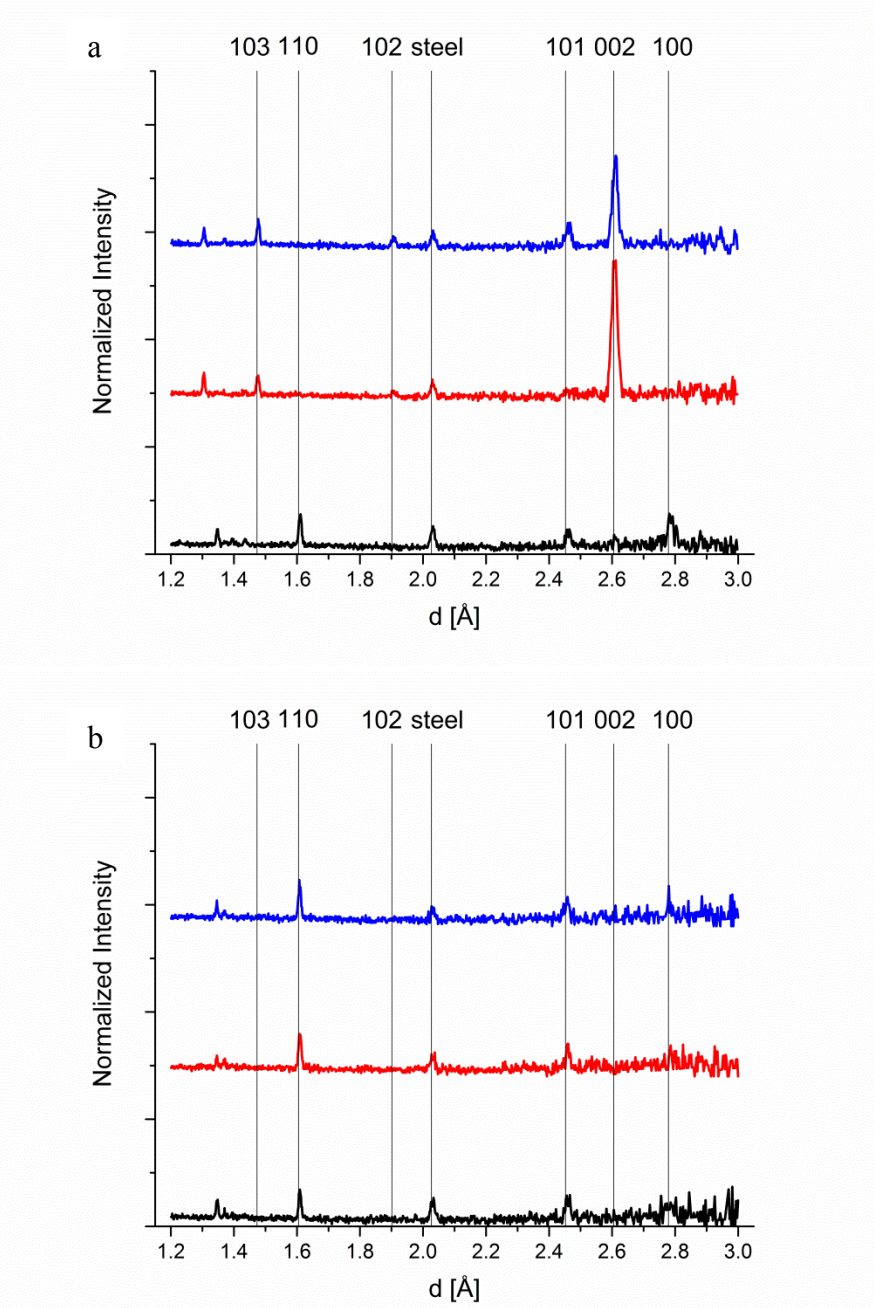

Figure 6.9: Dynamic scans of E123 from (a) The longitudinal direction and (b) the transverse direction with the major peaks labelled.

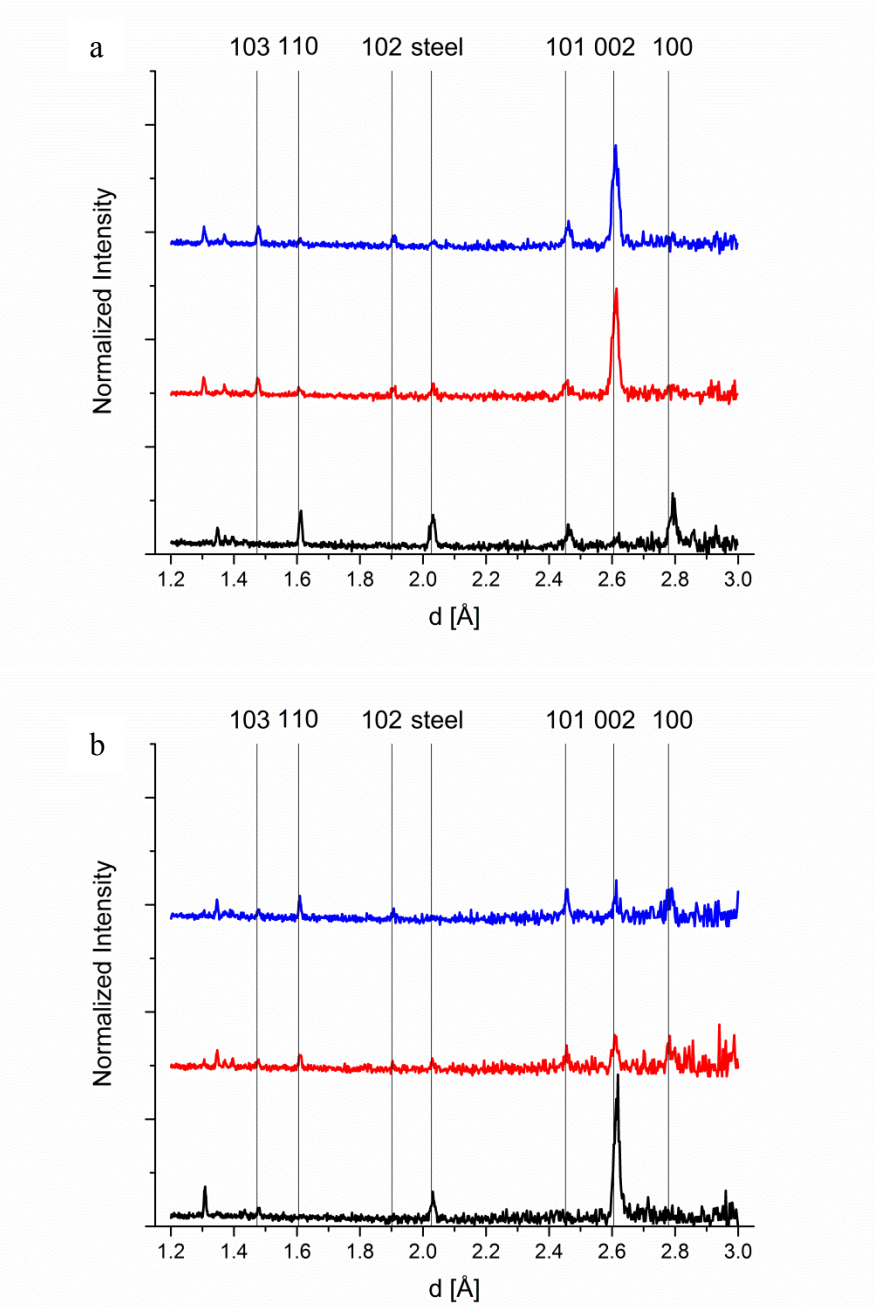

Figure 6.10: Dynamic scans of T159 from (a) The longitudinal direction and (b) the transverse direction with the major peaks labelled.

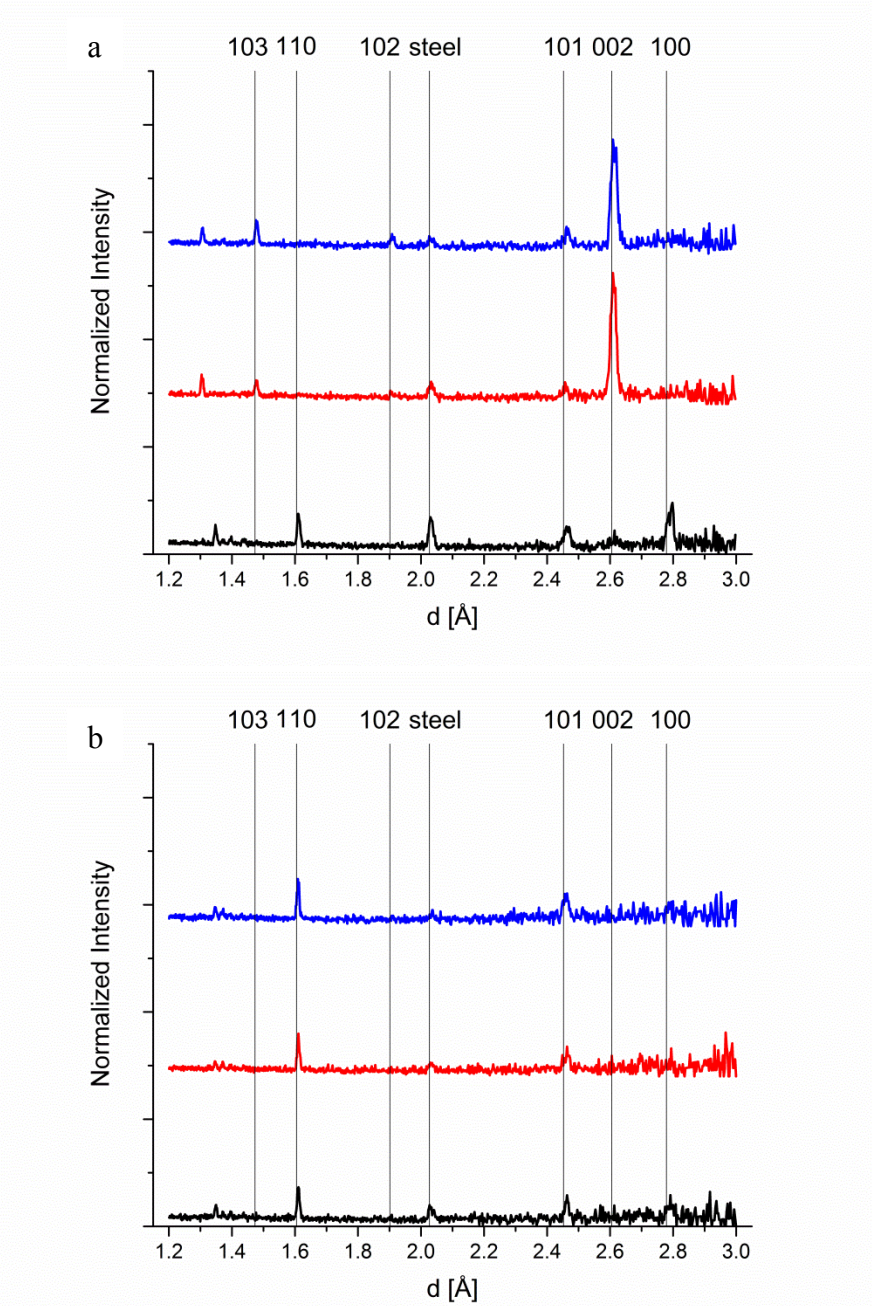

Figure 6.11: Dynamic scans of E159 from (a) The longitudinal direction and (b) the transverse direction with the major peaks labelled.

weaker after 120 minutes, and the Ex direction samples categorically demonstrate the greatest relative drop. It is not clear why the intensity of the basal peak after 120 minutes is abnormally low in the E123 sample. In addition, the basal peaks after 120 minutes in the Ex direction are generally less intense overall than in their Trans counterparts until 159°C. It appears that, despite their ostensibly similar orientation, grains in the Ex direction are easier to recrystallize than in the Trans direction. However, the rate at which the intensity of the basal peaks decreases with temperature is greater in the Trans samples, implying that temperature has a greater impact on the ease of recrystallization for that orientation.

The preferred prismatic orientation observed after twinning in the Trans direction is orientation dependent. Trans oriented samples typically display stronger primary prismatic peaks, while the Ex oriented samples possess stronger secondary prismatic peaks. This may be related to the orientation of the specific twin variant that is activated in each case. In the Trans samples, the (101) peak intensity in the transverse direction transitions from decreasing to increasing over time as temperature increases, although its maximum intensity remains fairly constant. In addition, the peak intensities of (102) and (103) remain relatively unchanged. This may suggest that at lower temperatures, rapid reorientation to high angles happens relatively quickly, but the orientation is fairly transient. At higher temperatures, the reorientation occurs more slowly. This implies more dDRX-like behavior at lower temperatures and more cDRX-like behavior at higher temperatures, which runs counter to the expected temperature dependence of these mechanisms [46].

6.3.3 Basal Peak Shape Evolution

Since the basal peak is the strongest peak and prone to the greatest change over time, it is worthwhile to investigate it further. The basal peaks in the longitudinal direction are plotted together in figure 6.12. The trends in peak intensity discussed in the previous section can clearly be observed in this figure. Note in figures 6.12b and d that the basal peaks at the same temperature are often fundamentally similar in shape, including the skew of the peak. The same secondary peak can even be seen in both T159 and E159. This indicates that once grains have twinned into the longitudinal direction, they deform similarly at the same temperatures, largely independent of the rest of the microstructure. The skewness of the peaks is likely due to an asymmetric distribution of either local strain or crystallite orientation in the basal orientation. With additional time, however, the skewed peaks become more symmetric in figure 6.12d. Accounting for thermal expansion of the lattice and hydrostatic compression from backpressure, most of the peaks are better distributed around the theoretical d-spacing. This is consistent with the effects of recrystallization which produces dislocation-free grains. The peak distribution and position of the 93°C samples remain relatively unchanged between 45 minutes (or 75 minutes in the case of T93) and 120 minutes. Since severe deformation is already occurring, this suggests that recrystallization is occurring faster at these lower temperatures and thus a more dDRX-like character. In contrast, the 159°C samples distinctly display a secondary peak in figure 6.12d, indicative of a secondary population of grains. This secondary population is distinct from the primary in terms of local stresses, or more likely, in orientation. Two distinct populations of grains in roughly similar orientations suggests a necklace-type microstructure due to cDRX. While dDRX

can also form a necklace-type microstructure in its intermediate stages, the heterogeneous nucleation of grains along the grain boundary would produce a range of grain sizes and thus maintain a broad, skewed peak. The separation of peaks here suggests relative homogeneity within the constituent grain populations, implying the action of cDRX. Again, evidence is observed for the operation of more dDRX-like behavior at lower temperatures and more cDRX-like behavior at higher temperatures, contrary to expected trends.

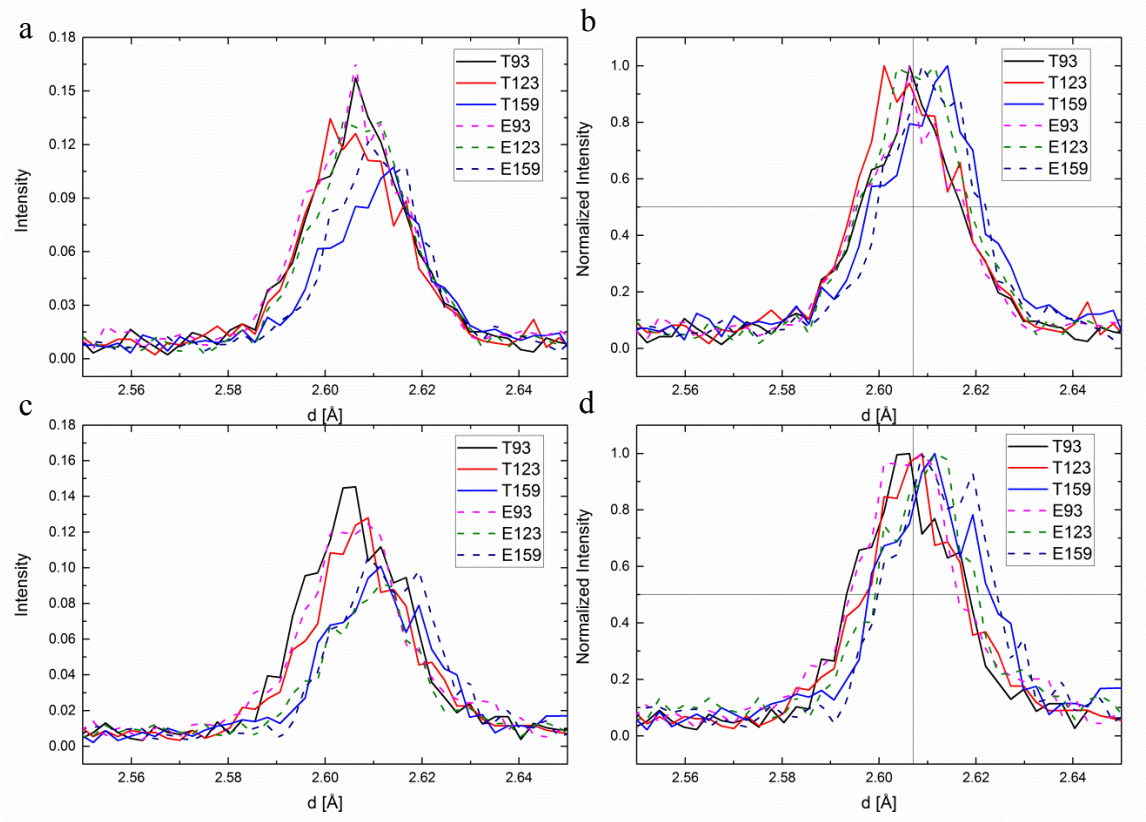

Figure 6.12: Basal peaks from the longitudinal direction plotted (a) after 45 minutes, (b) after 45 minutes and normalized, (c) after 120 minutes, and (d) after 120 minutes and normalized. Horizontal and vertical lines indicating half of the peak maximum and theoretical peak spacing are shown in (b) and (d).

6.3.4 Ex-situ Microstructural Analysis

The T123 sample was examined ex-situ with EBSD microstructure and texture are shown below in figure 6.13. Figure 6.13a shows a microstructure that is considerably recrystallized. The larger grains display both significant substructure formation and serration of the grain boundaries indicating, at least ex-situ, heavy competition between cDRX and dDRX. During *in-situ* diffraction, a strong basal peak was observed in every sample, but figure 6.13b shows almost no evidence of a basal texture in the longitudinal direction. It is clear that the sample has undergone further microstructural evolution after the shear zone. These results demonstrate that significant recrystallization can occur post-dynamically at roughly 0.43 homologous temperature, much less than the 0.57 homologous temperature used during typical ARL extrusions. It calls into question exactly how much dynamic versus post-dynamic recrystallization contributes to the microstructures that we generally consider to be byproducts of only ECAE deformation.

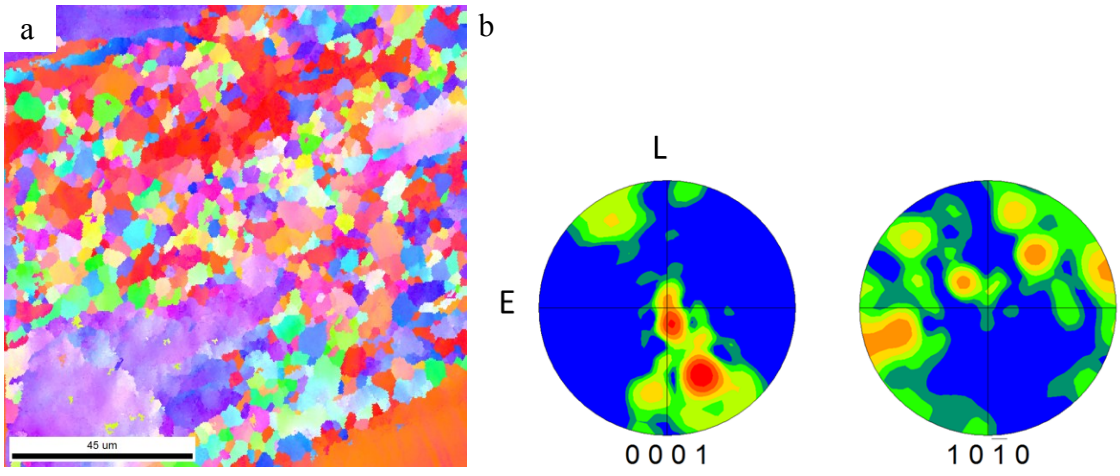

Figure 6.13: T123 microstructure ex-situ (a) IPF map and (b) pole figure

6.4 Conclusions

Samples of pure Mg were extruded by ECAE in two orientations at temperatures of 93, 123, and 159 °C during *in-situ* neutron diffraction. All samples demonstrated significant extension twinning that produced a large basal peak in the longitudinal direction. With both orientations reorienting into similar orientations early in deformation, the effects of the initial orientation on recrystallization were minimal. Samples processed at lower temperatures were found to exhibit behaviors indicating dDRX while those processed at higher temperatures exhibited more cDRX-like behavior.

6.5 Appendix: Steel Peaks During Extrusion

Almost every diffraction pattern displays steel peaks indicating that the diffraction volume frequently intersects the sidewalls. Multiple factors appear to play a role in this. In reviewing positional output of the load frame, there appears be a horizontal range of approximately 1-2 mm in the location of the alignment. The range is too much to be from variations in sample size, and points to an error in marker alignment. The accuracy of the marker is questionable as it was placed according to theoretical die dimensions. Furthermore, the marker had to be aligned with a camera crosshair, relying on consistency between operators. The table scans show that the steel peak typically disappears when moving along the extrusion axis, indicating first that the misalignment is largely systematic, and that it is the rear wall of the die that is being clipped. A few of the dynamic scans show an evolution in the steel peak intensity. In theory, the steel peak intensity should be consistent as the diffraction volume should not be moving within the channel. In actuality, the design of the load frame required both platens to move

simultaneously. To keep the die in place, the whole load frame was translated at half of the extrusion rate to keep the die in place. Slight mismatches between the applied extrusion rate and the offset rate are likely behind the small die shifts.

6.6 Appendix: Mini-ECAE Design Considerations and Schematics

For the experimental data to be useful for full-scale applications, the miniature ECAE system had to have all the capabilities of a normal sized system while subject to size and neutron transparency constraints. The VULCAN engineering diffractometer at the Spallation Neutron Source (SNS) at Oak Ridge National Lab (ORNL) was selected as preferred beam line for the experiment due to the ready access to a versatile load frame and heating capabilities. As an additional benefit, SNS was - and at the time of this writing, is - the most powerful neutron source in the world. Early in the process, sliding wall designs were rejected in favor of a simpler, clamshell design to improve system robustness and minimize points of failure. An asymmetric die design was created where one half included the bottom wall and a sidewall, and the other half had the remaining sidewalls. This design allowed the billet to be ejected simply by removing the die half with the bottom wall and continuing the extrusion. Several materials were considered for use as the constituent die material. Aluminum possessed poor mechanical properties at elevated temperatures, and its relative softness would increase the wear on the tool. Vanadium, frequently used in neutron diffraction, was rejected because the beam scientists cautioned that the incoherent scattering could be difficult to work with. At the suggestion of the ORNL beam scientists, steel was finally selected. Since thermal neutrons can penetrate about an inch of steel and the neutron beam would enter the die at

a 45° angle, the total thickness of the die was limited approximately 0.707 inches. As a consequence, a channel width of 0.25 inches was chosen.

Elevated temperature capability was achieved through the use of three cartridge heaters, attached close to either end of the die. Early versions of the die were plate shaped, but excess material was eventually removed in a "lean" design to reduce the thermal load on the cartridge heaters and improve die heating rates. A secondary benefit of the "lean" design was that it could be used with ORNL's induction heating coils as a backup heating source.

Designing a system to impose backpressure on the sample without vastly increasing the size of the ECAE system was difficult. A small air cylinder with a stroke length slightly longer than the maximum planned length of the sample was selected as the centerpiece of the backpressure system. The air cylinder was attached to a bracket on the inside corner of the die. Backpressure was applied to the sample via a cantilever and dummy billet attached to the backpressure. A pop safety valve was inserted between the air line and the cylinder to mediate the backpressure. If the backpressure increased above the rated value of the pop safety valve, air would leak out, ensuring a near constant backpressure. The final die schematics are shown below in figure 6.13, and the fully assembled system is shown in figure 6.3.

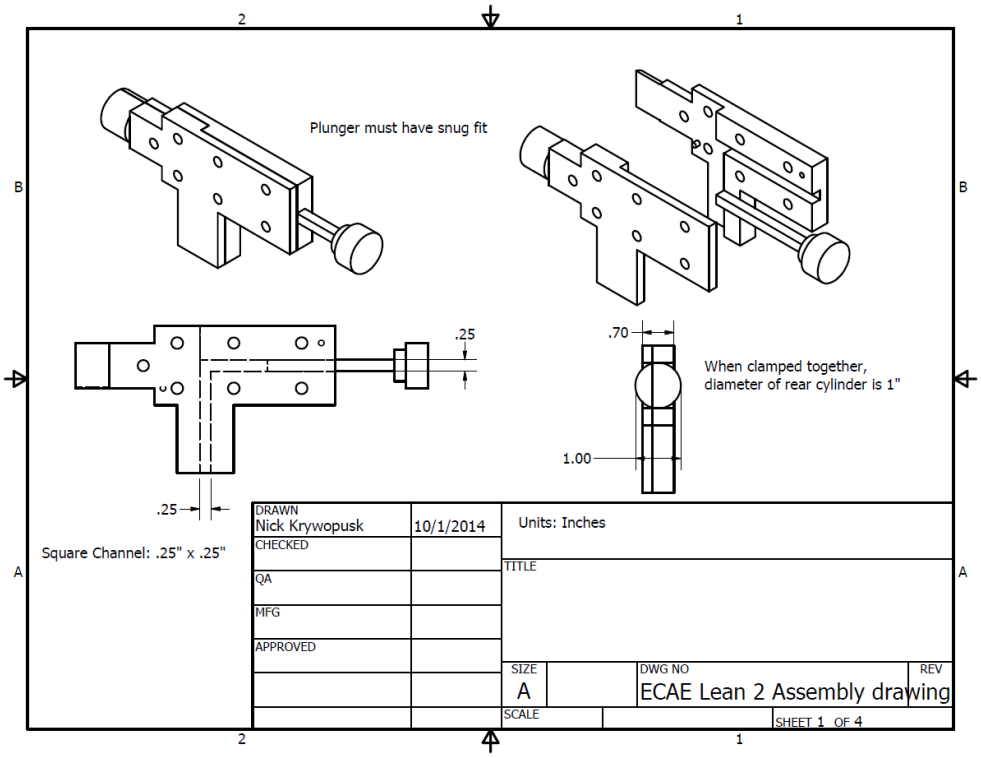
Plunger must have snug fit
.25
.25
Square Channel: .25" x .25"
.70
1.00
When clamped together, diameter of rear cylinder is 1"
DRAWN Nick Krywopusk 10/1/2014
CHECKED
QA
MFG
APPROVED
Units: Inches
TITLE
SIZE A
DWG NO ECAE Lean 2 Assembly drawing
REV
SCALE
SHEET 1 OF 4

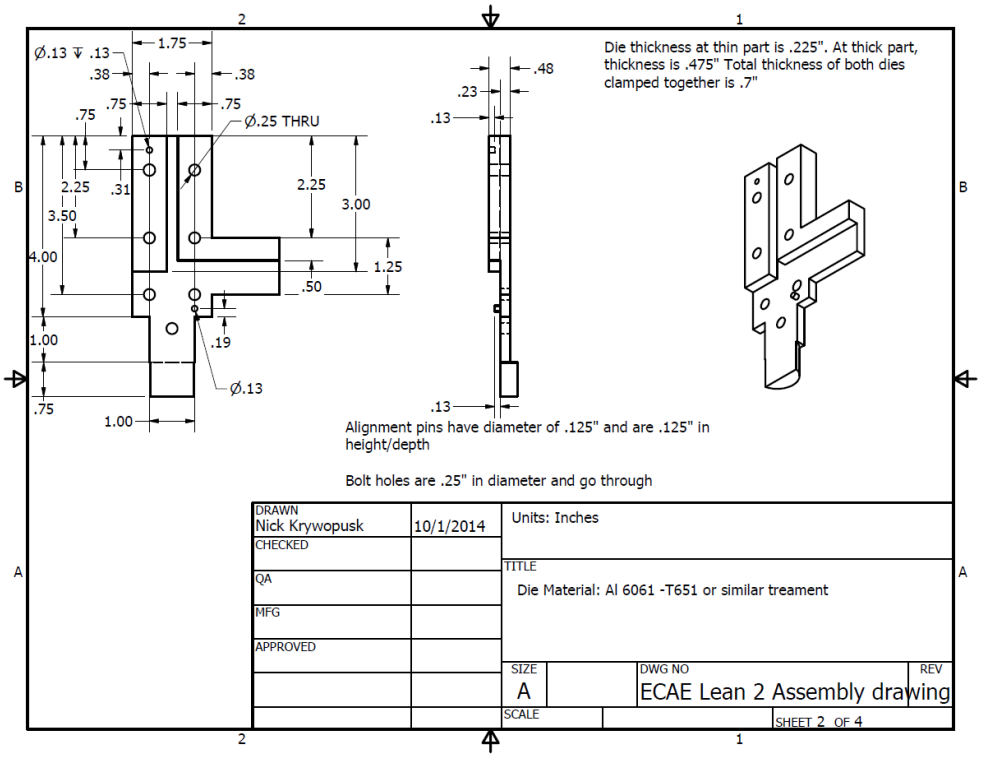
Ø.13 .13
1.75
.38
.38
.75
.75
.75
Ø.25 THRU
2.25
.31
2.25
3.00
3.50
4.00
1.25
.50
1.00
.19
Ø.13
.75
1.00
.48
.23
.13
.13
Die thickness at thin part is .225". At thick part, thickness is .475" Total thickness of both dies clamped together is .7"
Alignment pins have diameter of .125" and are .125" in height/depth
Bolt holes are .25" in diameter and go through
DRAWN Nick Krywopusk 10/1/2014
CHECKED
QA
MFG
APPROVED
Units: Inches
TITLE
Die Material: Al 6061 -T651 or similar treament
SIZE A
DWG NO ECAE Lean 2 Assembly drawing
REV
SCALE
SHEET 2 OF 4

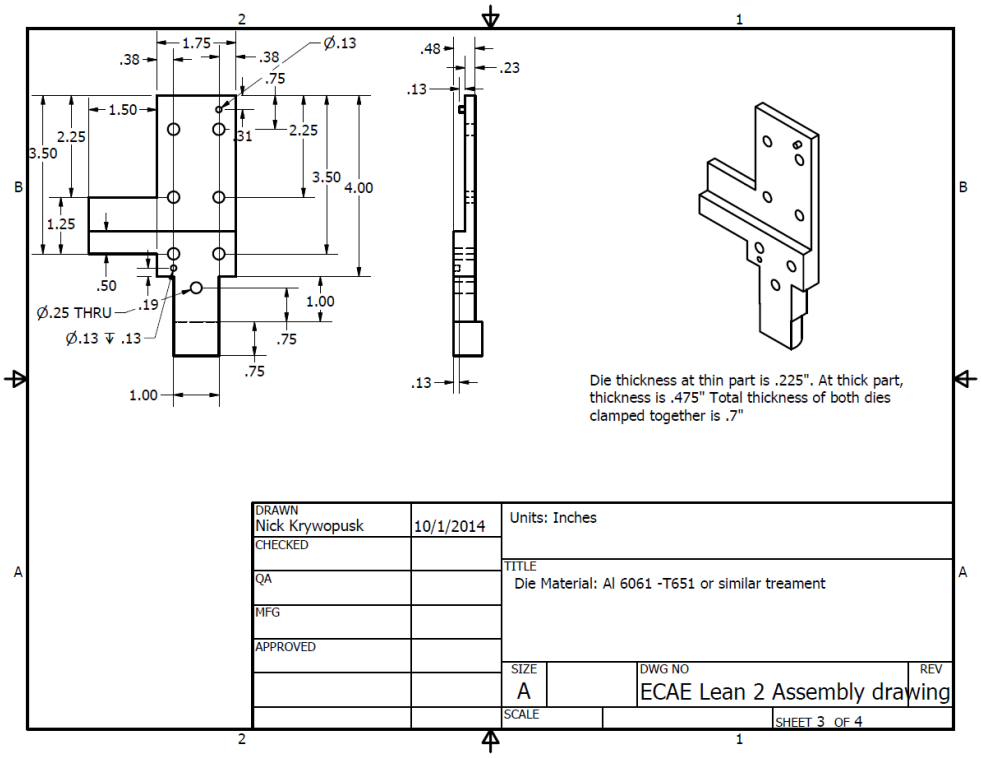

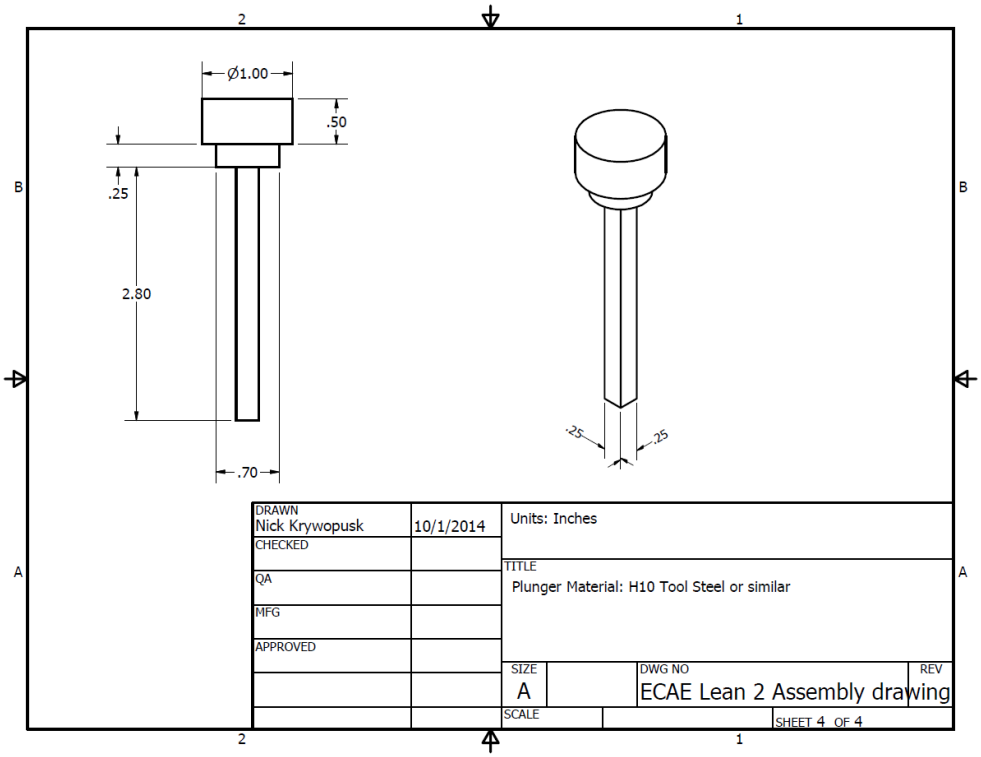

Figure 6.14: Drawings of clam-shell ECAE die.

6.7 Appendix: Neutron Diffraction Data Analysis

The majority of data processing in this work was performed using VULCAN's in-house analysis program, VDRIVE. VDRIVE handles data reduction, simple visualization, and basic data analysis tasks.

Since VULCAN is a time-of-flight diffractometer, which provides a time stamp for every neutron detected, and event-based data acquisition, where data is collected continuously, the diffraction data must first be partitioned into bins of time. To ensure good statistics, 15 minute bins were used, although no obvious difference in data quality was noticed with 8 minute bins. The binning function (VDRIVECHOP) also allows for the simultaneous normalization over the 30 Hz Vanadium profile and proton charge. Without Vanadium profile normalization, the data appears to have a large incoherent background, which is the beam power distribution. A Vanadium profile that was collected using the same chopper speed as the experiment is necessary for accurate normalization. The resulting data files are ready for visualization or further analysis. A sample input for VDRIVECHOP would be:

IPTS=16928 (The experiment's ID number)
RUNS=110721 (The run ID number)
dbin=900 (bin size in seconds)
RUNV=110592 (Normalize data over a Vanadium profile with the proper chopper speed)
PCSENV=1 (Normalize over proton charge)
bin=1 (bin the data to a file)
vout=1 (print the data to a text file that can be used outside of VDRIVE)

The command "VDRIVESPF" performs single peak fitting on data using a text input file that defines the detector number, the name of the peak, the number of peaks, the peak d-spacing, and the search range for the peak (in d-spacing). The output file provides integrated breadth, peak positions, strain, estimated errors for said values, and plots of

raw and fitted data. The user has very little control over how VDRIVE performs the single peak fitting, and as a result, it is somewhat of a black box. Particularly when the signal to noise ratio is very low, the program fits the data very poorly. The output data should always be checked against the quality of fit in the plots.

7. Conclusions and Future Work

7.1 Conclusions

In chapter 1, a figure was presented that outlined the state of knowledge for ECAE processing-structure-properties relationships. In figure 7.1, that figure is modified to reflect the contributions made in this work. While neither figure is exhaustive, they serve to show where this work has made progress and filled in some gaps.

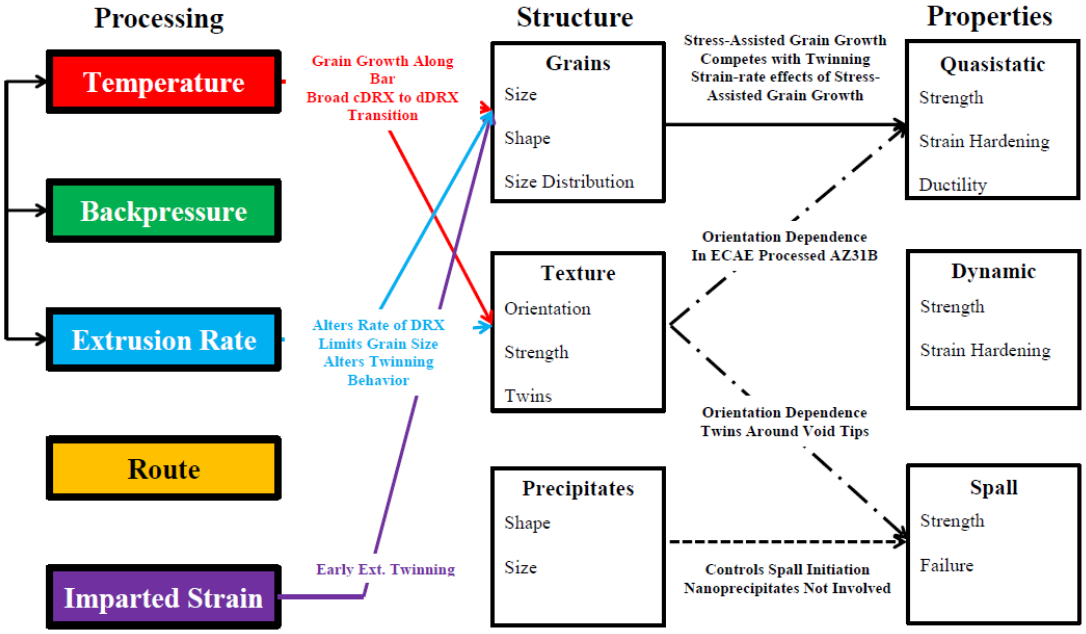

Figure 7.1: Contributions in this work to ECAE processing – microstructure – properties relationship with a brief description of each finding.

In Chapter 2, it was shown that the microstructures of ECAE processed materials possessed rather wide distributions, even though the average grain size for each material was highly consistent throughout the billet. If narrower distributions are desirable, the strain-rate must be increased to limit the upper size of the grains.

Examination of the ECAE-processed AZ31B microstructures after deformation at quasi-static rates showed significant amounts of abnormal grain growth, which is a softening mechanism. While it is still unclear precisely which factors caused the abnormal grain growth to occur in this context, from an alloy design perspective, the addition of more solute or finely distributed precipitates would likely help pin the grain boundaries and minimize the softening effect.

Solutes or finely distributed precipitates were suggested because large precipitates, such as the large Mn-Al "stringer" precipitates that exist in AZ31B perform a critical role in the nucleation and early growth of voids during spall. The primary lesson of this chapter is to avoid large insoluble precipitates to improve spall strength.

In Chapter 5, the fast strain-rates were found to break down plastically hard orientations better resulting in an overall increase in area fraction recrystallized compared to the slower rates. This result implies that extrusions can avoid shear localization by increasing strain-rate. It is clear that this trend cannot extend ad infinitum, but the precise limits of this effect are not yet known.

The findings in Chapter 6 are that, at the temperatures and strain-rates tested, extension twinning reorients a large fraction of the microstructure towards the Longitudinal direction, but this texture is eliminated by post-dynamic processes and does not present immediate benefits to extrusion capabilities. However, it does hold promise. Given that post-dynamic processes have the potential to play a major role in microstructural evolution after ECAE, it suggests that ECAE really has two sets of (likely interconnected) knobs: those that control the microstructure directly created by ECAE and those that impact post-dynamic processes.

For most HCP materials, ECAE produces strong fiber textures. Traditionally, the texture has been weakened by extruding at higher temperatures to favor the texture randomization associated with dDRX. This generally comes at the cost of grain size. However, it was found in Chapter 5 that either increasing or decreasing the strain-rate from the intermediate value increased the fraction of twins in the material, and significantly reduced the texture. By controlling texture strength through strain-rate, grain size and the associated Hall-Petch strength are not impacted.

7.2 Future Work

In the quest for materials by design, a number of new avenues of exploration and new gaps in understanding have been revealed by this work. Some of these are examined and experiments briefly proposed below.

The results of the highest strain-rate compression testing in Chapter 3 suggests that in compression, magnesium may transition from a largely slip mediated regime to a possibly stress-assisted grain growth mediated regime. However, to my current knowledge, Kannan et al have not observed apparent stress-assisted grain growth at Kolsky bar rates starting around 10^3 s^{-1}. Thus, if such a regime of stress-assisted grain growth mediated regime does exist, it does so in the traditionally difficult to achieve range of strain-rates: 10^0 to 10^3 s^{-1}. In this case, the holder designed for dynamic TEM may be well suited to evaluate the microstructural evolution within that range. Sample preparation is not made any more difficult since the crystalline axes are already not aligned with any of the sample orthogonal axes. Images forces due to the sample surfaces

in the TEM specimen geometry are not an issue in this instance, being likely to enhance activation of stress-assisted grain growth [85].

The effects of strain-rate on volume fraction recrystallized, grain size distribution, twin enhancement, and texture modification presents a number of new opportunities for ECAE process route design. The effect on the rate of recrystallization is to widen the magnesium processing window and has already been discussed in previous sections. One of the notable shortcomings of the ECAE process is the relative difficulty in creating textures aside from a basal fiber. The enhancement of large twins at low extrusion rates creates the possibility of generating bimodal microstructures through careful route design. Such a route would require rotations and temperatures where the twinned and untwinned regions do not deform by the same mechanism (ex. Prismatic and basal slip or basal slip and extension twinning). Subsequent passes would require similar considerations. Such bimodal structures would allow ECAE to generate textures that more closely mimic other processes that produce textures with biaxial qualities (such as traditional extrusion with its prismatic fiber texture). The enhanced twinning at high strain-rates allows for an easy method by which to weaken textures and magnesium's inherent anisotropy. The addition of a pass, or replacement of a final pass with a higher extrusion rate variant is a relatively painless way to improve microstructural homogeneity and weaken the texture.

The difference between the texture observed during *in-situ* neutron diffraction and the texture observed from *ex-situ* EBSD highlights the need to understand post-dynamic recrystallization and its interactions with the processing parameters and processing texture. An experiment that is well within our current capabilities is to essentially repeat

the neutron diffraction experiment. Instead of the dynamic scan remaining in the same location, the load frame can be translated vertically to follow a volume of grains as the microstructure evolves after the shear zone.

The most glaring limitation of this work is that it focused only on pure Mg and AZ31B. The isolated effects of solutes and a single phase of precipitates on microstructural evolution have been entirely overlooked. Pure Mg has almost no inclusions to study, while AZ31B, being a commercial alloy, has a number of secondary phases, making it difficult to extricate their individual effects. It is probable that with the addition of grain refiners, texture modification by encouraging twins at high strain-rate becomes much difficult or impossible. A follow-up study should remedy this issue by studying the effects of various solutes and precipitates on microstructural evolution during processing, quasi-static deformation, and dynamic deformation.

The second limitation of this study lies in which factors were evaluated. Grain size, texture, and to a lesser extent, grain size distribution were the results most frequently reported in this work. To a large extent, factors such as fraction of high angle boundaries and grain boundary character have been overlooked. As a result, this work has contributed little to the understanding of grain boundary engineering in magnesium, which has effects on both mechanical and corrosion properties. To a certain extent, a large amount of data has already been collected via EBSD which could be mined for data related to the grain boundaries.

8. References

[1] B.L. Mordike, T. Ebert, Magnesium Properties - applications - potential, Mater. Sci. Eng. A. 302 (2001) 37–45. doi:10.1016/S0921-5093(00)01351-4.

[2] T.L. Jones, R.D. DeLorme, M.S. Burkins, W.A. Gooch, Ballistic evaluation of magnesium alloy AZ31B, DTIC Document, 2007.

[3] M.H. Yoo, Slip, Twinning, and Fracture in Hexagonal Close-Packed Metals, Met. Mater. Trans. A. 12A (1981) 409–418.

[4] G.I. Taylor, Plastic strain in metals, Twenty-Eighth May Lect. to Inst. Met. (1938) 307–325. doi:not found.

[5] S.R. Agnew, Ö. Duygulu, Plastic anisotropy and the role of non-basal slip in magnesium alloy AZ31B, Int. J. Plast. 21 (2005) 1161–1193. doi:10.1016/j.ijplas.2004.05.018.

[6] M.H. Yoo, J.R. Morris, K.M. Ho, S.R. Agnew, Nonbasal deformation modes of HCP metals and alloys: Role of dislocation source and mobility, Metall. Mater. Trans. A. 33 (2002) 813–822. doi:10.1007/s11661-002-1013-5.

[7] P.G. Partridge, The crystallography and deformation modes of hexagonal close-packed metals, Metall. Rev. 12 (1967) 169–194. doi:10.1179/mtlr.1967.12.1.169.

[8] W.B. Hutchinson, M.R. Barnett, Effective values of critical resolved shear stress for slip in polycrystalline magnesium and other hcp metals, Scr. Mater. 63 (2010) 737–740. doi:10.1016/j.scriptamat.2010.05.047.

[9] M.R. Barnett, Twinning and the ductility of magnesium alloys, Mater. Sci. Eng. A. 464 (2007) 1–7. doi:10.1016/j.msea.2006.12.037.

[10] J.W. Christian, S. Mahajan, Deformation twinning, Prog. Mater. Sci. 39 (1995) 1–157. doi:10.1016/0079-6425(94)00007-7.

[11] M.R. Barnett, Twinning and the ductility of magnesium alloys. Part II. “Contraction” twins, Mater. Sci. Eng. A. 464 (2007) 8–16. doi:10.1016/j.msea.2007.02.109.

[12] K. Kubota, M. Mabuchi, K. Higashi, Processing and mechanical properties of fine-grained magnesium alloys, J. Mater. Sci. 34 (1999) 2255–2262. doi:10.1023/A:1004561205627.

[13] A. Yamashita, Z. Horita, T.G. Langdon, Improving the mechanical properties of magnesium and a magnesium alloy through severe plastic deformation, 300 (2001) 142–147.

[14] M.T. Pérez-Prado, J. a. del Valle, J.M. Contreras, O. a. Ruano, Microstructural evolution during large strain hot rolling of an AM60 Mg alloy, Scr. Mater. 50 (2004) 661–665. doi:10.1016/j.scriptamat.2003.11.014.

[15] M.Y. Zhan, Y.Y. Li, W.P. Chen, W.D. Chen, Microstructure and mechanical properties of Mg-Al-Zn alloy sheets severely deformed by accumulative roll-bonding, J. Mater. Sci. 42 (2007) 9256–9261. doi:10.1007/s10853-007-1885-2.

[16] Y.J. Chen, Q.D. Wang, H.J. Roven, M. Karlsen, Y.D. Yu, M.P. Liu, J. Hjelen, Microstructure evolution in magnesium alloy AZ31 during cyclic extrusion compression, J. Alloys Compd. 462 (2008) 192–200. doi:10.1016/j.jallcom.2007.07.116.

[17] T. Peng, Q. Wang, J. Lin, M. Liu, H.J. Roven, Microstructure and enhanced mechanical properties of an Mg-10Gd-2Y-0.5Zr alloy processed by cyclic extrusion and compression, Mater. Sci. Eng. A. 528 (2011) 1143–1148. doi:10.1016/j.msea.2010.09.097.

[18] Q. Wang, Y. Chen, M. Liu, J. Lin, H.J. Roven, Microstructure evolution of AZ series magnesium alloys during cyclic extrusion compression, Mater. Sci. Eng. A. 527 (2010) 2265–2273. doi:10.1016/j.msea.2009.11.065.

[19] J. Xing, H. Soda, X. Yang, H. Miura, T. Sakai, Ultra-Fine Grain Development in an AZ31 Magnesium Alloy during Multi-Directional Forging under Decreasing Temperature Conditions, Mater. Trans. 46 (2005) 1646–1650. doi:10.2320/matertrans.46.1646.

[20] H. Miura, G. Yu, X. Yang, Multi-directional forging of AZ61Mg alloy under decreasing

temperature conditions and improvement of its mechanical properties, Mater. Sci. Eng. A. 528 (2011) 6981–6992. doi:10.1016/j.msea.2011.05.050.
[21] P. Serre, R.B. Figueiredo, N. Gao, T.G. Langdon, Influence of strain rate on the characteristics of a magnesium alloy processed by high-pressure torsion, Mater. Sci. Eng. A. 528 (2011) 3601–3608. doi:10.1016/j.msea.2011.01.066.
[22] R.B. Figueiredo, T.G. Langdon, Development of structural heterogeneities in a magnesium alloy processed by high-pressure torsion, Mater. Sci. Eng. A. 528 (2011) 4500–4506. doi:10.1016/j.msea.2011.02.048.
[23] K. Edalati, A. Yamamoto, Z. Horita, T. Ishihara, High-pressure torsion of pure magnesium: Evolution of mechanical properties, microstructures and hydrogen storage capacity with equivalent strain, Scr. Mater. 64 (2011) 880–883. doi:10.1016/j.scriptamat.2011.01.023.
[24] M. Furukawa, Z. Horita, M. Nemoto, T.G. Langdon, Processing of metals by equal-channel, Significance. 6 (2001) 2835–2843. http://www.springerlink.com/content/h66m178160157q73/.
[25] Y. Estrin, A. Vinogradov, Extreme grain refinement by severe plastic deformation: A wealth of challenging science, Acta Mater. 61 (2013) 782–817. doi:10.1016/j.actamat.2012.10.038.
[26] R.B. Figueiredo, T.G. Langdon, Record superplastic ductility in a magnesium alloy processed by equal-channel angular pressing, Adv. Eng. Mater. 10 (2008) 37–40. doi:10.1002/adem.200700315.
[27] S.X. Ding, W.T. Lee, C.P. Chang, L.W. Chang, P.W. Kao, Improvement of strength of magnesium alloy processed by equal channel angular extrusion, Scr. Mater. 59 (2008) 1006–1009. doi:10.1016/j.scriptamat.2008.07.007.
[28] V. Segal, Materials processing by simple shear, Mater. Sci. Eng. A. 197 (1995) 157–164. http://linkinghub.elsevier.com/retrieve/pii/0921509395097058.
[29] V.M. Segal, Equal channel angular extrusion : from macromechanics to structure formation, 271 (1999) 322–333.
[30] V.M. Segal, Engineering and commercialization of equal channel angular extrusion (ECAE), Mater. Sci. Eng. A. 386 (2004) 269–276. doi:10.1016/j.msea.2004.07.023.
[31] R.Y.E. Lapovok, The role of back-pressure in equal channel, 0 (2005) 341–346.
[32] R. Lapovok, The positive role of back-pressure in equal channel angular extrusion, Mater. Sci. Forum. 503–504 (2006) 37–44. doi:10.4028/www.scientific.net/MSF.503-504.37.
[33] P.W.J. Mckenzie, R. Lapovok, Y. Estrin, The influence of back pressure on ECAP processed AA 6016: Modeling and experiment, Acta Mater. 55 (2007) 2985–2993. doi:10.1016/j.actamat.2006.12.038.
[34] R. Boulahia, J.-M. Gloaguen, F. Zaïri, M. Naït-Abdelaziz, R. Seguela, T. Boukharouba, J.-M. Lefebvre, Deformation behaviour and mechanical properties of polypropylene processed by equal channel angular extrusion: effects of back-pressure and extrusion velocity, Polymer (Guildf). 50 (2009) 5508–5517.
[35] A. Chapuis, J.H. Driver, Temperature dependency of slip and twinning in plane strain compressed magnesium single crystals, Acta Mater. 59 (2011) 1986–1994. doi:10.1016/j.actamat.2010.11.064.
[36] S. Suwas, G. Gottstein, R. Kumar, Evolution of crystallographic texture during equal channel angular extrusion (ECAE) and its effects on secondary processing of magnesium, Mater. Sci. Eng. A. 471 (2007) 1–14. doi:10.1016/j.msea.2007.05.030.
[37] G.G. Yapici, I. Karaman, Common trends in texture evolution of ultra-fine-grained hcp materials during equal channel angular extrusion, Mater. Sci. Eng. A. 503 (2009) 78–81. doi:10.1016/j.msea.2008.01.098.
[38] D.C. Foley, M. Al-Maharbi, K.T. Hartwig, I. Karaman, L.J. Kecskes, S.N. Mathaudhu, Grain refinement vs. crystallographic texture: Mechanical anisotropy in a magnesium

alloy, Scr. Mater. 64 (2011) 193–196. doi:10.1016/j.scriptamat.2010.09.042.
[39] M.A. Meyers, C. Taylor Aimone, Dynamic fracture (spalling) of metals, Prog. Mater. Sci. 28 (1983) 1–96. doi:10.1016/0079-6425(83)90003-8.
[40] N.A. Pedrazas, D.L. Worthington, D.A. Dalton, P.A. Sherek, S.P. Steuck, H.J. Quevedo, A.C. Bernstein, E.M. Taleff, T. Ditmire, Effects of microstructure and composition on spall fracture in aluminum, Mater. Sci. Eng. A. 536 (2012) 117–123. doi:10.1016/j.msea.2011.12.083.
[41] T. De Rességuier, S. Hemery, E. Lescoute, P. Villechaise, G.I. Kanel, S. V. Razorenov, Spall fracture and twinning in laser shock-loaded single-crystal magnesium, J. Appl. Phys. 121 (2017). doi:10.1063/1.4982352.
[42] E. Wielewski, G.J. Appleby-Thomas, P.J. Hazell, A. Hameed, An experimental investigation into the micro-mechanics of spall initiation and propagation in Ti-6Al-4V during shock loading, Mater. Sci. Eng. A. 578 (2013) 331–339. doi:10.1016/j.msea.2013.04.055.
[43] M. Ponga, A.A. Ramabathiran, K. Bhattacharya, M. Ortiz, Dynamic behavior of nano-voids in magnesium under hydrostatic tensile stress, Model. Simul. Mater. Sci. Eng. 24 (2016) 65003. doi:10.1088/0965-0393/24/6/065003.
[44] P.J. Hazell, G.J. Appleby-Thomas, E. Wielewski, C. Stennett, C. Siviour, The influence of microstructure on the shock and spall behaviour of the magnesium alloy, Elektron 675, Acta Mater. 60 (2012) 6042–6050. doi:10.1016/j.actamat.2012.07.041.
[45] L. Farbaniec, C.L. Williams, L. Kecskes, K.T. Ramesh, R. Becker, Microstructural effects on the spall properties of ECAE-processed AZ31B magnesium alloy, Int. J. Impact Eng. 98 (2016) 34–41. doi:10.1016/j.ijimpeng.2016.08.001.
[46] T. Sakai, A. Belyakov, R. Kaibyshev, H. Miura, J.J. Jonas, Dynamic and post-dynamic recrystallization under hot, cold and severe plastic deformation conditions, Prog. Mater. Sci. 60 (2014) 130–207. doi:10.1016/j.pmatsci.2013.09.002.
[47] R.D. Doherty, D. a. Hughes, F.J. Humphreys, J.J. Jonas, D.J. Jensen, M.E. Kassner, W.E. King, T.R. McNelley, H.J. McQueen, a. D. Rollett, Current issues in recrystallization: a review, Mater. Sci. Eng. A. 238 (1997) 219–274. doi:10.1016/S0921-5093(97)00424-3.
[48] a. G. Beer, M.R. Barnett, Microstructural Development during Hot Working of Mg-3Al-1Zn, Metall. Mater. Trans. A. 38 (2007) 1856–1867. doi:10.1007/s11661-007-9207-5.
[49] O. Sitdikov, R. Kaibyshev, Dynamic recrystallization in pure magnesium, Mater. Trans. 42 (2001) 1928–1937. doi:10.2320/matertrans.42.1928.
[50] T. Al-Samman, G. Gottstein, Dynamic recrystallization during high temperature deformation of magnesium, Mater. Sci. Eng. A. 490 (2008) 411–420. doi:10.1016/j.msea.2008.02.004.
[51] a Galiyev, R. Kaibyshev, G. Gottstein, Correlation of plastic deformation and dynamic recrystallization in magnesium alloy ZK60, Acta Mater. 49 (2001) 1199–1207. http://linkinghub.elsevier.com/retrieve/pii/S1359645401000209.
[52] G. Wang, S.D. Wu, L. Zuo, C. Esling, Z.G. Wang, G.Y. Li, Microstructure, texture, grain boundaries in recrystallization regions in pure Cu ECAE samples, Mater. Sci. Eng. A. 346 (2003) 83–90. doi:10.1016/S0921-5093(02)00521-X.
[53] W.. Cao, a Godfrey, Q. Liu, EBSP investigation of microstructure and texture evolution during equal channel angular pressing of aluminium, Mater. Sci. Eng. A. 361 (2003) 9–14. doi:10.1016/S0921-5093(03)00055-8.
[54] P. Sun, P. Kao, C. Chang, Effect of Deformation Route on Microstructural Development in Aluminum Processed by Equal Channel Angular Extrusion, 35 (2004) 1359–1368.
[55] S. Suwas, L.S. Tóth, J.-J. Fundenberger, A. Eberhardt, Texture Evolution in Commercially Pure Al during Equal Channel Angular Extrusion (ECAE) as a Function of Processing Routes, Solid State Phenom. 105 (2005) 357–362. doi:10.4028/www.scientific.net/SSP.105.357.

[56] G.G. Yapici, I. Karaman, Z.-P. Luo, Mechanical twinning and texture evolution in severely deformed Ti–6Al–4V at high temperatures, Acta Mater. 54 (2006) 3755–3771. doi:10.1016/j.actamat.2006.04.007.
[57] G. Purcek, O. Saray, O. Kul, I. Karaman, G.G. Yapici, M. Haouaoui, H.J. Maier, Mechanical and wear properties of ultrafine-grained pure Ti produced by multi-pass equal-channel angular extrusion, Mater. Sci. Eng. A. 517 (2009) 97–104. doi:10.1016/j.msea.2009.03.054.
[58] R.D. Field, K.T. Hartwig, C.T. Necker, J.F. Bingert, S.R. Agnew, Equal-Channel Angular Extrusion of Beryllium, 33 (2002) 965–972.
[59] I.J. Beyerlein, R.D. Field, K.T. Hartwig, C.T. Necker, Texture development in two-pass ECAE-processed beryllium, J. Mater. Sci. 43 (2008) 7465–7473. doi:10.1007/s10853-008-2635-9.
[60] L.R. Cornwell, K.T. Hartwig, R.E. Goforth, S.L. Semiatin, The equal channel angular extrusion process for materials processing, Mater. Charact. 37 (1996) 295–300. doi:10.1016/S1044-5803(97)80018-6.
[61] M. Furukawa, Z. Horita, M. Nemoto, T.G. Langdon, Review: Processing of metals by equal-channel angular pressing, J. Mater. Sci. 36 (2001) 2835–2843. doi:10.1023/a:1017932417043.
[62] S.R. Agnew, J. a. Horton, T.M. Lillo, D.W. Brown, Enhanced ductility in strongly textured magnesium produced by equal channel angular processing, Scr. Mater. 50 (2004) 377–381. doi:10.1016/j.scriptamat.2003.10.006.
[63] G.W. Qin, Y. Ren, W. Huang, S. Li, W. Pei, Grain refining mechanism of Al-containing Mg alloys with the addition of Mn-Al alloys, J. Alloys Compd. 507 (2010) 410–413. doi:10.1016/j.jallcom.2010.07.164.
[64] S. Biswas, S. Singh D., A. Bhowmik, S. Suwas, Study of Texture Evolution of Pure Magnesium during ECAE Using EBSD, Mater. Sci. Forum. 584–586 (2008) 343–348. doi:10.4028/www.scientific.net/MSF.584-586.343.
[65] G. Gottstein, T. Al Samman, Texture development in pure Mg and Mg alloy AZ31, in: Mater. Sci. Forum, Trans Tech Publ, 2005: pp. 623–632.
[66] B. Beausir, S. Biswas, D.I. Kim, L.S. Tóth, S. Suwas, Analysis of microstructure and texture evolution in pure magnesium during symmetric and asymmetric rolling, Acta Mater. 57 (2009) 5061–5077. doi:10.1016/j.actamat.2009.07.008.
[67] R.B. Figueiredo, T.G. Langdon, Principles of grain refinement and superplastic flow in magnesium alloys processed by ECAP, Mater. Sci. Eng. A. 501 (2009) 105–114. doi:10.1016/j.msea.2008.09.058.
[68] S. Biswas, D.S. Singh, B. Beausir, L.S. Toth, S. Suwas, Thermal Response on the Microstructure and Texture of ECAP and Cold-Rolled Pure Magnesium, Metall. Mater. Trans. A Phys. Metall. Mater. Sci. 46 (2015) 2598–2613. doi:10.1007/s11661-015-2846-z.
[69] S.R. Agnew, P. Mehrotra, T.M. Lillo, G.M. Stoica, P.K. Liaw, Crystallographic texture evolution of three wrought magnesium alloys during equal channel angular extrusion, Mater. Sci. Eng. A. 408 (2005) 72–78. doi:10.1016/j.msea.2005.07.052.
[70] A.S.M.I.H. Committee, Properties and Selection: Nonferrous Alloys and Special- Purpose Materials, ASM International, 1990. https://books.google.com/books?id=wxA7AQAAIAAJ.
[71] K.Y. Xie, Chemical Analysis of precipitates, n.d.
[72] N. Stanford, D. Atwell, The effect of Mn-rich precipitates on the strength of AZ31 extrudates, Metall. Mater. Trans. A Phys. Metall. Mater. Sci. 44 (2013) 4830–4843. doi:10.1007/s11661-013-1817-5.
[73] N. Dixit, K.Y. Xie, K.J. Hemker, K.T. Ramesh, Microstructural evolution of pure magnesium under high strain rate loading, Acta Mater. 87 (2015) 56–67. doi:10.1016/j.actamat.2014.12.030.

[74] A.S. Khan, A. Pandey, T. Gnäupel-herold, R.K. Mishra, Mechanical response and texture evolution of AZ31 alloy at large strains for different strain rates and temperatures, Int. J. Plast. 27 (2011) 688–706. doi:10.1016/j.ijplas.2010.08.009.
[75] M. Knezevic, A. Levinson, R. Harris, R.K. Mishra, R.D. Doherty, S.R. Kalidindi, Deformation twinning in AZ31 : Influence on strain hardening and texture evolution, Acta Mater. 58 (2010) 6230–6242. doi:10.1016/j.actamat.2010.07.041.
[76] A.A. Salem, S.R. Kalidindi, R.D. Doherty, S.L. Semiatin, Strain Hardening Due to Deformation Twinning in ⌴ -Titanium : Mechanisms, 37 (2006) 259–268.
[77] Z.S. Basinski, M.S. Szczerba, M. Niewczas, J.D. Embury, S.J. Basinski, The transformation of slip dislocations during twinning of copper-aluminum alloy crystals, Rev. Metall. 94 (1997) 1037–1044.
[78] M. Al-Maharbi, I. Karaman, I.J. Beyerlein, D. Foley, K.T. Hartwig, L.J. Kecskes, S.N. Mathaudhu, Microstructure, crystallographic texture, and plastic anisotropy evolution in an Mg alloy during equal channel angular extrusion processing, Mater. Sci. Eng. A. 528 (2011) 7616–7627. doi:10.1016/j.msea.2011.06.043.
[79] B. Li, S. Joshi, K. Azevedo, E. Ma, K.T. Ramesh, R.B. Figueiredo, T.G. Langdon, Dynamic testing at high strain rates of an ultrafine-grained magnesium alloy processed by ECAP, Mater. Sci. Eng. A. 517 (2009) 24–29. doi:10.1016/j.msea.2009.03.032.
[80] B. Li, S.P. Joshi, O. Almagri, Q. Ma, K.T. Ramesh, T. Mukai, Rate-dependent hardening due to twinning in an ultrafine-grained magnesium alloy, Acta Mater. 60 (2012) 1818–1826. doi:10.1016/j.actamat.2011.12.002.
[81] K. Eswar Prasad, B. Li, N. Dixit, M. Shaffer, S.N. Mathaudhu, K.T. Ramesh, The dynamic flow and failure behavior of magnesium and magnesium alloys, Jom. 66 (2014) 291–304. doi:10.1007/s11837-013-0850-6.
[82] M.T. Tucker, M.F. Horstemeyer, P.M. Gullett, H. El Kadiri, W.R. Whittington, Anisotropic effects on the strain rate dependence of a wrought magnesium alloy, Scr. Mater. 60 (2009) 58–61. doi:10.1016/j.scriptamat.2008.10.011.
[83] S.R. Kalidindi, A. Abusafieh, Accurate Characterization of Machine Compliance for Simple Compression Testing, 37 (1997).
[84] M. Jin, Study of deformation behavior of ultrafine-grained materials through in situ nanoindentation in a transmission electron microscope, (2005) 1735–1740. doi:10.1557/JMR.2005.0216.
[85] D.S. Gianola, S. Van Petegem, M. Legros, S. Brandstetter, Stress-assisted discontinuous grain growth and its effect on the deformation behavior of nanocrystalline aluminum thin films, 54 (2006) 2253–2263. doi:10.1016/j.actamat.2006.01.023.
[86] Y. Zhang, J.A. Sharon, G.L. Hu, K.T. Ramesh, K.J. Hemker, Stress-driven grain growth in ultrafine grained Mg thin film, 68 (2013) 424–427. doi:10.1016/j.scriptamat.2012.11.013.
[87] D.W. Bainbridge, H.L. Choh, E. H. Edwards, Recent observations on the motion of small angle dislocation boundaries, Acta Metall. 2 (1954) 322–333. doi:10.1016/0001-6160(54)90175-3.
[88] C.H. Li, E.H. Edwards, J. Washburn, E.R. Parker, Stress-induced movement of crystal boundaries, Acta Metall. 1 (1953) 223–229. doi:10.1016/0001-6160(53)90062-5.
[89] J.W. Cahn, J.E. Taylor, A unified approach to motion of grain boundaries , relative tangential translation along grain boundaries , and grain rotation, 52 (2004) 4887–4898. doi:10.1016/j.actamat.2004.02.048.
[90] J.W. Cahn, Y. Mishin, Coupling grain boundary motion to shear deformation, 54 (2006) 4953–4975. doi:10.1016/j.actamat.2006.08.004.
[91] T.J. Rupert, D.S. Gianola, Y. Gan, K.J. Hemker, Experimental observations of stress-driven grain boundary migration., Science. 326 (2009) 1686–1690. doi:10.1126/science.1178226.
[92] N. Stanford, M. Barnett, Effect of composition on the texture and deformation behaviour

of wrought Mg alloys, Scr. Mater. 58 (2008) 179–182. doi:10.1016/j.scriptamat.2007.09.054.
[93] C.J. Bettles, M. Barnett, Advances in wrought magnesium alloys : fundamentals of processing, properties and applications / edited by Colleen Bettles and Matthew Barnett, Elsevier, 2012. https://books.google.co.in/books?hl=en&lr=&id=LpRwAgAAQBAJ&oi=fnd&pg=PP1&dq=Luo,+A.A.%3B+Sachdev,+A.K.+12—Applications+of+magnesium+alloys+in+automotive+engineering.+In+Advances+in+Wrought+Magnesium+Alloys%3B+Bettles,+C.,+Barnett,+M.,+Eds.%3B+Woodhead+Pub.
[94] W.W. Mullins, The statistical self-similarity hypothesis in grain growth and particle coarsening, J. Appl. Phys. 59 (1986) 1341–1349. doi:10.1063/1.336528.
[95] G. Grest, M. Anderson, Abnormal grain growth in three dimensions, Scr. Metall. …. (1990) 661–665. http://scholar.google.com/scholar?hl=en&btnG=Search&q=intitle:ABNORMAL+GRAIN+GROWTH+IN+THREE+DIMENSIONS#0.
[96] C.L. Williams, K.T. Ramesh, D.P. Dandekar, Spall response of 1100-O aluminum, J. Appl. Phys. 111 (2012). doi:10.1063/1.4729305.
[97] C.L. Williams, C.Q. Chen, K.T. Ramesh, D.P. Dandekar, The effects of cold rolling on the microstructural and spall response of 1100 aluminum, J. Appl. Phys. 114 (2013). doi:10.1063/1.4817844.
[98] C.L. Williams, C.Q. Chen, K.T. Ramesh, D.P. Dandekar, On the shock stress, substructure evolution, and spall response of commercially pure 1100-O aluminum, Mater. Sci. Eng. A. 618 (2014) 596–604. doi:10.1016/j.msea.2014.09.030.
[99] T. Voisin, N.M. Krywopusk, F. Mompiou, T.P. Weihs, Precipitation strengthening in nanostructured AZ31B magnesium thin films characterized by nano-indentation, STEM/EDS, HRTEM, and in situ TEM tensile testing, Acta Mater. 138 (2017) 174–184. doi:10.1016/j.actamat.2017.07.050.
[100] S.M. Razavi, D.C. Foley, I. Karaman, K.T. Hartwig, O. Duygulu, L.J. Kecskes, S.N. Mathaudhu, V.H. Hammond, Effect of grain size on prismatic slip in Mg–3Al–1Zn alloy, Scr. Mater. 67 (2012) 439–442. doi:10.1016/j.scriptamat.2012.05.017.
[101] P.B. Berbon, M. Furukawa, Z. Horita, M. Nemoto, T.G. Langdon, Influence of pressing speed on microstructural development in equal-channel angular pressing, Metall. Mater. Trans. A. 30A (1999) 1989–1997. doi:10.1007/s11661-999-0009-9.
[102] I. Kim, J. Kim, D.H. Shin, K.-T. Park, Effects of grain size and pressing speed on the deformation mode of commercially pure Ti during equal channel angular pressing, Metall. Mater. Trans. A. 34 (2003) 1555–1558.
[103] T. Al-Samman, K.D. Molodov, D. a. Molodov, G. Gottstein, S. Suwas, Softening and dynamic recrystallization in magnesium single crystals during c-axis compression, Acta Mater. 60 (2012) 537–545. doi:10.1016/j.actamat.2011.10.013.
[104] R.Z. Valiev, T.G. Langdon, Principles of equal-channel angular pressing as a processing tool for grain refinement, Prog. Mater. Sci. 51 (2006) 881–981. doi:10.1016/j.pmatsci.2006.02.003.
[105] K.-D. Liss, T. Schmoelzer, K. Yan, M. Reid, M. Peel, R. Dippenaar, H. Clemens, In situ study of dynamic recrystallization and hot deformation behavior of a multiphase titanium aluminide alloy, J. Appl. Phys. 106 (2009) 113526.
[106] K.-D. Liss, U. Garbe, H. Li, T. Schambron, J.D. Almer, K. Yan, In situ observation of dynamic recrystallization in the bulk of zirconium alloy, Adv. Eng. Mater. 11 (2009) 637–640.
[107] W. Wu, H. Qiao, K. An, X. Guo, P. Wu, P.K. Liaw, Investigation of deformation dynamics in a wrought magnesium alloy, Int. J. Plast. 62 (2014) 105–120. doi:10.1016/j.ijplas.2014.07.005.

[108] M.R. Barnett, Z. Keshavarz, a. G. Beer, D. Atwell, Influence of grain size on the compressive deformation of wrought Mg–3Al–1Zn, Acta Mater. 52 (2004) 5093–5103. doi:10.1016/j.actamat.2004.07.015.

Curriculum Vitae

Nicholas M. Krywopusk was born in Richboro, PA in 1988. He graduated with a B.S. in Materials Science and Engineering and a minor in Entrepreneurship and Management from Johns Hopkins University in 2011. He received his M.S.E in Materials Science and Engineering from Johns Hopkins in 2012. From 2012 to 2018, Nick was a graduate research assistant in the Department of Materials Science at John Hopkins University and received his Ph.D in 2018.